High-harmonic spectroscopy of atoms and molecules

Der Fakultät für Mathematik und Physik
der Gottfried Wilhelm Leibniz Universität Hannover

zur Erlangung des Grades
Doktorin der Naturwissenschaften
Dr. rer. nat.
genehmigte Dissertation
von

M. Sci. Jing Zhao

geboren am 05. July 1985 in Hebei, China

Hannover 2013

Referent:	Prof. Dr. Manfred Lein
Korreferent:	Prof. Dr. Dieter Bauer
Tag der Promotion:	13. Juni 2013

Abstract

High-harmonic spectroscopy has become an important tool to investigate ultrafast electron dynamics in atoms and molecules. The method relies on measuring the harmonic spectrum emitted by atoms or molecules interacting with an intense laser field. In this dissertation, we investigate theoretically the electronic dynamics probed by high-harmonic spectroscopy. We simulate the dynamics by numerical solution of the time-dependent Schrödinger equation and analyze the results with the help of simplified models.

First we investigate the electron dynamics in laser-induced tunneling in atoms. The ionization time of the electron, i.e. the time when an electron exits the tunneling barrier, can be determined by two-color high-harmonic spectroscopy: we apply a weak second-harmonic field, orthogonally polarized to the fundamental laser field, to manipulate the electron trajectory in two dimensions, which leads to the generation of orthogonally polarized odd and even harmonics. The variations of harmonic intensity and amplitude ratio of neighboring even and odd harmonics as a function of the two-color delay are used to retrieve both the ionization and return time for each harmonic order. The analysis is based on two-dimensional electron trajectories evolving in complex time.

Next we study the correlated electron dynamics in field-induced one-electron ionization. As an example with two electrons, we consider an H_2 molecule with fixed-stretched internuclear distance, such that the electronic rearrangement dynamics occurs on the sub-laser-cycle time scale and influences the harmonic spectrum. We demonstrate that strong-field ionization in combination with electron correlation can localize bound electron wave packets in molecules, which results in extrema in the harmonic spectrum. Based on the shape of the remaining bound electron wave packet, we present a recollision model that can reproduce the harmonic spectrum well.

Finally, we study the autoionization dynamics of Fano resonances. We consider the photoelectron spectrum of a one-dimensional helium atom, since it is the simplest system that exhibits autoionization, due to its metastable doubly excited electronic states. A single attosecond pulse (as available from high-harmonic generation) creates an autoionizing wavepacket, and a time-delayed infrared laser pulse probes the dynamics. We find that the Fano line profile is strongly modified by the laser field. The oscillation of the quasi-bound wavepacket leaves a signature on the electron spectrum. Also, the spectrum exhibits a fringe pattern that can be explained as a consequence of the autoionizing decay being truncated by the laser field.

Keywords: high-order harmonic generation; Fano resonance; tunnel ionization

Zusammenfassung

Spektroskopie mit hohen Harmonischen hat sich zu einem bedeutsamen Mittel zur Untersuchung der ultraschnellen Elektrondynamik in Atomen und Molekülen entwickelt. Die Methode beruht auf der Messung des harmonischen Spektrums, welches von Atomen oder Molekülen emittiert wird, die mit einem starken Laserfeld wechselwirken. In dieser Dissertation untersuchen wir durch theoretische Berechnungen die Dynamik von Elektronen, welche mittels Spektroskopie der hohen Harmonischen gemessen werden. Dazu simulieren wir die Dynamik durch numerische Lösung der zeitabhängigen Schrödingergleichung und analysieren die Ergebnisse mit Hilfe von vereinfachten Modellen.

Zuerst untersuchen wir die Elektronbewegung bei laserinduziertem Tunneln in Atomen. Die Ionisationszeit des Elektrons, d.h. die Zeit, bei der das Elektron die Tunnelbarriere verlässt, kann durch eine Zwei-Farben-Spektroskopie der hohen Harmonischen bestimmt werden: Wir legen zusätzlich die zweite Harmonische als schwaches Feld an und polarisieren sie senkrecht zur Fundamentalen, um die Elektronbahn in zwei Dimensionen zu kontrollieren. Dies führt zur Erzeugung von zueinander senkrecht polarisierten geraden und ungeraden Harmonischen. Die Variationen in der Intensität sowie im Verhältnis der Amplituden von benachbarten geraden und ungeraden Harmonischen als Funktion des Delays zwischen den beiden Farben werden benutzt, um Ionisations- und Rekombinationszeit für jede Harmonische zu bestimmen. Die Analyse basiert auf zweidimensionalen Elektronenbahnen in komplexer Zeit.

Als nächstes wird die korrelierte Elektrondynamik in feldinduzierter Ein-Elektron-Ionisation behandelt. Als ein Beispiel mit zwei Elektronen betrachten wir ein H_2-Molekül mit fixiertem, vergrößertem Kernabstand. Seine elektronische Umordnungsdynamik tritt auf einer Zeitskala unterhalb eines Laserzyklus auf und beeinflusst das harmonische Spektrum. Wir zeigen, dass Starkfeldionisation in Kombination mit elektronischer Korrelation zu lokalisierten, gebundenen Elektronenwellenpaketen in Molekülen führen kann, was zu Extremwerten im harmonischen Spektrum führt. Ausgehend von der Form des verbliebenen gebundenen Elektronenwellenpakets demonstrieren wir ein Rekollisionsmodell, welches das harmonische Spektrum gut reproduziert.

Zuletzt untersuchen wir die Autoionisationsdynamiken von Fano-Resonanzen. Wir betrachten das Photoelektronenspektrum eines eindimensionalen Heliumatoms, welches mit seinen metastabilen, doppelt angeregten elektronischen Zuständen das einfachste System mit Autoionisation ist. Ein einzelner Attosekundenpuls (wie aus hohen Harmonischen generierbar) erzeugt ein autoionisierendes Wellenpaket, dessen Dynamik mit einem zeitverzögerten infraroten Laserpuls abgefragt wird. Unsere Rechnungen zeigen, dass das Fano-Linienprofil stark durch das Laserfeld modifiziert wird. Die Oszillation des quasi-gebunden Wellenpakets hinterlässt eine Signatur im Elektronspektrum. Zudem weist das Spektrum ein Interferenzmuster auf, das als eine Konsequenz aus dem Abbruch des Autoionisationszerfalls durch das Laserfeld erklärt werden kann.

Keywords: hohen Harmonischen generierbar; Fano-Resonanzen; Tunneln

Contents

Chapter 1

Introduction

In this thesis, we investigate the electronic dynamics of atoms and molecules under the influence of strong laser fields. The invention of the laser in the 1960s has opened the door to new fascinating areas of light-matter interactions. Enormous efforts in laser development have been made in the past several decades. Until the end of the 20th century, the Titanium:Sapphire laser reached sub-10 fs pulses with peak intensities on the order of 10^{13} $\sim 10^{16}\,\mathrm{W/cm^2}$ [1]. This is usually referred to as the strong-field regime. Nowadays ultrahigh laser pulses with peak intensity higher than $10^{20}\,\mathrm{W/cm^2}$ are achievable in laboratory. In this case relativistic effects need to be taken into consideration [2]. Here we will restrict our discussion to the nonrelativistic case. In the strong-field regime, the electric field strength of the laser pulse is comparable with the Coulomb forces between the nuclei and the bound electrons, leading to field ionization. Once an electron is removed from an atom or a molecule, it is pulled far away under the acceleration by the driving laser field. At this stage, the electron feels mainly the force of the laser field, and it moves approximately as a free particle in an oscillationg field [3]. It can revisit the parent ion within one or few cycles after ionization.

In the recollision process, the electron can be scattered elastically or inelastically from the parent ion, or it recombines to the initial state by single-photon emission. Elastic scattering provides electrons with large amounts of energy through further acceleration by the field after recollision. An image of the structure of the parent ion can be imprinted onto the scattered electron momentum distribution [4–8]. Inelastic scattering leads to further ionization or excitation of the parent ion, and is the essential mechanism of non-sequential double ionization of atoms and molecules [9–14]. High-energy photons emitted through recombination of the returning electrons with the parent ion form a spectrum consisting of pronounced peaks at integer multiples of the driven laser frequency. This process is known as high-order harmonic generation

(HHG) [15–17]. It involves the conversion of multiple laser photons into one high-energy photon, and has become the most convenient method to produce coherent X-rays and attosecond (1 as = 10 $^{-18}$s) pulses.

1.1 High-order harmonic generation

High-order harmonic generation was first observed experimentally in Saclay by Ferray et al [15] and Chicago by McPherson et al [16] in 1987. Surprisingly the observed harmonic spectrum exhibited a long plateau with constant harmonic intensities and a rapid decay beyond the cutoff. The existence of the plateau cannot be explained with lowest-order perturbation theory. An empirical law based on numerical simulation was proposed shortly after by Krause, Schafer and Kulander [17], according to which the position of the cutoff of the emitted spectrum is determined by the relation $\Omega = 3U_p + I_p$, where I_p is the ionization potential and the ponderomotive potential U_p is the cycle-averaged kinetic energy of an electron oscillating in the laser field without drift motion. Later, Corkum [3] explored the physical mechanism underlying the generation of high-order harmonics, named as the classical three-step model. In the classical three-step model, the HHG process is described as a sequence of three separate steps occurring within one optical period. First, an electron tunnels through the potential barrier formed by the atomic potential and the laser field with zero initial velocity. Then the electron is accelerated as a free classical particle in the oscillating field and may be driven back to the parent ion as the electric field reverses its sign. Finally, the electron recombines to the initial state with emission of a high-energy photon. In this model, the quantum processes of ionization and recombination are assumed to be instantaneous events relying on the quasistatic picture of laser-matter interactions, i.e. the driving laser pulse varies slowly compared to the motion of bound electrons. This classical picture of high-harmonic generation succeeds in explaining the cutoff energy as the maximum kinetic energy of the recolliding electron plus the binding energy.

Through the acceleration by the laser field with near-infrared (NIR) wavelength, the kinetic energy E_k of the recolliding electron may reach up to several hundreds of eV or more. The corresponding wavelengths of the electron $\lambda_e = 2\pi\hbar/\sqrt{2mE_k}$ is in the range of a few Ångströms or even sub-Ångström, which is comparable to the size of atoms or small molecules. Therefore, the harmonic spectrum carries information on the atomic structure with Ångström spatial resolution. As a result of recombination, the kinetic energy of the rec-

olliding electron and the binding energy are converted to the energy of emitted photons, resulting in the harmonic spectrum covering the spectral range from extreme ultraviolet (XUV, 10-120 eV) to soft x-ray (120-1200 eV). The three-step process occurs on a sub-optical cycle timescale: for the commonly used Ti:Sapphire laser with a wavelength of 800 nm, the optical cycle is about 2.67 fs, while the total duration of the electron excursion is about 1 fs. In the three-step model, electrons with different kinetic energies recombine at different times. This phenomenon is known as the attochirp. It indicates that the HHG process allows for sub-femtosecond temporally resolved imaging of electron dynamics in atoms and molecules. As a consequence, the HHG process serves as a new imaging technique, referred to as high-harmonic spectrosopy (Section 1.2), combining of sub-Ångström spatial and sub-femtosecond temporal resolution. High-harmonic spectrosopy has become an important tool to investigate the electronic and geometric structure of atoms or molecules [18–27] and ultrafast dynamics [28–31].

Since harmonic generation is triggered by a laser pulse, the generated field inherits coherent properties from the laser pulse. Thus, it provides an effective way for the generation of coherent XUV or soft x-ray pulses with attosecond duration, and opens up new avenues for time-domain studies of electron dynamics in atoms and molecules on the natural time scale of bound electrons (Section 1.3).

1.2 High-harmonic spectroscopy

During the 1990s, experiments on the interaction of strong laser fields with atoms were motivated by the possibility of using HHG as a source of coherent XUV radiation. It was found that the conversion efficiency from atoms is higher than that from molecules with a similar ionization potential [32, 33]. With the progress of the experimental techniques, molecular alignment became possible in free space using ultrashort laser pulses, and HHG from molecules attracted much more attention. The dependence of the HHG signal on molecular alignment with respect to the driving laser polarization was first observed in adiabatically aligned N_2 and CS_2 [34]. The generated harmonic intensity was significantly enhanced by the alignment. The idea of using HHG to investigate molecular structure was triggered by a series of theoretical simulations on alignment dependence of HHG signals from the simple two-center molecule H_2^+ [18–20, 35, 36]. These simulations suggested that interference of harmonics emitted from the two centers is imprinted on the harmonic spectra as a

function of the alignment angle between the moleuclar axis and the driving laser polarization. Destructive interference leads to structural minima in the harmonic spectra, from which one can read information about the internuclear separation.

The existence of the intensity minima in HHG spectra was observed experimentally using aligned CO_2 molecules [22, 23]. However, it was found that the minimum position depends on the laser intensity, which cannot be simply explained as the destructive quantum interference in the recombination step. Later experimental and theoretical work suggested that the involvement of lower-lying molecular orbitals, i.e. multichannel HHG [26, 30], is responsible for the intensity dependence of the minimum position. This is possible for molecules, since electronic energy levels in molecules are only a few eV apart. It is unlike atoms with tens of eV separation. Thus in molecules, ionization from several close-lying orbitals can result in competing pathways. The authors of [37, 38] claim that macroscopic propagation plays an important role in the variation of HHG minima, even when harmonics are contributed from multiple molecular orbitals. Smirnova et al [30] interpreted the intensity dependence as a consequence of multichannel interference and the hole dynamics. Tunneling from a lower-lying orbital creates the molecular ion in an excited electronic state and the coherent superposition of electronic states results in bound electron wave-packet dynamics during the second step of HHG. Similarly, with nitrogen molecules, the initial shape and location of the hole left by strong-field ionization was imaged [39]. Since HHG with multiple channels must connect the same initial to the same final state of the molecule, it records the information about multielectron dynamics and the rearrangement of electrons upon tunneling ionization. Therefore high-harmonic spectroscopy is also capable of resolving correlated electron dynamics with attosecond temporal resolution [39–44].

Another interesting application of high-harmonic spectroscopy is the possibility to spatially image the shape of the orbital from which the electron was released. For this purpose, the molecule is aligned at different angles to the direction of the recolliding electron determined by the laser polarization axis. Molecular orbitals of N_2 were reconstructed by means of a tomographic analysis of the harmonic spectral intensity measured at different molecular alignment angles [21]. In that work, both harmonic phase and polarization were assumed to be known. Tomographic imaging of molecular orbitals using HHG has met a lot of interest since its first demonstration. The harmonic phase is an important factor for recovering the molecular orbitals in the tomographic

reconstruction procedure, and can be measured using the 'reconstruction of attosecond beating by interference of two-photon transition' (RABITT) technique [24, 45]. With the help of a series of RABITT measurements of the HHG emission from aligned N_2 at different angles between the molecular axis and the laser polarization direction, it has been suggested that not only the highest occupied molecular orbital (HOMO), but also the orbital lying just below (HOMO-1) can be reconstructed [27, 46]. This tomography approach was further extended to resolve the spatial properties of wavefunctions in systems that are difficult to align. The key point is to manipulate the electron trajectory in the continnum by adding a second-harmonic field polarized orthogonally to the fundamental field. As the relative delay between the two fields varies, the electron can recollide with the parent ion from different directions. Using this method the angular-dependent information of the p state in neon atoms was obtained [47].

Recently, high-harmonic spectroscopy has been applied to reveal the exact exit times of electrons producing high-harmonic radiation [48]. Similar to previous work [47], once the electron is released from the atom, its motion in the lateral direction is perturbed by a moderate second harmonic field polarized perpendicular to the main laser field. In this experiment, the variations of harmonic intensity and recollision angle as a function of the phase difference between the two fields are observed. The observables constitute two separate sources of information, facilitating the reconstruction of both ionization and return times of the three-step process.

These examples show that high-harmonic spectroscopy has become a powerful tool to image atomic and molecular structures and ultrafast dynamics in strong field physics.

1.3 Attosecond-domain spectroscopy

In the three-step process, each recollision gives an attosecond burst of radiation, which takes place twice per optical cycle of the laser field, resulting in an attosecond pulse train (APT) [49]. For the generation of single attosecond pulses (SAP), the most straightforward approach is to shorten the duration of the driving laser pulse such that only one recollision process can take place for the high harmonics of interest. The first SAP was produced using a few-cycle laser pulse [50], characterized by a broad continnuum spectrum. For such short laser pulses, the control of the carrier-envelope phase (CEP) is very important, because the variation of the CEP could change from the generation of a SAP

to the generation of two attosecond pulses. Moreover, the method is applicable only for the generation of SAP with photon energies near the cutoff region. To avoid the difficulty of controlling the CEP stabilized few-cycle laser pulses and generate attosecond pulses with a wide energy region, the polarization gating technique was proposed [51, 52], which relies on the fact that the recollision process can only occur for linear or nearly linear laser polarization. The combination of a left-circularly polarized pulse and a delayed right-circularly polarized pulse leads to a pulse with linear or nearly linear polarization for a short time, which can be used to for the generation of SAP in both the plateau and cut-off region of the harmonic spectrum [53, 54]. It has also been suggested that adding an orthogonally polarized second-harmonic field to the polarization gating field can suppress the depletion outside of the polarization gate so that the SAP can be generated with laser pulses as long as 28 fs [55, 56]. The polarization gating technique puts less requirements on the driving laser pulse. Up to now, the shortest attosecond pulse of 67 as, covering the energy range of 55 - 130 eV, has been generated with this method [57].

With the advent of attosecond XUV pulses, it has become possible to carry out time-resolved measurements of electronic dynamics in atoms and molecules on the natural time scale of bound electrons. Many current experiments with attosecond pulses are based on the XUV-pump-NIR-probe technique, where the XUV-pump pulse is applied to excite or ionize the atoms or molecules, and the NIR-probe pulse measures the induced variations after a certain delay with respect to the pump pulse. An important example is the attosecond streaking method [50, 58, 59], which can be used to characterize attosecond pulses. XUV-pump-XUV-probe experiments have also been reported [60, 61], but they are still highly challenging because of the low intensities of the available XUV pulses. The first reported XUV-pump-NIR-probe experiment measured the duration of an Auger decay in Kr atoms directly in the time domain using isolated attosecond pulses [62]. By analysing the photoelectron spectrum as a function of the time delay between the XUV pulse and the NIR pulse, a lifetime of about 8 fs was observed, in agreement with energy-domain spectra. The attosecond streaking method can also be used to answear the question of the precise time of electron release from an atom [63]. In the experiment, a SAP with central energy at 106 eV was applied to set electron free from the 2s and 2p orbitals of neon. Streaking by a weak NIR field produced two different streaking traces in the photoelectron spectra. Their relative phase lag indicated an emission time difference of about 20 as. Similarly, using attosecond pulse trains, it was found that the $3p$ photoelectrons from argon are emitted

about 20 as after the $3s$ photoelectrons [64].

Over the last few years, the dynamical properties of Fano resonances caused by autoionization of metastable states have been investigated via the XUV-pump-NIR-probe method [65–70]. The autoionization process governed by the electron-electron interaction is characterized by an asymmetric line shape, which is known as the Fano profile [71]. The time-resolved autoionization dynamics has been investigated by analysing the laser-modified Fano resonance profile. At the same time, the transient absorption technique was also extended to the attosecond domain for the exploration of electronic motion [67, 72–74]. In the experiment, the spectrum of the attosecond pulses transmitted through the sample was measured instead of the kinetic energy of the free electron. With the available experiment techniques, the transient absorption spectroscopy gives higher spectral resolution compared with the photoelectron spectrum. The first attosecond transient absorption experiment demonstrated the real-time observation of wave packet motion in the valence shells of krypton ions [72]. Time-resolved autoionization dynamics has also been investigated by analysing the laser-modified photoabsorption [67, 69, 74].

A completely different approach yielding access to the attosecond domain is the attosecond angular streaking [75]. This technique provides attosecond temporal resolution without attosecond pulses. In particular, it gave experimental insight into the tunnel ionization process. Angular streaking uses elliptically polarized laser pulses both to ionize the atom and to rotate the emission direction of electron and ion. Therefore the technique is suitable for the investigation of laser-induced tunneling, an entirely different ionization mechanism compared to the one-photon photoionization mentioned above. It was demonstrated that the instant of ionization is thus mapped to the peak of the final ion angular distribution. A small upper limit of 12 as between the maximum of the electric field and the maximum of electron emission was found, thus supporting the concept of instantaneous tunneling [76].

1.4 Outline of this thesis

In the next chapter, we give a review of the fundamental theory of strong-field physics. The main theoretical methods used in the modeling of high-order harmonic generation are the time-dependent Schrödinger equation and the strong-field approximation. In addition, we introduce the numerical methods used in this thesis.

In Chapter 3, inspired by the measurement of the exact exit times of elec-

trons producing high-harmonic radiation [48], we address this problem using the numerical solution of the time-dependent Schrödinger equation (TDSE). We obtain the times of ionization and return of the laser-driven electron in high-order harmonic generation and investigate the effect of tunneling on the lateral dynamics of the electron in the two-color field. Furthermore, we retrieve the tunneling time characterizing the under-barrier electron motion. Part of the work in Chapter 3 has been discussed in [77]

In Chapter 4, we study the two-channel HHG from H_2 molecules at stretched internuclear distance. We show the possibility to manipulate the location of the bound electron wave packets created by strong-field ionization. We develop a recollision model to extract the initial shape of the remaining bound electron wave packet from high-harmonic spectrum. Part of the work in Chapter 4 has been published in [44]

Chapter 5 presents our work on probing Fano resonances with the XUV-pump-NIR-probe technique. Autoionizing states in the one-dimensional helium atom are investigated by numerical solution of the TDSE. We show that the Fano line profile is strongly modified by the presence of the laser field. We observe a clear fringe pattern in the photoelectron spectrum and explain it as the truncation of the autoionizing decay by the laser field. Part of the work in Chapter 5 has been published in [70].

Chapter 2

Strong Field Physics

Tremendous progress in pulsed laser source technology has taken place since the first demonstration of laser radiation [78–80]. Pulses with a duration of only a few femtoseconds and intensities comparable to the atomic potential are now available for a broad range of wavelengths (800 nm to 2000 nm). Strong field effects, e.g. tunnel ionization, high-order harmonic generation, and non-sequential double ionization, become observable [1]. This developments pose new challenges not only in theoretical understanding but also in numerical methods for treating atomic processes in ultra-short, intense laser field.

In this chapter, we describe in detail the widely used semi-classical theory in strong field physics, where the atomic or molecular system is treated quantum mechanically while the laser field is treated classically [81]. This is a good approximation in the strong-field regime, since the laser intensity is high enough that the average photon number is very large and the electromagenetic field can be described classically. Moderately strong fields ($I \lesssim 10^{17}\,\mathrm{W/cm^2}$) do not reach the relativistic regime so that the Schödinger equation is applicable. We start by reviewing basic classical electrodynamics which eventually explains the interaction of the electric field of the laser pulse with the atoms within the electric dipole approximation by neglecting the magnetic field and the spatial dependence of the laser electric field. Next we present the time-dependent Schödinger equation describing an atom or a molecule in an electromagnetic field in the forms of the velocity gauge and length gauge. Then we discuss the mechanism of high-harmonic generation. The process will be treated using both the classical three-step model [3] and the quantum-orbit model [82]. Finally, we discuss the numerical methods applied in this thesis.

2.1 Description of the electromagnetic field

The classical description of the field is based on Maxwell's equations. These equations relate the electric and magnetic field vectors $\mathbf{E}$ and $\mathbf{B}$, together with

the electric displacement $\mathbf{D}$ and magnetic field strength $\mathbf{H}$. If there are no free charges and no free currents, the equations have the form [83]

$$\nabla \times \mathbf{H} = \frac{\partial \mathbf{D}}{\partial t}, \tag{2.1}$$

$$\nabla \times \mathbf{E} = -\frac{\partial \mathbf{B}}{\partial t}, \tag{2.2}$$

$$\nabla \cdot \mathbf{B} = 0, \tag{2.3}$$

$$\nabla \cdot \mathbf{D} = 0, \tag{2.4}$$

with the constitutive relations $\mathbf{B} = \mu_0(\mathbf{H} + \mathbf{M})$ and $\mathbf{D} = \varepsilon_0\mathbf{E} + \mathbb{P}$. Here ε_0 and μ_0 are the free space permittivity and permeability, respectively, and $\mu_0\varepsilon_0 = c^{-2}$ where c is the speed of light in vacuum. $\mathbb{P}$ is the polarization field and $\mathbf{M}$ is the magnetization field which are defined in terms of microscopic bound charges and bound current respectively.

The electric field $\mathbf{E}(\mathbf{r}, t)$ and magnetic field $\mathbf{B}(\mathbf{r}, t)$ can be generated from the scalar potential ϕ and the vector potential $\mathbf{A}$ as

$$\mathbf{E}(\mathbf{r}, t) = -\frac{\partial \mathbf{A}(\mathbf{r}, t)}{\partial t} - \nabla\phi(\mathbf{r}, t), \tag{2.5}$$

$$\mathbf{B}(\mathbf{r}, t) = \nabla \times \mathbf{A}(\mathbf{r}, t). \tag{2.6}$$

With the substitutions $\mathbf{A} \to \mathbf{A} + \nabla\chi$, $\phi \to \phi - \partial\chi/\partial t$, where χ is any scalar field, the electric field $\mathbf{E}(\mathbf{r}, t)$ and magnetic field $\mathbf{B}(\mathbf{r}, t)$ are unchanged. Therefore a further condition on the vector potential $\mathbf{A}(\mathbf{r}, t)$ is required to restrict the form of the potentials. The frequently used condition in non-relativistic physics is

$$\nabla \cdot \mathbf{A}(\mathbf{r}, t) = 0, \tag{2.7}$$

known as the Coulomb gauge, which implies, in quantum mechanics, that the momentum operator and the vector potential commute, $[\mathbf{p}, \mathbf{A}(\mathbf{r}, t)] = 0$, although $\mathbf{r}$ is taken to be position operator. In empty space, the solution of Maxwell's equations for a radiation field can always be expressed in terms of potentials such that $\nabla \cdot \mathbf{A}(\mathbf{r}, t) = 0$ and $\phi = 0$. The vector potential satisfies the wave equation

$$\nabla^2\mathbf{A}(\mathbf{r}, t) = \frac{1}{c^2}\frac{\partial^2 \mathbf{A}(\mathbf{r}, t)}{\partial t^2}. \tag{2.8}$$

A monochromatic plane wave solution of Eq. (2.8) with linear polarization reads

$$\mathbf{A}(\mathbf{r}, t) = \mathbf{A}_0 \cos(\mathbf{k} \cdot \mathbf{r} - \omega t + \delta_\omega), \tag{2.9}$$

where $\mathbf{A}_0$ describes both the amplitude and the polarization of the laser field, $\mathbf{k}$ is the propagation vector and δ_ω is a real phase. The angular frequency is $\omega = c|\mathbf{k}|$. The amplitude A_0 is related to the electric field amplitude by $E_0 = \omega A_0$ and the relation to the intensity is $I = \frac{1}{2}\varepsilon_0 c\omega^2 A_0^2$. The solution satisfies Eq. (2.7) if $\mathbf{k} \cdot \mathbf{A}_0 = 0$, i.e. the direction of the vector potential $\mathbf{A}$ is perpendicular to the propagation direction, i.e. $\mathbf{A}$ is a transverse field. The transverse electromagnetic field has an electric field, a magnetic field perpendicular to it, and a propagation direction perpendicular to both of these fields. The electric and magnetic fields associated with the vector potential $\mathbf{A}(\mathbf{r}, t)$ are

$$\mathbf{E}(\mathbf{r}, t) = -\omega \mathbf{A}_0 \sin(\mathbf{k} \cdot \mathbf{r} - \omega t + \delta_\omega), \tag{2.10}$$

$$\mathbf{B}(\mathbf{r}, t) = -\mathbf{k} \times \mathbf{A}_0 \sin(\mathbf{k} \cdot \mathbf{r} - \omega t + \delta_\omega). \tag{2.11}$$

From the above formula one finds that $|\mathbf{E}|/|\mathbf{B}| = \omega/k = c$. For the laser intensities used in this work (smaller than $10^{17}\,\mathrm{W/cm^2}$), the electron drift due to the magnetic field in the laser propagation direction is very small and can be neglected. The wavelength for femtosecond laser pulses available in laboratories today is in the visible or infrared regime, which is much larger than the typical size of atoms or small molecules, i.e. the field does not change over the spatial extent of the atoms or molecules. For instance, the laser wavelength of 800 nm is a thousand times larger than the typical atomic scale. As a consequence, one can neglect the spatial dependence of the vector potential, $\mathbf{A}(\mathbf{r}, t) \approx \mathbf{A}(t)$. This is the electric dipole approximation, which holds as long as $\mathbf{k} \cdot \mathbf{r} \ll 1$ (with the atom/molecule placed at the origin of the coordinate system). This condition holds even for the case of the extreme ultraviolet range ($\lambda \approx 100$ - 10 nm). The electric dipole approximation is used throughout the thesis.

A short laser pulse with a finite duration can be expressed as the superposition of plane waves with different frequencies. The electric field of a linearly polarized laser pulse is normally written as

$$E(t) = E_0 f(t) \cos(\omega t + \varphi), \tag{2.12}$$

where $f(t)$ is the envelope and φ is the carrier-envelope phase, i.e. the phase difference between the carrier wave and the envelope function. There are several widely used envelope forms, e.g. $\sin^2$, trapezoidal and Gaussian envelopes. In experiment, temporal profiles are often assumed to be Gaussian, while $\sin^2$ and trapezoidal profiles are more convenient in numerical simulations. It is

important to assure that the electric field of Eq. (2.12) satisfies the relation

$$\int_{-\infty}^{\infty} E(t)dt = 0. \tag{2.13}$$

A physical pulse has to obey this relation; otherwise it would contain a zero-frequency component, which is not possible for a propagating pulse.

2.2 Time-dependent Schrödinger equation

We restrict our discussion to the nonrelativistic regime, such that the time-dependent Schrödinger equation is applicable to describe the interaction between atoms or molecules and the strong laser field. Relativistic effects have to be taken into account for laser intensities higher than $10^{17}\,\mathrm{W/cm^2}$ (at 800 nm wavelength), while the laser intensities used in the thesis are lower than that.

We begin the discussion of the theory with the single-active-electron approximation (SAE), in which only one of the electrons in the highest occupied orbital that ionizes is considered to be 'active', while the remaining electrons are frozen in the initial configuration. The SAE approximation has been successfully employed for many aspects of strong laser-matter interaction. However, recent experiments show clear evidence of multi-electron effects both in harmonic generation [84–86] and nonsequential double ionization [87–89].

The SAE Hamiltonian describing an atomic or a molecular electron exposed to a laser beam reads [90] (atomic units [1] are used unless stated otherwise)

$$H(t) = \frac{(\mathbf{p} + \mathbf{A}(\mathbf{r},t))^2}{2} + V(\mathbf{r}) \tag{2.14}$$

where $\mathbf{p} = -i\nabla$ is the momentum operator, $\mathbf{r}$ is the position of the electron and $V(\mathbf{r})$ is the binding potential between the electron and the remaining particles of the atom or molecule. The corresponding TDSE is given by

$$i\frac{\partial}{\partial t}\Psi(\mathbf{r},t) = \left[\frac{\mathbf{p}^2}{2} + \mathbf{p}\cdot\mathbf{A}(\mathbf{r},t) + \frac{\mathbf{A}^2(\mathbf{r},t)}{2} + V(\mathbf{r})\right]\Psi(\mathbf{r},t). \tag{2.15}$$

The term $\mathbf{p}\cdot\mathbf{A}(\mathbf{r},t)$ describes the interaction between the active electron and the laser field. This form is called velocity gauge since the laser-matter in-

[1] Atomic units are widely used in atomic physics, in which the fundamental physical constants are set to unity as $\hbar = m_e = e = 4\pi\varepsilon_0 = 1$. It results in the fine-structure constant $\alpha = \frac{e^2}{4\pi\varepsilon_0\hbar c} \approx \frac{1}{137}$, and the corresponding unit of length: $a_0 = \frac{4\pi\varepsilon_0\hbar^2}{m_e e} = 5.29\times10^{-11}\,m = 0.53\,\text{Å}$, time: $\tau_0 = \frac{(4\pi\varepsilon_0)^2\hbar^3}{m_e e^4} = 24.2\,\text{as}$, energy: $E = \frac{m_e e^4}{(4\pi\varepsilon_0)^2\hbar^2} = 27.21\,\text{eV}$, electric field: $E_0 = \frac{e}{4\pi\epsilon_0 a_0^2} = 5.14\times10^{11}\,\text{V/m}$ and laser intensity: $I = \frac{1}{2}\epsilon_0 c E_0^2 = 3.51\times10^{16}\,\text{W/cm}^2$.

teraction arises from the momentum. In the spirit of the electric dipole approximation, the spatial dependence of the vector potential is neglected, and the term $\mathbf{p} \cdot \mathbf{A}(t)$ is a function of time. The term $\frac{1}{2}\mathbf{A}^2(t)$ can be removed by introducing a phase factor

$$\Psi(\mathbf{r}, t) = \exp\left[-i \int^t \frac{\mathbf{A}^2(t')}{2} dt'\right] \Psi_V(\mathbf{r}, t), \tag{2.16}$$

which yields the velocity-gauge TDSE in the form

$$i\frac{\partial}{\partial t}\Psi_V(\mathbf{r}, t) = \left[\frac{\mathbf{p}^2}{2} + \mathbf{p} \cdot \mathbf{A}(t) + V(\mathbf{r})\right] \Psi_V(\mathbf{r}, t). \tag{2.17}$$

It is well known that quantum mechanics is invariant with respect to unitary transformations. Through a unitary transformation related to a gauge transformation of $\mathbf{A}(t)$,

$$\Psi_L(\mathbf{r}, t) = \exp\left(i\mathbf{A}(t) \cdot \mathbf{r}\right) \Psi(\mathbf{r}, t), \tag{2.18}$$

one obtains the TDSE in the length gauge,

$$i\frac{\partial}{\partial t}\Psi_{\mathrm{L}}(\mathbf{r}, t) = \left[\frac{\mathbf{p}^2}{2} + \mathbf{r} \cdot \mathbf{E}(t) + V(\mathbf{r})\right] \Psi_{\mathrm{L}}(\mathbf{r}, t). \tag{2.19}$$

Eq. (2.17) and (2.19) are the commonly used equations for the numerical treatment of laser-matter interactions. In the velocity gauge, the light-matter interaction operator is $\mathbf{p} \cdot \mathbf{A}(t)$; in the length gauge, it is the operator $\mathbf{r} \cdot \mathbf{E}(t)$. The two gauges are completely equivalent (as long as the TDSE is solved exactly) and the use of a specific gauge is merely a matter of convenience. The TDSE in the length gauge is conceptually simpler to understand, since it provides a physical interpretation of laser-induced ionization in terms of tunneling, which is specific to the length gauge. The oscillating field creates a barrier in the total potential $\mathbf{r} \cdot \mathbf{E}(t) + V(\mathbf{r})$, such that the electron gets the opportunity to tunnel. In fact, physics should not depend on what gauge is used, and all the observables must be the same in both gauges if the solutions of the TDSE are obtained exactly. Here it is important to note that although the momentum operator in both equations is the same, namely $\mathbf{p} = -i\nabla$, it has different physical meanings. In the velocity gauge, it is the canonical momentum of the electron, whereas it is the kinetic momentum of the electron (i.e. proportional to the physical velocity) in the length gauge.

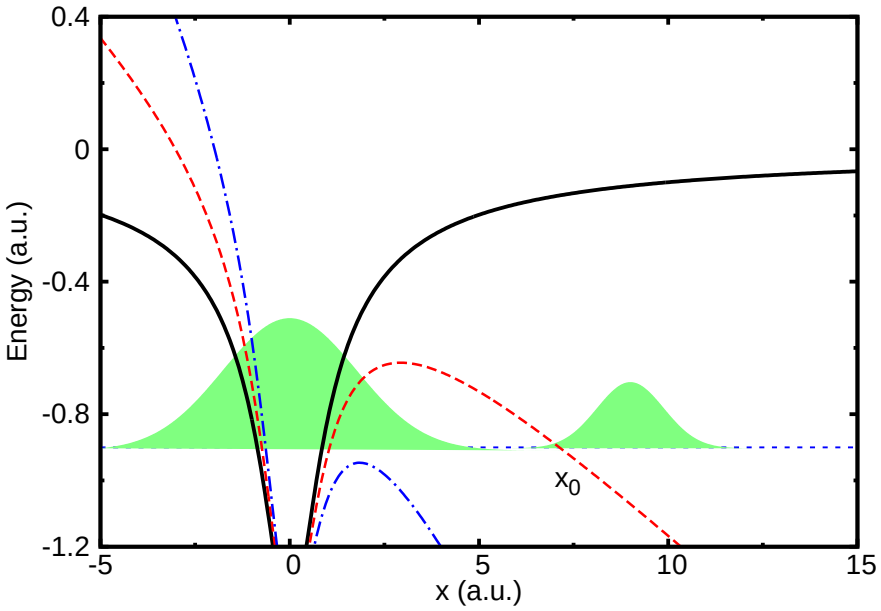

Figure 2.1: Potential for a helium atom in the length gauge with static electric field E_0=0 (solid line), E_0=0.107 a.u. (dashed line) and E_0=0.239 a.u. (dash-dotted line). The horizontal dotted line marks the ground-state electron energy of -0.903 a.u. The green shaded distribution schematically depicts the electron distribution after tunneling.

2.3 High-order harmonic generation

2.3.1 Tunnel ionization

When an atom or a molecule is subjected to a strong static electric field, the binding potential is distorted so much that a barrier is formed as depicted in Fig. 2.1 for different strengths E = -E_0 of the field. (The sign of the field is chosen such that the force on the electron points to the right.) Without the electric field, the electron is localized between the potential walls. As the strength of the field increases, the electron may tunnel through the potential barrier formed by the superposition of the external electric field and the atomic binding potential. When the electric field is further increased, the top of the potential barrier falls below the binding energy, and the electron can escape by classical motion over the barrier. This is known as over-the-barrier ionization (OTBI).

Tunnel ionization depends exponentially on the electric field strength. From

analytical modeling, the tunnel ionization rate Γ is [91]

$$\Gamma = \Gamma_0 \exp\left[-\frac{2(2I_p)^{3/2}}{3E_0}\right], \tag{2.20}$$

where Γ_0 depends on the spatial structure of the bound state. The electron is supposed to be released at the exit x_0. The width of the potential barrier is given by $x_0 = I_p/E_0$ if a triangular barrier is assumed. When the electron moves under the barrier, one gets an imaginary velocity $\kappa(x) = i\sqrt{2[V(x) - xE_0 + I_p]}$. It implies that tunneling occurs in imaginary time, that is, the time that the electron spends to pass through the barrier is purely imaginary. The Keldysh *tunneling time* is defined as the absolute value of this time [92, 93]

$$\begin{aligned} \tau_{\mathrm{T}} &= \left| \int_0^{x_0} \frac{1}{\kappa(x)} dx \right| \\ &= \int_0^{x_0} \frac{1}{\sqrt{2[V(x) - xE_0 + I_p]}} dx \\ &= \frac{\sqrt{2I_p}}{E_0}. \end{aligned} \tag{2.21}$$

In the last step, a triangular barrier has been assumed, i.e. $V(x) = 0$. The Keldysh tunneling time is typically a few hundred attoseconds and is almost equal to the imaginary part of the complex ionization time obtained in the quantum-orbit model [94].

Although the tunnel ionization rate is derived under the assumption of a static field, it is also valid for slowly oscillating electric fields, in which an electron has enough time to pass through the potential barrier while the electric field does not change too much. To be quantitative we can use the Keldysh parameter [92], defined as the product of the laser frequency ω and the tunneling time τ_{T},

$$\gamma = \omega\tau_{\mathrm{T}} = \omega\frac{\sqrt{2I_p}}{E_0} = \sqrt{\frac{I_p}{2U_p}}, \tag{2.22}$$

with the pondermotive energy $U_p = E_0^2/4\omega^2$.

If $\gamma \ll 1$, the tunneling time is small compared with the period of the oscillating electric field. Thus the field can be considered as almost static during tunneling. Replacing the modulus of the static electric field E_0 by modulus of the instantaneous electric field $|E(t)|$ leads to the instantenous

ionization rates $\Gamma(t)$ for the slowly oscillating field. This means that tunneling is the dominant ionization mechanism when lasers with high intensities and long wavelengths are applied. For an infrared laser pulse with a wavelength of 800 nm and intensity of $4\times10^{14}\,\mathrm{W/cm^2}$, the Keldysh parameter is $\gamma = 0.53$ for the helium atom. Because of the exponential law Eq. (2.20), the tunnel ionization rate shows a strong maximum at times when the electric field reaches its maximum. $\gamma \gg 1$ corresponds to pulses with weak intensities or high frequencies. In this case, the quasi-static approximation breaks down and the electrons do not have enough time to follow the fast changes in the potential. They feel a time-averaged effect of the laser field rather than a quasi-static barrier. This ionization mechanism is termed multiphoton ionization.

2.3.2 Three-step model

High-order harmonic generation is a nonlinear process, in which a large number of laser photons are converted into a single photon of high energy. The mechanisum for high-order harmonic generation is successfully explained by the classical three-step model proposed by Corkum [3], as depicted in Fig. 2.2. First, an electron from an atom or a molecule, exposed to a strong laser field, tunnels into the continuum through the potential barrier. Then the electron is accelerated as a free particle in the oscillating field and may be driven back to the parent ion as the electric field changes directions. Finally, the electron can recombine to the initial state by emitting an XUV photon. The photon energy equals the kinetic energy of the returning electron acquired in the continuum plus the binding energy of the electron in the ground state. According to Eq. (2.20), the tunnel ionization rate depends exponentially on the strength of the electric field, indicating that tunneling mainly occurs around the maxima of the oscillating electric field, i.e. tunneling is confined to a short time interval around the field peaks. Once the electron is released, its motion is dominated by the oscillating laser field. Due to the large classical action of the electron in the continuum, the electron motion is described classically in the three-step model. Even without the quantum-mechanical processes of tunnel ionization and recombination modelling, the classical dynamics explains the observed cutoff in the harmonic spectrum.

In the following, the classical motion of the free electron is described in detail. We assume that a monochromatic field linearly polarized along the x-axis with electric field $E(t) = E_0\cos(\omega t)$ is used, so that the electron is accelerated along a straight line. Suppose an electron is born at time t_i with a initial velocity of zero at $x = 0$. Its subsequent motion is determined by

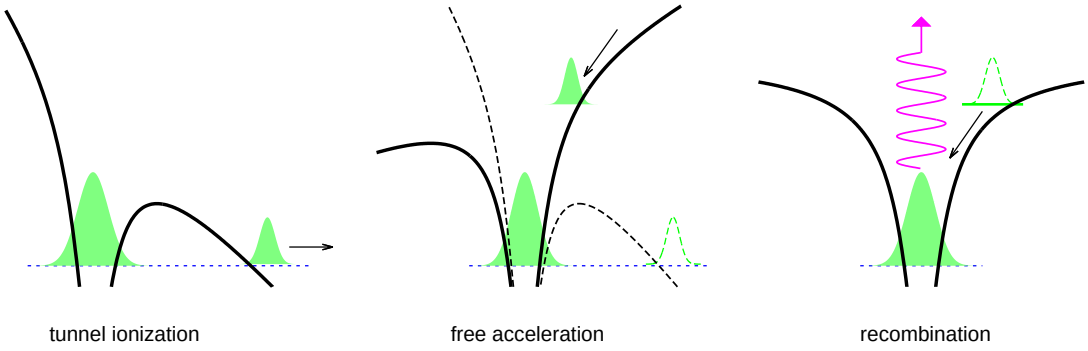

Figure 2.2: Illustration of the three-step model for high harmonic generation. First the laser electric field releases the electron from the atomic attractive potential via tunnel ionization. Then the electric field drives the electron back to the ion. Finally, the electron recombines with the ion by emission of a high-energy photon.

Newton's equation

$$\ddot{x}(t) = -E(t). \tag{2.23}$$

The solution to Eq. (2.23) with the initial condition stated above yields the instantaneous electron displacement

$$x(t) = \alpha \left[\omega(t - t_i)\sin(\omega t_i) + \cos(\omega t) - \cos(\omega t_i)\right], \tag{2.24}$$

where $\alpha = E_0/\omega^2$ is the classical oscillation amplitude. The value of α is on the order of nanometres ($\approx$ 33 a.u. at laser intensity $4\times10^{14}\,\mathrm{W/cm^2}$ of 800 nm), much larger than the atomic radius. It demonstrates the validity of treating the electron as a freely moving particle in the laser field. The instantaneous electron velocity is

$$v(t) = -\int_{t_i}^{t} E(t'')dt'' = \frac{E_0}{\omega}\left[\sin(\omega t_i) - \sin(\omega t)\right]. \tag{2.25}$$

It consists of a drift velocity $v_D = \frac{E_0}{\omega}\sin(\omega t_i)$ determined by the phase ωt_i of the oscillating field at which the electron is released, and an oscillating term with amplitude E_0/ω. For sufficiently long laser pulses, the velocity of the detected photoelectron equals the drift velocity if there is no additional interaction with the parent ion. From this, one obtains the maximum velocity $v_{max} = E_0/\omega$, and the corresponding maximum kinetic energy $v_{max}^2/2 = E_0^2/(2\omega^2)$. From Eq. (2.25), the instantaneous kinetic energy of the

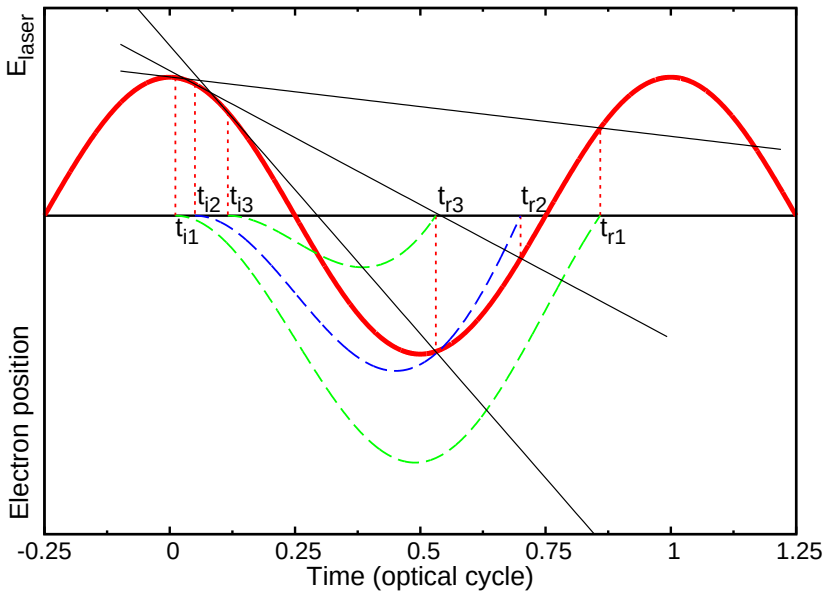

Figure 2.3: Graphical solution of the return time t_r for given start time t_i with the electric field $E(t) = E_0 \cos(\omega t)$. The solid thick curves represents the electric field. Dashed curves represent the classical electron trajectories corresponding to different release times. Solid thin curves are the tangent lines of the function $E(t)$ at different birth times t_i. The intersection points are the corresponding return times t_r.

electron is

$$E_k(t) = 2U_p \left[\sin^2(\omega t) - 2\sin(\omega t)\sin(\omega t_i) + \sin^2(\omega t_i)\right]. \tag{2.26}$$

The electron returns to the parent ion at time t_r when $x(t_r) = 0$, i.e.

$$\omega(t_r - t_i)\sin(\omega t_i) = \cos(\omega t_i) - \cos(\omega t_r). \tag{2.27}$$

Solutions of Eq. (2.27) will give all the electron trajectories characterized by pairs (t_i, t_r) of birth times t_i and recollision times t_r. Eq. (2.27) can be solved graphically as illustrated in Fig. 2.3, where the return time t_r is determined as the intersection point between the function of the electric field $E(t)$ and its tangent line at the ionization time t_i.

When analyzing the classical trajectories of the electrons in the external electric field in Fig. 2.3, one finds that Eq. (2.27) cannot be fulfilled for every electron birth time t_i. Electrons born between the zero-crossing and the maximum of the field never return to the parent ion. Those electrons do not

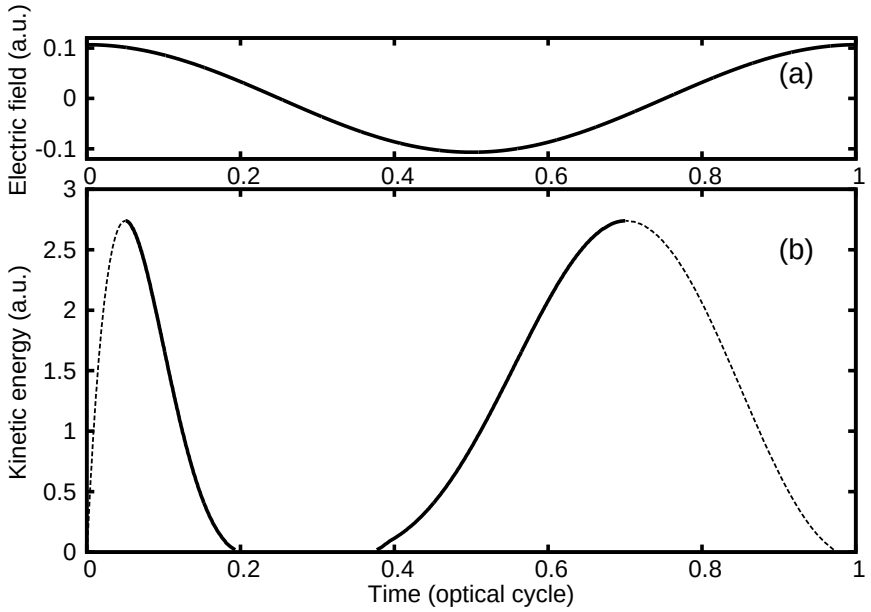

Figure 2.4: (a) Electric field of a laser pulse with 800 nm wavelength and intensity $4\times10^{14}\,\mathrm{W/cm^2}$. (b) Electron kinetic energy at the instant of recollision as a function of ionization time and return time. Dashed lines represent results for the long trajectory. Solid lines represent the short trajectory.

contribute to HHG. Electrons released between the field maximum and the zero-crossing return to the parent ion and may recombine. The classical trajectory depends on the release time. The kinetic energy of the electron at the time of its return is

$$E_k = 8U_p \left[\cos\frac{\omega}{2}(t_r + t_i)\sin\frac{\omega}{2}(t_r - t_i)\right]^2. \tag{2.28}$$

Fig. 2.4 shows the kinetic energy of the electron at the instant of recollision as a function of the ionization time t_i or alternatively the return time t_r. There exists a cutoff, i.e. a maximum kinetic energy that the electron can possess when it re-encounters its parent ion. From numerical evaluation of Eq. (2.28), the maximum kinetic energy is $E_{k,\mathrm{max}}$=3.17U_p [3] at an ionization phase close to ωt_i=17°. If we consider electron trajectories returning within one optical cycle, as shown in Fig. 2.4, for given electron kinetic energy there are two possible trajectories, and they merge at the cutoff.

As shown in Fig. 2.4(b), the short trajectories have a return energy monotonically increasing with the return time. "Short" refers to the excursion time, i.e. the time between ionization and recollision. On the other hand, trajectories corresponding to electrons that are born just after the peak of the laser

field with recollision after more than 0.65 optical cycles are called the long trajectories. In this case, the return energy monotonically decreases with the excursion time.

The photon energy emitted in the third step of the three-step model is $\Omega = E_k + I_p$. The classical maximum value of the return energy leads to the maximum photon energy of $\Omega_{\text{cutoff}} = I_p + 3.17U_p$. This is the commonly known cut-off law for high-harmonic generation. For multi-cycle laser pulses, the lower harmonics have several recollisions with the same photon energy. Due to the quantum-mechanical nature of the electron, the spreading of the electron wave packet during propagation reduces the overlap with the ground state of the system. Therefore only the first two encounters of the electron with the parent ion lead to significant photon emission.

From Fig. 2.4, it is clear that the recollision process is confined to a fraction of the laser period. This temporal confinement results in an attosecond temporal structure of the emitted pulses. Furthermore, different harmonic frequencies are emitted at different instants, i.e. the harmonic emission is chirped. The chirps for the short and long trajectories are of different sign. It is positive for the short trajectory and negative for the other. In experiments, the predominance of harmonic emission from either the short or long trajectories depends on phase matching conditions. Under the commonly used experimental conditions, where the gas jet is placed after the laser focus, the short trajectory is favored.

For linearly polarized long pulses and atoms or molecules with inversion symmetry, the three-step process repeats every half-cycle of the driving laser field with the same intensities but with phase differences of π relative to each other. The electric field of the harmonic radiation in the time domain reads

$$E_H(t) = -E_H(t + \frac{T}{2}), \tag{2.29}$$

with T being the period of the laser field. The emitted spectrum in the frequency domain is given by

$$E_H(\Omega) = \int E_H(t)e^{i\Omega t}dt = \sum_n e^{in\Omega T}(1 - e^{i\Omega\frac{T}{2}}) \int_0^{\frac{T}{2}} E_H(t)e^{i\Omega t}dt. \tag{2.30}$$

Constructive interference occurs when

$$\frac{T}{2}\Omega = (2m + 1)\pi, \qquad m = 0, 1, \ldots, \tag{2.31}$$

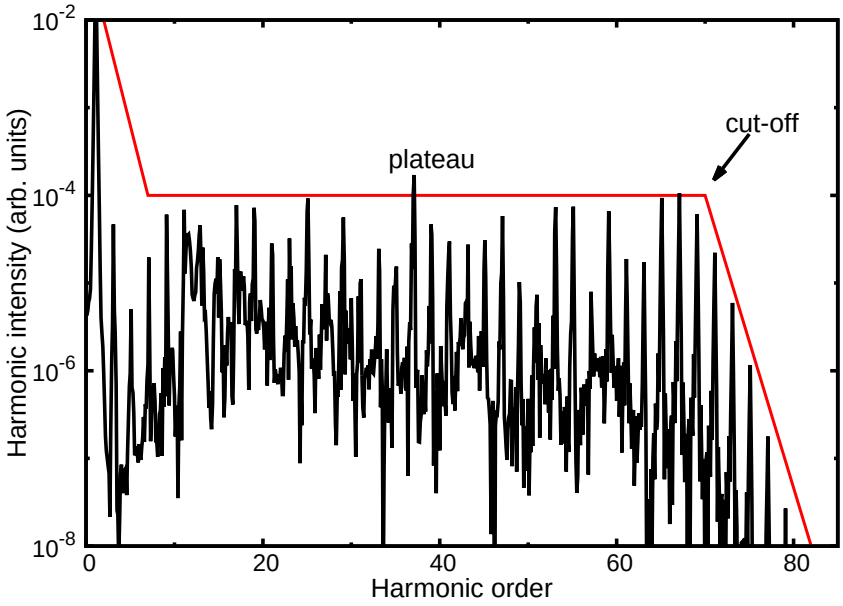

Figure 2.5: High-harmonic spectrum generated from a 2D model helium atom using a laser pulse of 800 nm with intensity $4\times10^{14}\,\mathrm{W/cm^2}$.

i.e. when Ω is an odd multiple of the fundamental laser frequency. Fig. 2.5 shows the harmonic spectrum from a 2D model helium atom with a multicycle laser pulse. Indeed, only odd harmonics are present in the spectrum. Also it exhibits the characteristic plateau and cutoff. For atoms or molecules that do not possess inversion symmetry or if the external field breaks the inversion symmetry, harmonic emission will be periodic not with a period of a half cycle but a full cycle of the laser field, leading to harmonic peaks separated by the laser frequency $2\pi/T$. Thus both even and odd harmonics can be generated.

2.3.3 Quantum-orbit model

The classical three-step model is able to explain the cutoff in the harmonic spectrum, but the initial tunnel ionization and the recombination are quantum-mechanical processes that require separate treatment. In this section, we introduce the quantum-mechanical description of the three-step process [95], based on the strong-field approximation (SFA). Resulting from this approach is the quantum-orbit model, where each harmonic emission frequency is attributed to a few dominant quantum trajectories evolving in complex time [82].

Consider an atom or a molecule interacting with an external field $\mathbf{E}(t)$.

The TDSE in the length gauge reads

$$i\frac{\partial}{\partial t}\Psi(t) = [H_0 + \mathbf{r}\cdot\mathbf{E}(t)]\Psi, \tag{2.32}$$

with H_0 being the field-free Hamiltonian. The time evolution operator with respect to the interaction operator $\mathbf{r}\cdot\mathbf{E}(t)$ is

$$U(t,0) \;=\; U_0(t,0) \;-\; i\int_0^t dt' U(t,t')\mathbf{r}\cdot\mathbf{E}(t')U_0(t',0), \tag{2.33}$$

where $U_0(t,0)$ is the evolution operator associated with H_0. To simplify the integral in Eq. (2.33), the full evolution operator $U(t,t')$ in the second term is replaced by the Volkov propagator $U_V(t,t')$, which describes the evolution of a free electron in the laser field. This replacement indicates that the influence of the laser field after ionization at time t' is fully taken into consideration, while the effect of the Coulomb potential is neglected. This is the main approximation of the SFA. It relies on the fact that the electric field strength is large enough to dominate the Coulomb term beyond the tunneling point x_0. The Volkov propagator in the length gauge acts as

$$U_V(t,t')|\psi_{PW}(\mathbf{p}+\mathbf{A}(t'))\rangle = \exp\left(-i\int_{t'}^{t} dt''\frac{(\mathbf{p}+\mathbf{A}(t''))^2}{2}\right)|\psi_{PW}(\mathbf{p}+\mathbf{A}(t))\rangle, \tag{2.34}$$

where $|\psi_{PW}(\mathbf{p}+\mathbf{A}(t))\rangle$ is a plane-wave state characterized by electron momentum $\mathbf{k} = \mathbf{p}+\mathbf{A}(t)$. The Volkov propagator $U_V(t,t')$ acts such that a plane wave with momentum $\mathbf{k}' = \mathbf{p}+\mathbf{A}(t')$ evolves to a plane wave with the momentum $\mathbf{k} = \mathbf{p}+\mathbf{A}(t)$ while acquiring an accumulated phase. At each moment, the plane waves form a complete basis:

$$\int d^3p|\psi_{PW}(\mathbf{p}+\mathbf{A}(t))\rangle\langle\psi_{PW}(\mathbf{p}+\mathbf{A}(t))| = 1. \tag{2.35}$$

Thus, within the SFA, the expression for the time evolution operator Eq. (2.33) takes the form

$$U^{SFA}(t,0) \;=\; U_0(t,0) \;-\; i\int_0^t dt' U_V(t,t')\mathbf{r}\cdot\mathbf{E}(t')U_0(t',0). \tag{2.36}$$

Inserting the expression for the Volkov propagator Eq. (2.34) and the identity operator Eq. (2.35) into Eq. (2.36), we obtain the time-dependent wave

function

$$\begin{aligned}
|\Psi(t)\rangle &= U^{SFA}(t,0)|\Psi_0\rangle \\
&= -i\int d^3p \int_0^t dt' \langle\psi_{PW}(\mathbf{p}+\mathbf{A}(t'))|\mathbf{r}\cdot\mathbf{E}(t')|U_0(t',0)|\Psi_0\rangle \\
&\times \exp\left(-i\int_{t'}^t dt'' \frac{(\mathbf{p}+\mathbf{A}(t''))^2}{2}\right)|\psi_{PW}(\mathbf{p}+\mathbf{A}(t))\rangle \\
&+ U_0(t,0)|\Psi_0\rangle. \qquad (2.37)
\end{aligned}$$

Here, we have assumed that the initial state at $t=0$ is the field-free ground state $|\Psi_0\rangle$. The second term in the right-hand side describes the evolution of the initial state under the field-free Hamiltonian. The first term represents the electrons in the continuum. An electron stays in the ground state until time t', when it is released by the laser field into the continuum with the instantaneous kinetic momentum $\mathbf{p}+\mathbf{A}(t')$. Then the electron is accelerated by the laser field until the moment t and reaches the kinetic momentum $\mathbf{p}+\mathbf{A}(t)$.

By neglecting the continuum-continuum transitions, one obtains the time-dependent dipole moment

$$\begin{aligned}
\mathbf{D}(t) &= \langle\Psi(t)|-\mathbf{r}|\Psi(t)\rangle \\
&= -i\int d^3p \int_0^t dt' \mathbf{d}_r^*(\mathbf{p}+\mathbf{A}(t)) d_i(\mathbf{p}+\mathbf{A}(t'),t') \\
&\times \exp(-iS(\mathbf{p},t,t')) + c.c. \qquad (2.38)
\end{aligned}$$

where $S(\mathbf{p},t,t') = \frac{1}{2}\int_{t'}^t dt''(\mathbf{p}+\mathbf{A}(t''))^2 + I_p(t-t')$ is the semiclassical action. The ionization and recombination matrix elements between the ground state and the plane wave are given by

$$d_i(\mathbf{p}+\mathbf{A}(t'),t') = \langle\psi_{PW}(\mathbf{p}+\mathbf{A}(t'))|\mathbf{r}\cdot\mathbf{E}(t')|\Psi_0\rangle, \qquad (2.39)$$

$$\mathbf{d}_r(\mathbf{p}+\mathbf{A}(t)) = \langle\psi_{PW}(\mathbf{p}+\mathbf{A}(t))|-\mathbf{r}|\Psi_0\rangle. \qquad (2.40)$$

It is straightforward to interpret the time-dependent dipole moment (Eq. (2.38)) in the following way:

1. The electron tunnels out from the ground state at time t', with the ionization amplitude given by Eq. (2.39).
2. Then the electron moves freely in the laser field from time t' to t.
3. Finally, the electron recombines to the ground state at time t, described by the recombination dipole of Eq. (2.40).

This is the quantum-mechanical description of the three-step model proposed by Lewenstein [95]. It relies on the following assumptions: (a) The influence of the Coulomb potential on the electron in the continuum is negligible. This assumption is correct when the field strength is large enough to dominate the Coulomb field, which is justified for short-range potentials, e.g., negative ions. It is problematic in the case of neutral atoms or molecules due to the long range of the Coulomb potential. (b) Contributions from excited states are neglected, only the transition between the ground state and the Volkov state is accounted for within the SFA. This is problematic if intermediate resonances play a role in high harmonic generation. Despite of the many flaws and problems regarding the SFA it is often surprisingly successful for producing the basic physical features. Many strong-field phenomena can be described qualitatively by the SFA.

In practice, the calculation of the time-dependent dipole moment can be simplified with the help of the saddle-point approximation [95], since the phase factor $\exp(-iS)$ in the dipole moment osillates rapidly as a function of the momentum $\mathbf{p}$, while the matrix elements in Eqs. (2.39) and (2.40) vary slowly with the momentum $\mathbf{p}$. The saddle-point momentum $\mathbf{p}_s$ makes the phase stationary, i.e. $\nabla_{\mathbf{p}} S(\mathbf{p},t,t')|_{\mathbf{p}=\mathbf{p}_s}=0$, which leads to

$$\mathbf{p}_s(t,t') \;=\; -\frac{1}{t-t'}\int_{t'}^{t}\mathbf{A}(t'')dt''. \tag{2.41}$$

The matrix elements are evaluated at $\mathbf{p}_s$ and the action function $S(\mathbf{p},t,t')$ is replaced by a second-order Taylor expansion in $\mathbf{p}$ at the saddle point $\mathbf{p}_s$

$$S(\mathbf{p},t,t') \;=\; S(\mathbf{p_s},t,t') + \frac{1}{2}\sum_{j,k}\partial_{p_j}\partial_{p_k}S(\mathbf{p},t,t')|_{\mathbf{p}=\mathbf{p_s}}(p_j-p_{sj})(p_k-p_{sk}), \tag{2.42}$$

with $\partial_{p_j}\partial_{p_k}S(\mathbf{p},t,t')|_{\mathbf{p}=\mathbf{p_s}} \;=\; S_{j,k}(t-t')$. After analytical integration over $\mathbf{p}$, the dipole moment reads

$$\begin{aligned}\mathbf{D}(t) \;&=\; -i\int_0^t dt'\left[\frac{2\pi}{\epsilon \,+\, i(t-t')}\right]^{3/2}\\ &\times\; \mathbf{d}_r^*(\mathbf{p}_s(t,t') \,+\, \mathbf{A}(t))d_i(\mathbf{p}_s(t,t') \,+\, \mathbf{A}(t'),t')\\ &\times\; \exp(-iS(\mathbf{p}_s(t,t'),t,t')) \,+\, c.c.,\end{aligned} \tag{2.43}$$

where ϵ is a small cutoff parameter. The factor $[2\pi/(\epsilon \,+\, i(t-t'))]^{3/2}$ describes the spreading of the wave packet during the propagation in the continuum. The second-order Taylor expansion of the action gives a factor $[2\pi/(\epsilon \,+\, i(t-t'))]^{1/2}$

for every spatial dimension.

The harmonic spectrum $I(\Omega)$ can be obtained from the Fourier transform of the dipole moment $\mathbf{D}(t)$:

$$I(\Omega) \propto \Omega^4 |\mathbf{D}(\Omega)|^2 \tag{2.44}$$

with

$$\mathbf{D}(\Omega) = \int dt \mathbf{D}(t) e^{i\Omega t}. \tag{2.45}$$

Inserting Eq. (2.43) into Eq. (2.45), we obtain the analytical expression for $\mathbf{D}(\Omega)$ with the two-dimensional integral over t and t'

$$\begin{aligned} \mathbf{D}(\Omega) &= -i \int_{-\infty}^{\infty} dt \int_0^t dt' \left[\frac{2\pi}{\epsilon + i(t-t')} \right]^{3/2} \\ &\times \mathbf{d}_r^*(\mathbf{p}_s(t,t') + \mathbf{A}(t)) d_i(\mathbf{p}_s(t,t') + \mathbf{A}(t'), t') \\ &\times \exp(-iS(\mathbf{p}_s(t,t'), t, t') + i\Omega t). \end{aligned} \tag{2.46}$$

The matrix elements can be calculated from the bound-state wave function in momentum space $\tilde{\Psi}_0(\mathbf{k})$ as

$$d_i(\mathbf{p}_s + \mathbf{A}(t'), t') = i\mathbf{E}(t) \cdot \nabla_{\mathbf{k}} \tilde{\Psi}_0(\mathbf{k})|_{\mathbf{k}=\mathbf{p}_s+\mathbf{A}(t')}, \tag{2.47}$$

$$\mathbf{d_r}(\mathbf{p}_s + \mathbf{A}(t)) = -i\nabla_{\mathbf{k}} \tilde{\Psi}_0(\mathbf{k})|_{\mathbf{k}=\mathbf{p}_s+\mathbf{A}(t)}. \tag{2.48}$$

The harmonic spectrum from SFA is obtained by numerical integration over times t and t' in Eq. (2.46). It can be further simplified using the saddle-point method for t and t'. The stationary conditions require that the first derivatives of the exponent $S(\mathbf{p}_s(t,t'), t, t') - \Omega t$ in the integrand equal zero, leading to the following equations

$$\left. \frac{\partial S(\mathbf{p}_s(t,t'), t, t')}{\partial t'} \right|_{t'=\tau_i, t=\tau_r} = 0 \Rightarrow \frac{[\mathbf{p}_s(\tau_r, \tau_i) + A(\tau_i)]^2}{2} = -I_p, \tag{2.49}$$

$$\left. \frac{\partial S(\mathbf{p}_s(t,t'), t, t')}{\partial t} \right|_{t=\tau_r, t'=\tau_i} = 0 \Rightarrow \frac{[\mathbf{p}_s(\tau_r, \tau_i) + A(\tau_r)]^2}{2} = \Omega - I_p. \tag{2.50}$$

Eq. (2.41) ensures that electron returns at time τ_r to the same position at time τ_i where it was released, since the velocity integral over time from ionization τ_i to recombination τ_r yields electron displacement from τ_i to τ_r, $\Delta x = \int_{\tau_i}^{\tau_r} (\mathbf{p}_s + \mathbf{A}(t'')) dt'' = 0$. This completes the reduction of the momentum integral to a sum over a few trajectories. Each trajectory has a unique ion-

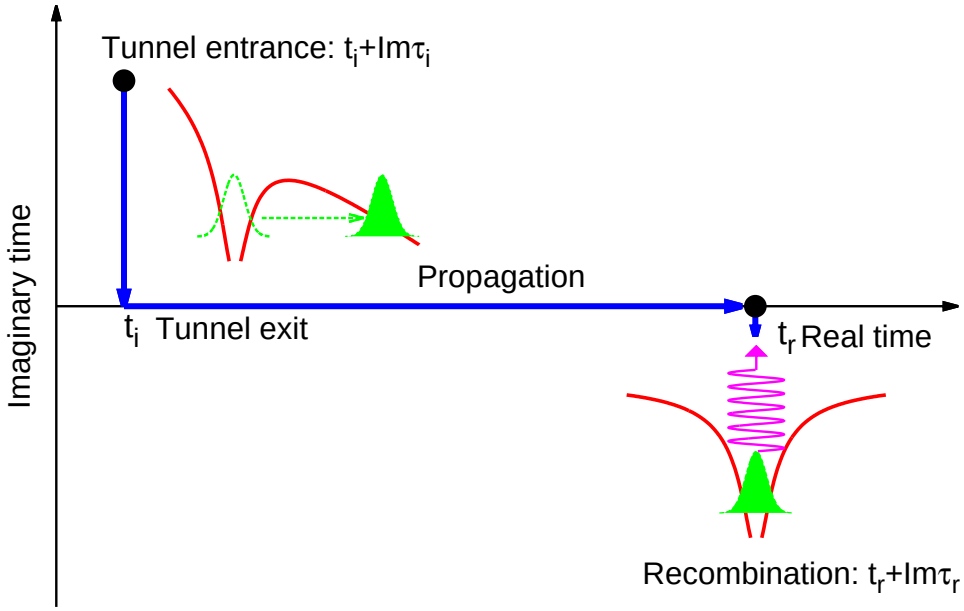

Figure 2.6: Contour of the time-integration in the action. Ionization occurs from complex time τ_i to real time t_i. The electron moves in the continnum from real time t_i to real time t_r. Recombination takes place at the complex time τ_r.

ization time τ_i, recombination time τ_r and photon energy Ω. These trajectories are known as quantum orbits. For each frequency component of the harmonic radiation, only a discrete set of quantum orbits contribute. Eqs. (2.49), (2.50) can be interpreted as energy conservation rules in the process of tunneling and recombination. In Eq. (2.49) the kinetic energy of the electron at the time of birth in the continuum is negative, which is classically impossible, but it can be satisfied formally by a complex-valued ionization time. The solution of Eqs. (2.49), (2.50) are complex ionization time $\tau_i = t_i + \mathrm{Im}\tau_i$ and recombination time $\tau_r = t_r + \mathrm{Im}\tau_r$. The quantum orbits are trajectories with complex saddle-point momenta and complex velocities. They are different from the classical trajectories of the three-step model. The energy of the emitted photon, however, is a real quantity, which could be measured in experiment. The interpretation is that during tunneling, the electron moves in the classical forbidden region so that its velocity is imaginary and the time is complex. The imaginary part of the ionization time τ_i is associated with the tunnel ionization process, and is essentially the Keldysh tunneling time. The physical mechanism associated with the complex times is shown in Fig. 2.6. The electron

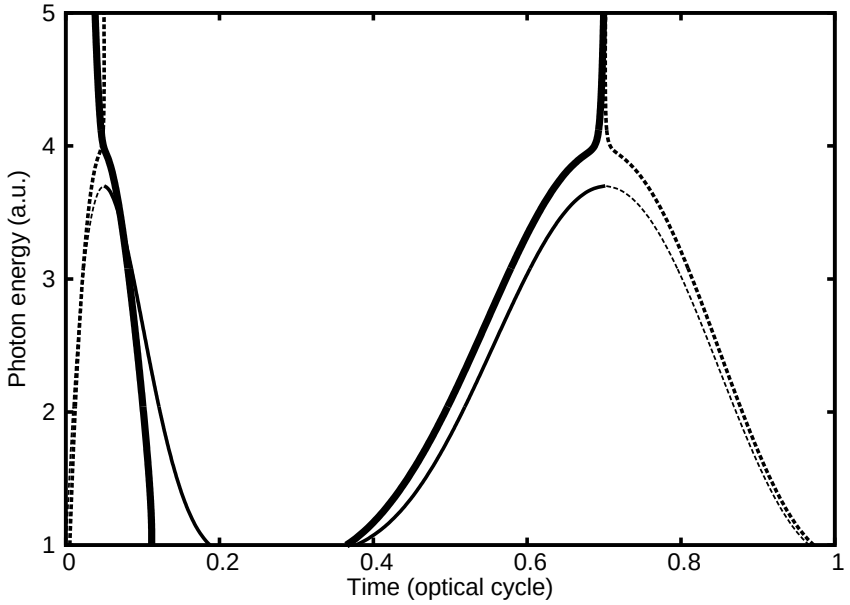

Figure 2.7: Emitted photon energy vs real part of ionization and recombination times for $I_p = 24.58\,\mathrm{eV}$ (He), using an 800 nm laser field with an intensity of $I{=}4{\times}10^{14}\,\mathrm{W/cm^2}$. Full and dashed lines correspond to the short and long trajectories, respectively. The thin (thick) lines represent the results from the three-step model (quantum-orbit model).

starts tunneling at time τ_i. As it moves under the barrier, the imaginary component of time decreases. When the imaginary part reaches zero, the electron exits the barrier. Afterwards the electron moves in the oscillating laser field from the real time t_i to t_r. Similarly, the recombination occurs from the real time t_r to the complex time τ_r. The imaginary part $\mathrm{Im}\tau_r$ of the recombination time is usually very small.

In Fig. 2.7, the emitted photon energies are shown versus the real part of ionization and recombination times. As in the classical three-step model, there are at least two solutions for every harmonic frequency, namely, the short and long trajectories. The trajectories merge near the photon energy $\Omega = 1.32I_p + 3.17U_p$ [95], which yields a more precise description of the cutoff position in the harmonic spectrum, arising from the more rigorous quantum-mechanical calculation. Pronounced differences between the quantum-orbit model and the classical model are found especially for the short trajectory. The quantum-orbit model predicts much earlier ionization times for the short trajectory except for the region around the cutoff.

In Fig. 2.8, the imaginary parts of ionization and recombination times are

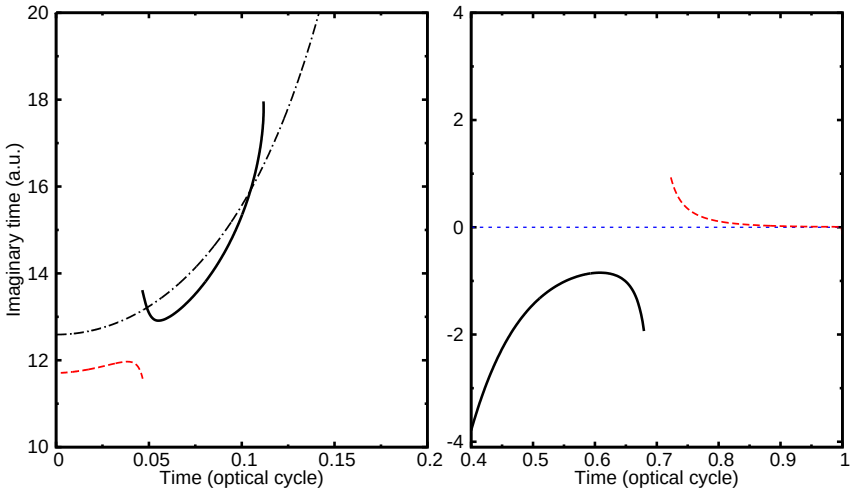

Figure 2.8: Imaginary part of ionization times (left) and recombination times (right) as a function of real parts. Solid lines represent the results for short trajectories and dashed lines for long trajectories. The dot-dashed line shows the Keldysh tunneling time $\sqrt{2I_p}/|E(t_i)|$, see Eq. (2.21). The simulation parameters are the same as in Fig. 2.7.

shown. Also shown is the Keldysh tunneling time as defined in Eq. (2.21). For the short trajectory, the Keldysh tunneling time agrees well with the quantum-orbit model. The discrepancy near the cut-off region is due to the invalidity of the saddle-point approximation. Here the second-order derivative of the action with respect to the return time equals zero and the uniform approximation is required [96, 97]. The imaginary part of the recombination times is very small compared to that of the ionization times. Note the different scales in the left and right panels of Fig. 2.8.

To evaluate the integration over t and t' in Eq. (2.46), the classical action $S(\mathbf{p}_s, t', t) - \Omega t$ is expanded up to second order around the saddle points τ_r and τ_i as

$$\begin{aligned} S(\mathbf{p}_s, t, t') - \Omega t &= S(\mathbf{p}_s, \tau_r, \tau_i) - \Omega\tau_r \\ &+ \frac{1}{2} S''_{t,t}(\mathbf{p}_s, t, t')\big|_{\substack{t=\tau_r \\ t'=\tau_i}} (t-\tau_r)^2 \\ &+ S''_{t,t'}(\mathbf{p}_s, t, t')\big|_{\substack{t=\tau_r \\ t'=\tau_i}} (t-\tau_r)(t'-\tau_i) \\ &+ \frac{1}{2} S''_{t',t'}(\mathbf{p}_s, t, t')\big|_{\substack{t=\tau_r \\ t'=\tau_i}} (t'-\tau_i)^2, \end{aligned} \tag{2.51}$$

with

$$S''_{t,t}(\mathbf{p}_s,t,t')\big|_{\substack{t=\tau_r\\t'=\tau_i}} = -\left(\mathbf{p}_s(\tau_r,\tau_i)+A(\tau_r)\right)\left[\frac{\mathbf{p}_s(\tau_r,\tau_i)+A(\tau_r)}{\tau_r-\tau_i}+E(\tau_r)\right], \tag{2.52}$$

$$S''_{t,t'}(\mathbf{p}_s,t,t')\big|_{\substack{t=\tau_r\\t'=\tau_i}} = \left(\mathbf{p}_s(\tau_r,\tau_i)+A(\tau_i)\right)\frac{\mathbf{p}_s(\tau_r,\tau_i)+A(\tau_r)}{\tau_r-\tau_i}, \tag{2.53}$$

$$S''_{t',t'}(\mathbf{p}_s,t,t')\big|_{\substack{t=\tau_r\\t'=\tau_i}} = -\left(\mathbf{p}_s(\tau_r,\tau_i)+A(\tau_i)\right)\left[\frac{\mathbf{p}_s(\tau_r,\tau_i)+A(\tau_i)}{\tau_r-\tau_i}-E(\tau_i)\right]. \tag{2.54}$$

Note that the ionization matrix element in Eq. (2.47) has a pole at the saddle point τ_i for hydrogen-like atoms [98–101]. The integration over t' can be evaluated using a generalized saddle-point formula as in [98] or a Gaussian wavefunction in the definition of the ionization matrix element [95, 100]. Within the saddle-point approximation, the expression for the harmonic amplitude yields

$$a(\Omega) = -i\sum_{j=1}^{N} A_j \exp(-iS(\mathbf{p}_s,\tau_r,\tau_i)+i\Omega\tau_r) \tag{2.55}$$

with A_j including all the integral coefficients. Since there are several trajectories for each Ω during each half cycle of the laser field, the sum includes all the contributing trajectories. Depending on the relative phase between the short and long trajectories, they can interfere constructively or destructively.

2.4 Numerical method

In this section, we discuss the numerical method used in this work. We describe the numerical approach to solve the TDSE on a space-time grid and the calculation of observables.

2.4.1 Split-operator method

The split-operator method was first proposed by Feit and co-workers in 1982 [102]. The evolution of the wave packet from the intial state $\Psi(t=0)$ to time t is given by integration of Eq. (2.17) or (2.19)

$$|\Psi(t)\rangle = \mathcal{T}\exp\left[-i\int_0^t dt' H(t')\right]|\Psi(t=0)\rangle, \tag{2.56}$$

with $\mathcal{T}$ being the time-ordering operator. If a very small time step Δt is taken, the time-dependent Hamiltonian is considered to be time-independent during

Δt, then the propagation operator becomes

$$|\Psi(t+\Delta t)\rangle = e^{-iH(t)\Delta t}|\Psi(t)\rangle. \tag{2.57}$$

The Hamiltonian in both the length and velocity gauge consists of two parts: the momentum-dependent part and the position-dependent part, which are diagonal in their respective representations. From a numerical point of view, it is therefore desirable to split the full time-evolution operator into a product of momentum-dependent and position-dependent terms. With the help of the Baker-Campbell-Hausdorff formula [90] for two noncommuting operaters,

$$e^A e^B = e^{A+B+\frac{1}{2}[A,B]+\frac{1}{12}([A,[A,B]]+[B,[A,B]])+\text{high order commutator}}, \tag{2.58}$$

with the commutator $[A,B] = AB - BA$, the propagation operator in the length gauge is expressed as

$$e^{-iH(t)\Delta t} = e^{-i\mathscr{V}(t)\frac{\Delta t}{2}} e^{-i\frac{\mathbf{p}^2}{2}\Delta t} e^{-i\mathscr{V}(t)\frac{\Delta t}{2}} + \mathcal{O}(\Delta t^3), \tag{2.59}$$

where $\mathscr{V}(t)$ is position-dependent and includes the laser-electron interaction. By neglecting the high-order term $\mathcal{O}(\Delta t^3)$, evolution of the wave packet during each time interval Δt is accomplished with the following steps:

1. The evolution of the wave packet starts in position space; it is multiplied with the position-dependent operator $e^{-i\mathscr{V}(t)\frac{\Delta t}{2}}$.
2. The wave packet is transformed to momentum space and then multiplied by the momentum-dependent operator $e^{-i\frac{\mathbf{p}^2}{2}\Delta t}$.
3. The wave packet is transformed back to position space and then multiplied again with the last term of the operator $e^{-i\mathscr{V}(t)\frac{\Delta t}{2}}$.

In practice, the transformation between position space and momentum space is performed by the fast Fourier transformation (FFT) routines. The FFTW package (www.fftw.org) is used to implement the Fourier transforms in one, two and three dimensional simulations in this work.

For numerical calculations, one should choose the parameters in such a way that the results do not change substantially when the calculation is made more accurate. To ensure the convergence of the numerical simulation, several aspects have to be taken into account:

The grid in position space should be sufficiently large so that a further increase of the grid size does not change the observable quantities of interest. Depending on the problem to be investigated, different methods are used in the

propagation procedure. When the harmonic spectrum is simulated, one can apply absorbing boundaries to avoid the reflection of the wave packet at the boundary. A grid larger than the classical quiver amplitude of a free electron in the laser field is enough, since electrons that undergo direct ionization without recollision, do not contribute to the harmonic generation. For the calculation of electron momentum distributions, a much larger grid size is required to cover all the electrons in the continuum. A more efficient approach was proposed with the idea of splitting the position space into inner and outer parts [103, 104]. In the inner part, the wave function is propagated exactly by means of the split-operator method. Electrons in the outer part do not interact with the core any more. Thus they are considered as free electrons in the laser field. The wave packet in the outer part needs to be propagated in the momentum space only. The choice of the grid spacing $\Delta x{=}\pi/p_{\max}$ is determined by the maximum momentum $p_{\max}$ that is relevant in the problem.

The evolution of the wave packet starts from the ground state of an atom or a molecule. The ground state is obtained by using imaginary-time propagation [105]. Replacing the real time step Δt by the imaginary time step $-i\Delta\tau$, the propagation operator becomes $e^{-H\Delta\tau}$. We begin with an arbitrary wave packet $|\Phi_0\rangle$ and propagate in imaginary time. Expanding the initial wave packet in terms of the eigenstates $|\psi_n\rangle$ of the field-free Hamiltonian H_0 with eigenvalues E_n, the wave packet at time t is

$$|\Phi(t)\rangle = \sum_n a_n \exp(-iE_n t)|\psi_n\rangle \tag{2.60}$$

with $a_n = \langle\psi_n \,|\, \Phi_0\rangle$. The wave packet after one imaginary time step becomes

$$|\Phi(\tau + \Delta\tau)\rangle = \sum_n a_n e^{-E_n(\tau+\Delta\tau)}|\psi_n\rangle. \tag{2.61}$$

The state with the lowest negative energy, i.e. the ground state, becomes exponentially dominant after many imaginary time steps starting from an arbitary wave packet. The wave packet is renormalized after each propagation step, and the energy of the wave packet can be calculated either from the expectation value of the Hamiltonian

$$E \;=\; \langle\Phi(\tau)|\frac{\mathbf{p}^2}{2} \;+\; \mathscr{V}(t)\,|\Phi(\tau)\rangle, \tag{2.62}$$

or from the decay of the norm after one step,

$$E = -\frac{1}{2\Delta\tau}\ln\left(\frac{\langle\Phi(\tau+\Delta\tau)|\Phi(\tau+\Delta\tau)\rangle}{\langle\Phi(\tau)|\Phi(\tau)\rangle}\right). \tag{2.63}$$

When the contributions from other states are negligible, i.e. the energy difference of two sequential steps is smaller than 10^{-14} a.u., the wave packet is considered to be converged to the ground state $|\Psi_0\rangle$.

According to the quantum mechanical theory, once the time-dependent wavefuction is known, any observable quantity can be obtained as the expectation value of the operator corresponding to the quantity observed in laboratory. In the following, the simulation of the high-order harmonic spectrum is shown as an example in strong-field physics.

2.4.2 Harmonic spectrum

According to classical electrodynamics, the radiation intensity from an oscillating dipole is proportional to the modulus squared of the Fourier transform of the dipole acceleration, which corresponds in quantum mechanics to the second derivative of the expectation value of the electron position,

$$\mathbf{a}(t) = -\frac{d^2}{dt^2}\langle\Psi(t)|\mathbf{r}|\Psi(t)\rangle. \tag{2.64}$$

Applying the Ehrenfest theorem, which relates the time derivative of the expectation value of an operator to the commutator of that operator with the Hamiltonian of the system, one obtains

$$\frac{d}{dt}\langle\Psi(t)|\mathbf{r}|\Psi(t)\rangle = -i\langle\Psi(t)|[\mathbf{r},H]|\Psi(t)\rangle, \tag{2.65}$$

$$\frac{d}{dt}\langle\Psi(t)|\mathbf{p}|\Psi(t)\rangle = -i\langle\Psi(t)|[\mathbf{p},H]|\Psi(t)\rangle. \tag{2.66}$$

with the commutation relations $[\mathbf{r},H] = i\mathbf{p}$ and $[\mathbf{p},H] = -i(dV(\mathbf{r})/d\mathbf{r} + \mathbf{E}(t))$ (in the length gauge) yields

$$\mathbf{a}(t) = -\frac{d}{dt}\langle\Psi(t)|\mathbf{p}|\Psi(t)\rangle \tag{2.67}$$

and

$$\mathbf{a}(t) = \langle\Psi(t)|\frac{dV(\mathbf{r})}{d\mathbf{r}} + \mathbf{E}(t)|\Psi(t)\rangle. \tag{2.68}$$

In practice, the dipole acceleration $\mathbf{a}(t)$ can be calculated from either the dipole moment $\mathbf{D}(t)$,

$$\mathbf{a}(t) \;=\; \ddot{\mathbf{D}}(t) = -\frac{d^2}{dt^2}\langle\Psi(t)|\mathbf{r}|\Psi(t)\rangle, \tag{2.69}$$

dipole velocity (time-derivate of the dipole moment) $\dot{\mathbf{D}}(t)$,

$$\mathbf{a}(t) \;=\; \ddot{\mathbf{D}}(t) = -\frac{d}{dt}\langle\Psi(t)|\mathbf{p}|\Psi(t)\rangle, \tag{2.70}$$

or directly as

$$\mathbf{a}(t) \;=\; \ddot{\mathbf{D}}(t) = \langle\Psi(t)|\frac{d}{d\mathbf{r}}V(\mathbf{r}) + \mathbf{E}(t)|\Psi(t)\rangle. \tag{2.71}$$

Then the harmonic spectrum can be calculated with the different forms of the dipole acceleration in Eqs. (2.64), (2.67) and (2.68),

$$S(\Omega) = \left|\int_{-\infty}^{\infty} \mathbf{a}(t)e^{i\Omega t}dt\right|^2. \tag{2.72}$$

The corresponding expressions are referred to as "length", "velocity" or "acceleration" forms of the harmonic spectrum. They are physically equivalent and give the same result if the wave function is obtained directly by numerical solution of the TDSE.

In experiment, the measured macroscopic harmonic signal is sensitive to the phase-matching conditions. The short or long trajectory can be selected by positioning the laser focus before or after the gas jet [106]. In numerical simulations, the harmonic signal from different trajectories can be separated by the Gabor transform of the dipole acceleration moment, instead of the Fourier transform. With the help of the Gabor transform, we analyze the harmonic radiation as a function of harmonic order and emission times. The Gabor time-frequency distribution is defined as

$$S_G(\Omega, t) = \left|\int_{-\infty}^{\infty} \mathbf{a}(t') \exp\left[-\frac{(t'-t)^2}{2\sigma^2}\right] e^{i\Omega t'} dt'\right|^2. \tag{2.73}$$

The parameter $\sigma = 1/(3\omega)$ is chosen to give satisfactory resolutions in both the temporal and frequency domains [107]. It is possible to extract the emission times of harmonic radiation from the Gabor distribution. The emission times for a given harmonic frequency is considered to be at the local maxima of the Gabor intensity when viewed as a function of time t for fixed frequency Ω.

2.4.3 Photoelectron spectrum

The photoelectron spectrum can be calculated using the spectral method, in which the wave packet at the end of the action of the laser field (time t_0) is propagated further in time without external field until a final time t_f. The wave packet after time t_0 can be expanded in the eigenstates of the field-free Hamiltonian as

$$|\Psi(t)\rangle = \sum_n a_n e^{-iE_n(t-t_0)} \,|\, \psi_n\rangle, \tag{2.74}$$

with $a_n = \langle\psi_n|\Psi(t_0)\rangle$. The time-dependent autocorrelation function for wave packets is calculated as

$$C(t) = \langle\Psi(t_0) \,|\, \Psi(t)\rangle = \sum_n |a_n|^2 \, e^{-iE_n(t-t_0)}. \tag{2.75}$$

The Fourier transform of the autocorrelation function yields the total energy spectrum

$$\begin{aligned} \sigma(E) &= \frac{1}{2\pi} \int_{-\infty}^{\infty} C(t)\, e^{iE(t-t_0)}\, dt \\ &= \sum_n |a_n|^2\, \delta(E - E_n), \end{aligned} \tag{2.76}$$

with the integral over times from $-\infty$ to ∞. In the simulation, we have the autocorrelation function for $t \geqslant t_0$. It can be extended to times before t_0 by taking the complex conjugate of the autocorrelation function

$$C(t') \,=\, C^*(t) \quad \text{for} \quad t' < t_0 \tag{2.77}$$

with $t_0 - t' = t - t_0$. Then the energy spectrum of Eq. (2.76) becomes

$$\sigma(E) \,=\, \frac{1}{\pi}\, \mathrm{Re} \lim_{t_f \to \infty} \int_{t_0}^{t_f} C(t)\, e^{iE(t-t_0)}\, dt \tag{2.78}$$

In practice, a sufficiently long time interval is required for the simulation to guarantee sufficient energy resolution. The photoelectron spectrum is the part of $\sigma(E)$ corresponding to the continuous part of the eigenenergy spectrum. By choosing a suitable initial wave packet, the autocorrelation function can also be used to obtain the discrete bound-state energy levels of the unperturbed system.

Chapter 3

Ionization and return times in HHG

3.1 Introduction

Recently, the exact exit times of electrons producing high-harmonic radiation have been revealed by high-harmonic spectroscopy [48]. The experiment has shown that the times at which electrons exit from the atom are well reproduced by the quantum-orbit model [82] and they are substantially different from the purely classical trajectory model [3]. A weak second harmonic field polarized perpendicular to the laser field was applied to manipulate the electron trajectory in two dimensions. In the experiment, however, there are two uncertainties. First, applying the quantum-orbit model requires knowledge of the laser intensity, which is difficult to measure accurately. Second, the absolute value of the phase difference between the two fields (the two-color delay) was not measured in the experiment. Instead, the absolute scale was determined by requiring minimal averaged deviation of the retrieved return times from the quantum-orbit return times. To overcome these limitations, we follow a theoretical approach based on the numerical solution of the TDSE. There is no obvious way to extract the ionization times directly from the quantum mechanical wave function. In this work, we follow precisely the experimental procedure, but without uncertainty about laser intensity or two-color delay.

We start with the discussion on the mechanism of harmonic generation from the orthogonally polarized two-color field, i.e. the generation of orthogonally polarized odd and even harmonics. We calculate the single-atom harmonic spectrum from the short trajectory for varying two-color delay using the Gabor transform. Then we analyze the variations of harmonic intensity and amplitude ratio of neighboring even and odd harmonics as a function of the two-color delay. We find that the optimized two-color delays, corresponding to the maxima of the harmonic intensity and the amplitude ratio, deviate significantly from the predictions of the quantum-orbit model when we

use the real parts of the quantum-orbit times combined with classical modeling of the electron dynamics in the two-color field proposed in [48]. We introduce an improved quantum mechanical model based on two-dimensional electron trajectories evolving in complex time. The results agree well with our TDSE simulations. We carry out both 2D and 3D simulations to show that the temporal properties of laser-induced tunnel ionization are independent of the dimensions of the simulation, i.e. independent of the particular choice of potential. Using the quantum mechanical model, we retrieve the ionization and return time for each harmonic order. Furthermore, we use this two-color scheme to retrieve the tunneling time, which we define as the imaginary part of the complex ionization time in the quantum-orbit model.

3.2 HHG from two-color field

We have discussed harmonic generation from a linearly polarized laser field in Chapter 2. In this section, we present harmonic radiation from an orthogonally polarized two-color field. The fundamental pulse is linearly polarized along the x-axis, whereas the second harmonic field is polarized along the y-axis with relative amplitude ε. The electric field $\mathbf{E}(t)$ is expressed as

$$\mathbf{E}(t) \;=\; E_0 \left[\mathbf{e}_x \cos(\omega t) \;+\; \mathbf{e}_y \varepsilon \cos(2\omega t \;+\; \phi)\right], \tag{3.1}$$

where ϕ is the two-color delay. E_0 and ω are the amplitude and frequency of the main field with wavelength 800 nm.

Since the second harmonic field is weak, tunneling is determined by the main field. Once the electron is released from the atom by the main field, the free electron is accelerated by the combined electric field and is then driven to recollide with the parent ion at an angle α, as in Fig. 3.1. The harmonics are emitted with their polarization at an angle θ with respect to x-axis. The lateral electron motion results in the modulation of the harmonic signal as a function of the two-color delay and the production of even harmonics.

3.2.1 Harmonic spectrum

The classical motion of the electron after tunneling is illustrated for two subsequent half-cycles by the blue dashed lines in Fig. 3.1. The radiation process repeats every half-cycle of the main laser field. In the following we will analyze the x- and y-components of the harmonic radiation with the help of the classical picture. From one half cycle to the next half cycle of the fundamental field, the harmonic field along x exhibits a sign change. Thus, upon Fourier

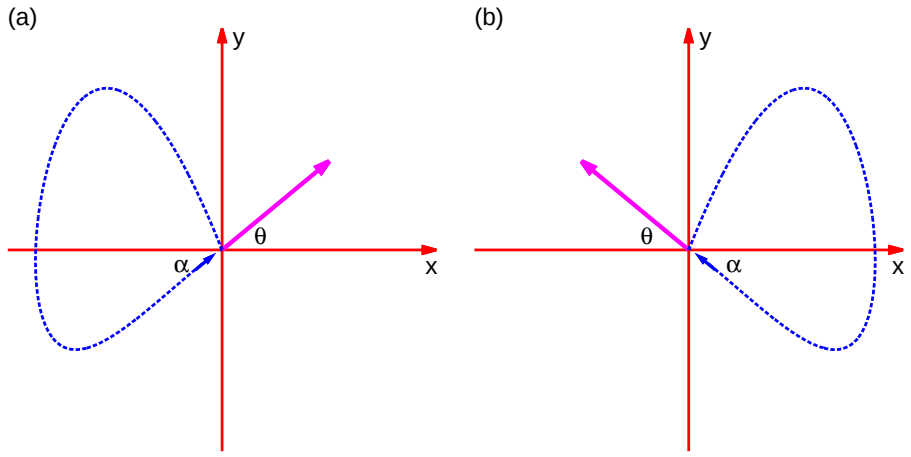

Figure 3.1: Schematic diagrams of the two trajectories caused by the two-color field in two subsequent half-cycle of the main field. The main and second-harmonic fields are polarized along x-axis and y-axis respectively. The dashed curves represent the electron trajectories in the continuum. The solid arrow indicates the polarization of the harmonic radiation.

transformation to the frequency domain, the harmonics polarized along x are at odd multiples of the fundamental frequency (Eq. (2.31)). In contrast, the harmonic field along y is periodic for every half-cycle

$$E_{Hy}(t) = E_{Hy}(t + \frac{T}{2}). \tag{3.2}$$

Upon Fourier transformation to the frequency domain, the harmonics polarized along y are

$$E_{Hy}(\Omega) = \sum_n e^{in\Omega\frac{T}{2}} \int_0^{\frac{T}{2}} E_{Hy}(t) e^{i\Omega t} dt. \tag{3.3}$$

Constructive interference occurs when

$$\frac{\Omega}{2} T = 2m\pi, \quad m = 0, 1, \ldots, \tag{3.4}$$

i.e. at even multiples of the fundamental laser frequency. The generation of even harmonics polarized along the y-axis can also be explained by the fact that the presence of the orthogonally polarized second-harmonic field breaks the inversion symmetry.

Then we calculate the harmonic spectrum from a model helium atom. Within the single-active-electron approximation, the TDSE for the wave func-

tion $\Psi(\mathbf{r},t)$ in the length gauge reads

$$i\,\partial_t\,\Psi(\mathbf{r},t) = \left[\frac{\mathbf{p}^2}{2} + V(\mathbf{r}) + \mathbf{r}\cdot\mathbf{E}(t)\right]\Psi(\mathbf{r},t) \tag{3.5}$$

with the two-dimensional (2D) atomic potential

$$V(\mathbf{r}) = -\frac{1}{\sqrt{\mathbf{r}^2+\epsilon}}, \tag{3.6}$$

or the three-dimensional (3D) atomic potential

$$V(\mathbf{r}) = -\frac{1+e^{-\beta r}}{\sqrt{\mathbf{r}^2+\alpha}}, \tag{3.7}$$

where $\mathbf{r}$ is the electron coordinate. The soft-core parameters ϵ=0.0678, α=1e-5 and β=1.38 are chosen to reproduce the ionization potential of real helium atom (I_p=24.6 eV). Here we use a 10-cycle pulse of 800 nm wavelength such that the calculated spectrum yields well-separated harmonic peaks, rather than a continuous spectrum. The electric field envelope is trapezoidal with a two-cycle turn on and off. The TDSE is solved using the split-operator method [102] with 2048 time steps per optical cycle, starting from the ground state as obtained by imaginary-time propagation [105]. We use a grid size of 200×200 a.u. with spacing of Δ_x=Δ_y=0.2 a.u. in the 2D simulation, and a grid size of 100×100 a.u. with spacing of Δ_x=Δ_y=0.39 a.u. in the 3D simulation. Absorbing boundaries are used to avoid unphysical reflections of the wave packet at the borders.

The dipole acceleration $\mathbf{a}(t)$ is calculated using Eq. (2.68). The x- and y-components of the harmonic spectra are obtained separately from the x- and y-components of the dipole acceleration $\mathbf{a}(t)$,

$$S_{x,y}(\Omega) = \left|\int a_{x,y}(t)e^{i\Omega t}dt\right|^2. \tag{3.8}$$

The total harmonic intensity is evaluated as

$$S(\Omega) = S_x(\Omega) + S_y(\Omega). \tag{3.9}$$

The x- and y-components of the harmonic spectra with the two-color delay ϕ=0 are shown in Fig. 3.2. Well-defined plateaus and clear cut-offs are found in both components. The cut-off positions agree well with the cut-off law, i.e. $\Omega_{\text{cutoff}} = 1.32I_p + 3.2U_p$, which predicts the maximum harmonic order of

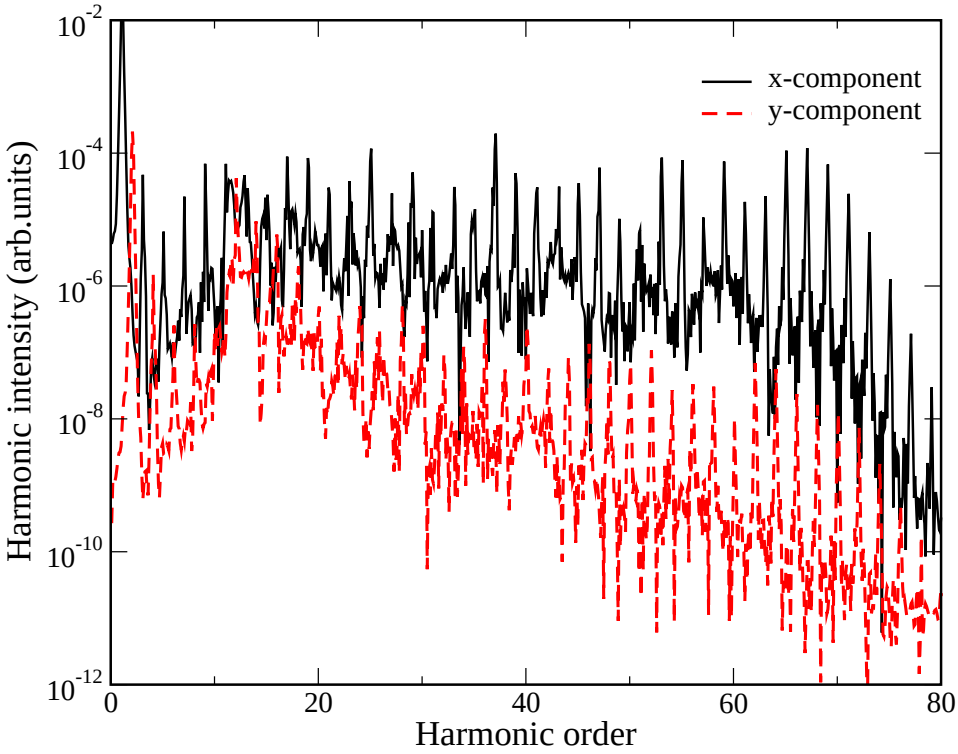

Figure 3.2: HHG spectra for the 2D model helium atom in the presence of the orthogonally polarized two-color field. The laser intensity is $4\times10^{14}\,\mathrm{W/cm^2}$ with zero two-color delay. Solid line represents the x-component of the harmonic field; dashed line represents the y-component of the harmonic field.

69. Odd harmonics are generated along the x-axis as expected, whereas even harmonics are produced along the y-axis.

For each harmonic frequency, the harmonic signal includes contributions from more than one trajectory. Interference of multiple trajectories leads to the modulation of the harmonic signal in the plateau region. Due to the dispersion of the wavepacket in the continuum, the two shortest trajectories play a dominant role, i.e. the so-called short and long trajectories. Under the commonly used experimental conditions, the short trajectory is favored by phase-matching conditions. In numerical simulations, with the help of the Gabor transform, one obtains the harmonic radiation as a function of emission time. Contributions from short and long trajectories correspond to different emission times, and can therefore be distinguished in the Gabor distribution.

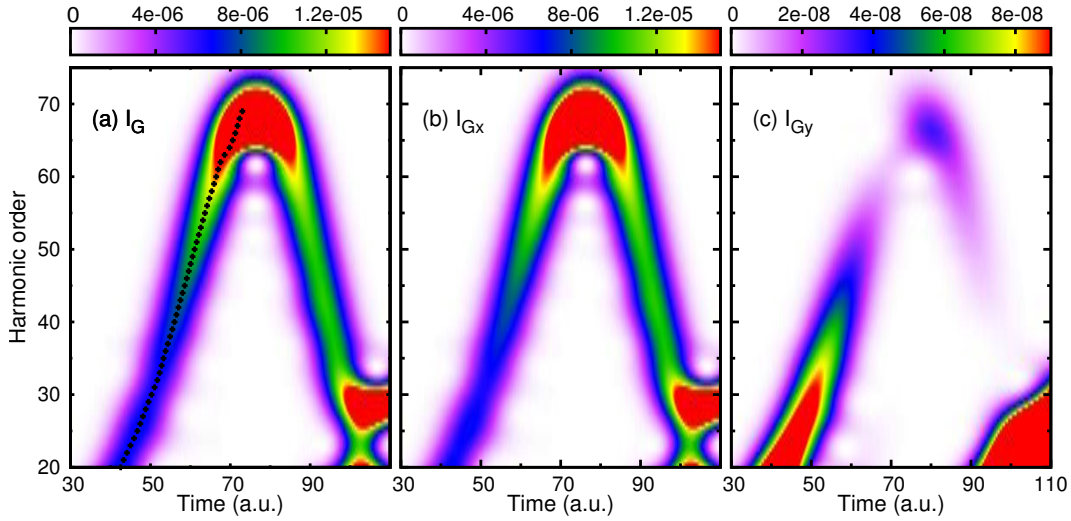

Figure 3.3: Gabor distributions of the generated harmonics as a function of harmonic order and emission time. (a) Total harmonic field; (b) x-component of harmonic field; (c) y-component of harmonic field. Dots represent the obtained emission times of harmonic radiation. The laser intensity is the same as in Fig. 3.2. Time zero corresponds to the maximum of the electric field.

3.2.2 Time-frequency analysis

Using the Gabor time-frequency analysis, the harmonic intensity as a function of harmonic frequency Ω and emission time t is obtained separately for the x- and y-component

$$I_{\mathrm{G}x,y}(\Omega,t) = \left| \int dt' a_{x,y}(t') \, \exp[-(t-t')^2/(2\sigma^2) + i\,\Omega\,t'] \right|^2 . \tag{3.10}$$

The total harmonic intensity at time t is $I_{\mathrm{G}}(\Omega,t) = I_{\mathrm{G}x}(\Omega,t) + I_{\mathrm{G}y}(\Omega,t)$.

In the following simulations, we apply a total duration of 3 optical cycles and one-cycle linear ramps for the trapezoidal profile of the electric field. With this laser pulse, we perform the Gabor time-frequency analysis on trajectories that are born in the first half-cycle of the central part of the trapezoidal pulse. We analyze the emission of harmonics with energies above the ionization threshold. The Gabor distributions of the generated fields are shown in Fig. 3.3. The short and long trajectories [95] are well separated except in the cutoff region, where the contributions from the short and long trajectories are coherently superimposed. The short trajectories correspond to harmonics emitted at times from 40 a.u. to 75 a.u., with the photon energy monotonically increasing with the return time. The long trajectories correspond to harmonics

emitted during a relatively shorter time interval from 75 a.u. to 100 a.u. with a return energy that decreases with the emission time.

In order to compare directly with the experimental results [48], we will concentrate on harmonic radiation from the short trajectory. For a given harmonic frequency, the emission time t_r is taken to be at the local maximum of the Gabor intensity as a function of time. For these emission times $t_r(\Omega)$, the harmonic intensities of the x-component and y-component associated with the short trajectories are obtained from the Gabor transforms of the two dipole-acceleration components at time t_r

$$I_{Gx}(\Omega, t_r) = \left| \int dt' a_x(t') \, \exp[-(t_r - t')^2/(2\sigma^2) + i\,\Omega\, t'] \right|^2 , \tag{3.11}$$

and

$$I_{Gy}(\Omega, t_r) = \left| \int dt' a_y(t') \, \exp[-(t_r - t')^2/(2\sigma^2) + i\,\Omega\, t'] \right|^2 . \tag{3.12}$$

They correspond to the radiation intensities of odd and even harmonics measured in the experiment [48]. Near the cutoff, the short and the long trajectories merge together. It is therefore necessary to fit the numerical Gabor intensity for each harmonic order to a coherent sum of two Gaussians as

$$I_{\rm fit}(\Omega) \; = \; \left| \alpha_1 \exp\Big[- \frac{(t-\beta_1)^2}{2\sigma_1^2} \Big] \; + \; \alpha_2 e^{i\theta_2} \exp\Big[- \frac{(t-\beta_2)^2}{2\sigma_2^2} \Big] \right|^2 . \tag{3.13}$$

The emission times for short trajectories are taken as the smaller value of the fitting parameters β_1 and β_2, with their corresponding harmonic intensities α_1^2 and α_2^2. The emission times $t_r(\Omega)$ extracted from the Gabor distribution are shown in Fig. 3.3(a). To retrieve two quantities, namely ionization time and return time, from the HHG spectra, we require two observables per harmonic order. They are the harmonic intensity and the recollision angle, as proposed in [48].

3.2.3 Harmonic intensity

We start the analysis with a classical description of the electron lateral motion in the continuum. Since the second harmonic field is weak, it is considered as a perturbation compared to the main field, thus it mostly affects the electron after tunneling. The equation of motion for the laser-driven free

electron in the y direction is

$$\ddot{y}(t) \;=\; -\varepsilon E_0 \cos\left(2\omega t \;+\; \phi\right). \tag{3.14}$$

Integration of Eq. (3.14) yields the electron's instantaneous displacement in y direction

$$y(t) \;=\; \frac{\varepsilon E_0}{4\omega^2}\left[\cos\varphi(t) \;-\; \cos\varphi_i \;+\; (\varphi(t)-\varphi_i)\sin\varphi_i\right] \;+\; v_{y0}(t-t_i), \tag{3.15}$$

with $\varphi_i \;=\; 2\omega t_i \;+\; \phi$ and $\varphi(t) \;=\; 2\omega t \;+\; \phi$, and v_{y0} is the initial velocity along the y-axis at the moment of ionization t_i. Note that the ionization time t_i and return time t_r are determined by the main field. Recombination is possible if the electron returns at time t_r to the position where it was released at time t_i, i.e. $y(t_r) - y(t_i) = 0$. The required initial velocity in the y-direction is

$$v_{y0}(t_i, t_r, \phi) \;=\; -\frac{\varepsilon E_0}{2\omega}\left[\sin\varphi_i + \frac{\cos\varphi_r \;-\; \cos\varphi_i}{2\omega(t_r - t_i)}\right], \tag{3.16}$$

with $\varphi_r = 2\omega t_r \;+\; \phi$. The corresponding electron velocity at the return time t_r is

$$v_y(t_r) \;=\; -\frac{\varepsilon E_0}{2\omega}\left[\sin\varphi_r + \frac{\cos\varphi_r \;-\; \cos\varphi_i}{2\omega(t_r - t_i)}\right]. \tag{3.17}$$

For each ionization time t_i, the wave packet created by tunnel ionization as a function of the initial lateral velocity v_{y0} is approximated as [108, 109]

$$\Psi(v_{y0}) \;\propto\; P(v_{y0}) \exp\left(-\frac{v_{y0}^2}{2}\frac{\sqrt{2I_p}}{|E_x(t_i)|}\right), \tag{3.18}$$

with $E_x(t_i)$ being the instantaneous electric field of the main field. The prefactor $P(v_{y0})$ depends sensitively on details of the initial bound state. The dependence of the tunneling probablity on the initial lateral velocity v_{y0} leads to the reduction of the harmonic yields as,

$$I_{\mathrm{HG}}(\Omega) \;\propto\; \exp\left(-v_{y0}^2(t_i, t_r, \phi)\frac{\sqrt{2I_p}}{|E_x(t_i)|}\right). \tag{3.19}$$

For each harmonic order, the harmonic intensity depends on the ionization time t_i, return time t_r and the two-color delay ϕ. Eq (3.19) shows that the harmonic radiation efficiency is maximized for vanishing v_{y0} [110, 111]. Based on Eq. (3.19) together with the classical analysis of the electron dynamics

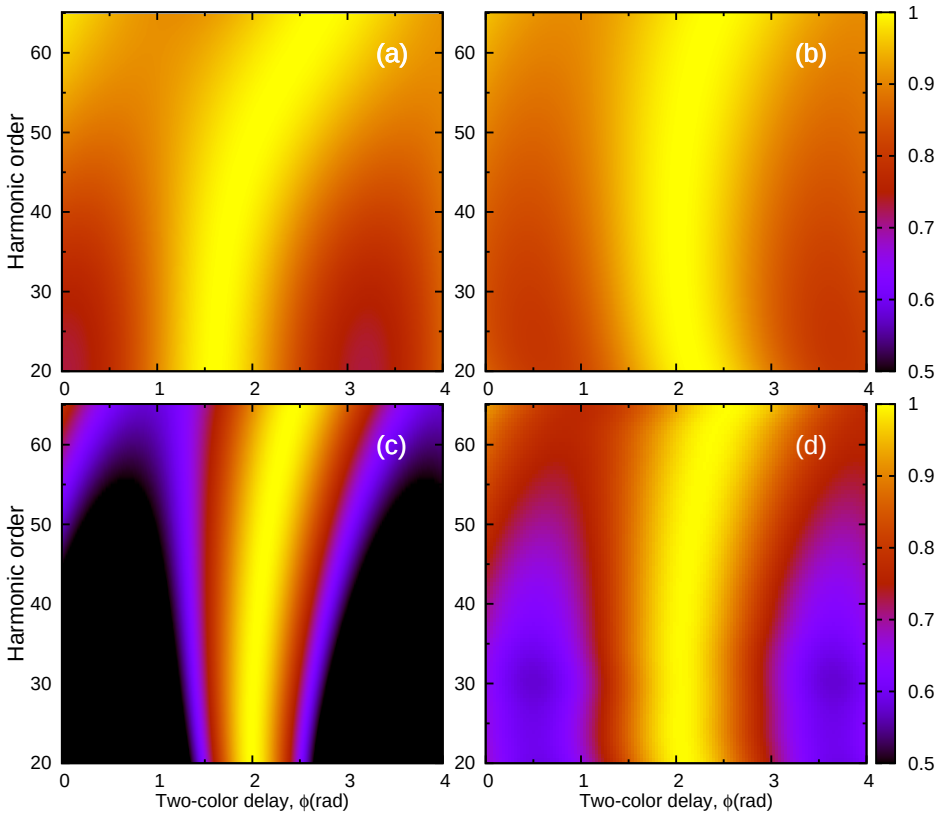

Figure 3.4: Comparison of the normalized harmonic intensity for two-color HHG as a function of harmonic order and two-color delay ϕ. (a) the prediction of the classical model; (b) the prediction of the quantum-orbit model with real times; (c) the prediction of the quantum-orbit model with complex times; (d) results from TDSE simulation. The laser intensity is 4×10^{14} W/cm^2 and ε=0.1. The classical cutoff is at harmonic order 65.

along the y-axis Eq. (3.16), we show the harmonic intensity as a function of harmonic order and two-color delay ϕ in Figs. 3.4 (a) and (b), by inserting the ionization and return times from the classical three-step model and the quantum-orbit model. Note that the results from the two models are not the harmonic signals, since Eq. (3.19) only contains the exponential dependence of the harmonic signal on the initial lateral velocity $v_{y0}(t_i, t_r, \phi)$. For each harmonic order, the harmonic intensity as a function of the two-color delay is normalized by the maximum value. The normalized harmonic intensity for two-color HHG from the TDSE is shown in Fig. 3.4 (d). The results are in good agreement with the experiment. Moreover, we propose a fully quantum mechanical model to describe the electron dynamics along the y-axis, with the idea of using the complex times of the quantum-orbit model in Eq. (3.19). Then

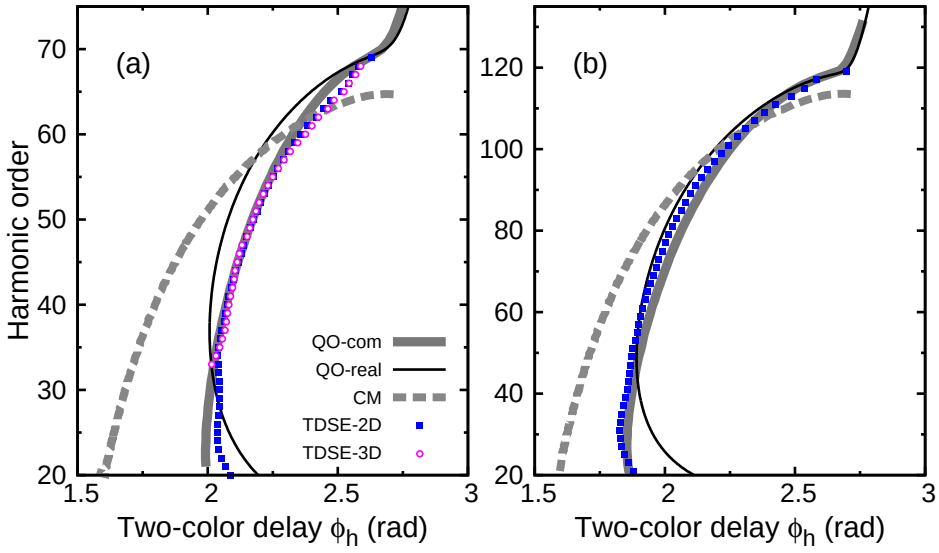

Figure 3.5: Two-color delays maximizing the harmonic intensity. Thick solid lines (grey) are the predictions of the quantum-orbit model with complex times (QO-com). Thin solid lines (black) are the results with real times (QO-real). Thick dashed lines (grey) are the predictions of the classical three-step model (CM); Purple circles and blue squares, results from the 3D and 2D TDSE, respectively. (a) Laser intensity $4{\times}10^{14}\,\mathrm{W/cm^2}$; (b) $8{\times}10^{14}\,\mathrm{W/cm^2}$.

the velocity along y becomes complex. We use the real part of the resulting the complex initial velocity in Eq. (3.19). The results from this model are shown in Fig. 3.4 (c). Modulations of the harmonic intensities can be seen in Fig. 3.4 as the two-color delay varies. The details of the modulation depend on the harmonic order. The explanation is that different harmonic orders originate from electron trajectories with different excursion times. The prediction of the quantum-orbit model with complex times agrees much better with the TDSE result, as compared to the real-time models.

We extract for every harmonic frequency the two-color delay ϕ_h that maximizes the harmonic signal in Fig. 3.4. From Eq. (3.19) we find that this is fulfilled for $v_{y0}(t_i, t_r, \phi) = 0$. Eq. (3.16) then yields the optimized two-color delay $\phi_h(\Omega)$

$$\phi_h(\Omega) = \arctan\left[\frac{\cos 2\omega t_i - \cos 2\omega t_r - 2\omega(t_r - t_i)\sin 2\omega t_i}{\sin 2\omega t_i - \sin 2\omega t_r + 2\omega(t_r - t_i)\cos 2\omega t_i}\right]. \tag{3.20}$$

For comparison, we insert the real ionization and return times from the classical three-step model or the quantum-orbit model into Eq. (3.20) to find $\phi_h(\Omega)$.

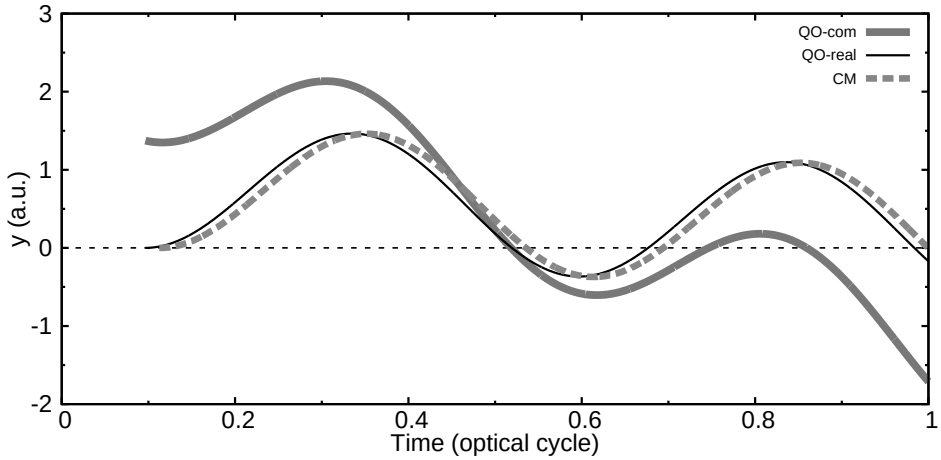

Figure 3.6: Electron displacement along the y-axis for harmonic order 40. The thick solid curve represents the real part of electron displacement from the quantum-orbit model with complex times; the thin solid curve is the result from the quantum-orbit model with real times; the thick dashed curve is the result from the classical three-step model. The laser intensity is $4\times10^{14}\,\mathrm{W/cm^2}$.

With the complex ionization time τ_i and return time τ_r, we choose $\phi_h(\Omega)$ that corresponds to purely imaginary initial lateral velocity, i.e. $\mathrm{Re}(v_{y0}(\tau_i,\tau_r,\phi_h)) = 0$, where $v_{y0}(\tau_i,\tau_r,\phi_h)$ is the complex initial velocity obtained from Eq. (3.16) with complex times. In Fig. 3.5, we show the results for two different laser intensities, including 3D TDSE results for the lower intensity. The comparison clearly shows that the results are practically independent of the dimensions of the simulation. For the lower intensity, neither of the two trajectory models matches the TDSE results when the real times are used. If we use the complex times from the quantum-orbit model, however, we find a very good match with the TDSE. For the higher intensity, the deficiencies of the real-time trajectories are less pronounced but still visible.

To gain further insight into the differences between the classical and quantum mechanical description of the electron motion in the y direction, we compare the instantaneous electron displacement along y-axis after it is released by the main field. Fig. 3.6 shows the electron displacements obtained from Eq. (3.15) with times from different models. The two-color delays ϕ_h maximizing the harmonic intensities are used. For complex times from the quantum-orbit model, we plot the real part $\mathrm{Re}(y(t))$ of the electron displacement, assuming that the electron start tunneling at zero point with the complex ionization time, i.e. $y(\tau_i) = 0$. In the classical description of electron lateral motion, the

electron starts its motion from the parent ion and returns to it at the recombination time. In contrast, with the complex times from the quantum-orbit model, the electron is born at some distance from the parent ion. The good agreement between the TDSE results and the predictions of the quantum-orbit model with complex times in Fig. 3.6 indicates that tunnel ionization induces electron displacement in both x and y direction.

3.2.4 Amplitude ratio

The second observable of interest is the amplitude ratio of the y- and x-component of the generated field as

$$R(\Omega) = \sqrt{I_{Gy}(\Omega, t_r)/I_{Gx}(\Omega, t_r)}. \tag{3.21}$$

Here I_{Gx} and I_{Gy} are the intensities of the x-component and y-component, obtained from the separate Gabor transforms of the two dipole-acceleration components according to Eqs. (3.11) and (3.12). The amplitude ratio R is precisely the quantity measured in the experiment where the square root of the ratio of neighboring even and odd harmonics was taken. For linearly polarized harmonics, the polarization angle θ relative to the x axis is given by $\tan\theta = R$. Note that our method works even when the harmonics are not linearly polarized.

The appearance of even harmonics polarized along the y-axis is induced by the lateral velocity of the free electron at the moment of return. Within the SFA, the x- and y-component of the recombination matrix element are expressed as

$$d_x(\mathbf{p} + \mathbf{A}(t_r)) = -\langle \psi_{\mathrm{PW}}(\mathbf{p} + \mathbf{A}(t_r))|x|\Psi_0\rangle, \tag{3.22}$$

$$d_y(\mathbf{p} + \mathbf{A}(t_r)) = -\langle \psi_{\mathrm{PW}}(\mathbf{p} + \mathbf{A}(t_r))|y|\Psi_0\rangle. \tag{3.23}$$

By rotating the original coordinate system (x, y) to a new coordinate systme (x', y'), with the x' axis along the electron recollision angle α. The transform has the form

$$\begin{aligned} x' &= x\cos\alpha + y\sin\alpha \\ y' &= x\sin\alpha - y\cos\alpha. \end{aligned} \tag{3.24}$$

If the bound-state wave function $|\Psi_0\rangle$ has spherical symmetry, the recombiantion matrix element along y' axis is zero, and the x- and y-component of

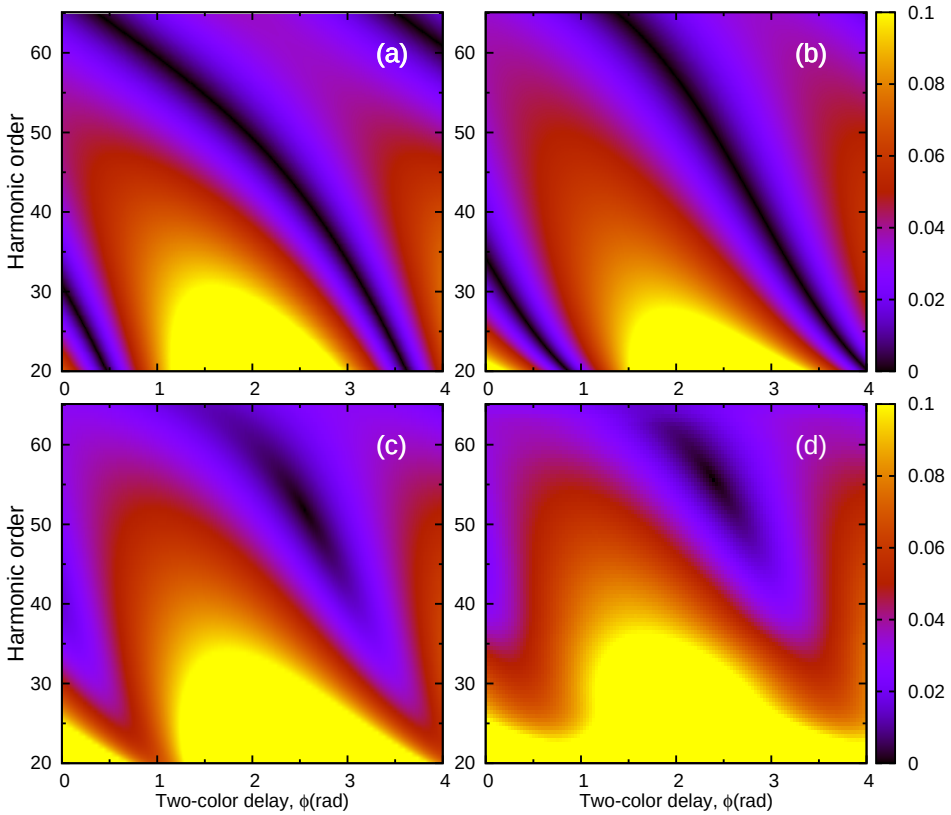

Figure 3.7: Comparison of the y to x amplitude ratio for two-color HHG as a function of harmonic order and two-color delay ϕ. (a) The prediction of the classical model; (b) the prediction of the quantum-orbit model using only the real parts of the complex times; (c) the prediction of the quantum-orbit model with complex times; (d) results from the TDSE simulation. The laser intensity is the same as in Fig. (3.4).

the recombination matrix element becomes

$$d_x(\mathbf{p}+\mathbf{A}(t_r)) \;=\; \langle\psi_{\mathrm{PW}}(\mathbf{p}+\mathbf{A}(t_r))|x'\cos\alpha|\Psi_0\rangle, \tag{3.25}$$

$$d_y(\mathbf{p}+\mathbf{A}(t_r)) \;=\; \langle\psi_{\mathrm{PW}}(\mathbf{p}+\mathbf{A}(t_r))|x'\sin\alpha|\Psi_0\rangle. \tag{3.26}$$

The electron recollision angle can be extracted directly from the ratio of the y and x component of the recombination matrix element

$$\tan\alpha \;=\; \frac{d_y(\mathbf{p}+\mathbf{A}(t_r))}{d_x(\mathbf{p}+\mathbf{A}(t_r))} \;=\; \frac{v_y(t_r)}{v_x(t_r)}. \tag{3.27}$$

Since the harmonic intensity is proportional to the modulus squared of the

recombination matrix element, Eq. (3.27) implies that the amplitude ratio R is fully determined by the return velocity vector, namely $R = |v_y(t_r)/v_x(t_r)|$. In the case of linear polarization, this would mean that the recollision angle is identical to the harmonic polarization angle. Using $\Omega - I_p = v_x^2(t_r)/2$ and Eq. (3.17), we have

$$R = \frac{\varepsilon E_0/(2\omega)}{\sqrt{2(\Omega - I_p)}} \left| \sin\varphi_r + \frac{\cos\varphi_r - \cos\varphi_i}{2\omega(t_r - t_i)} \right|. \tag{3.28}$$

The amplitude ratio as a function of harmonic order and two-color delay is shown in Fig. (3.7). Similar to the harmonic intensity, the amplitude ratio is modulated as a function of the two-color delay and behaves differently for each harmonic order. The maximum value of the amplitude ratio decreases as a function of harmonic frequency, i.e. the signal polarized along the y-axis becomes smaller for high harmonic orders, which means that the electron returns with a smaller angle α. The prediction of the quantum-orbit model with complex times agrees well with the TDSE result, compared to the predictions with real times.

In Fig. 3.8 (a) and (b), we show a comparison for selected harmonic orders. We compare the amplitude ratio R obtained from the TDSE and from Eq. (3.28) with the complex times from the quantum-orbit model. The good agreement is in accordance with the previous observation [112] that the recollision angle in elliptically polarized fields is not strongly modified by Coulomb focusing. Interestingly the signal polarized along the y axis does not become zero although classically the recollision angle must pass through zero for an appropriate choice of two-color delay. This indicates that a single recollision in the two-color field generates elliptically polarized harmonics, i.e. the y- and x-components of the harmonic field oscillate out of phase. The phase difference between the y- and x-component versus two-color delay is shown in Fig. 3.8 (c) and (d). In the TDSE simulation, the harmonic phase is obtained from the complex-valued Gabor transform in Eqs. (3.11) and (3.12), before taking the modulus square. In the quantum-orbit model, the phase difference is evaluated as $\arg(v_y/v_x)$ with the complex velocities. The phase difference from the TDSE simulation is in good agreement with the prediction of the quantum-orbit model with complex times. The complex treatment of the lateral motion can explain the elliptically polarized harmonic field observed in our TDSE simulation. It also predicts the possibility to control the polarization properties of the generated harmonics.

We now analyze the two-color delay $\phi_a(\Omega)$ that maximizes the amplitude

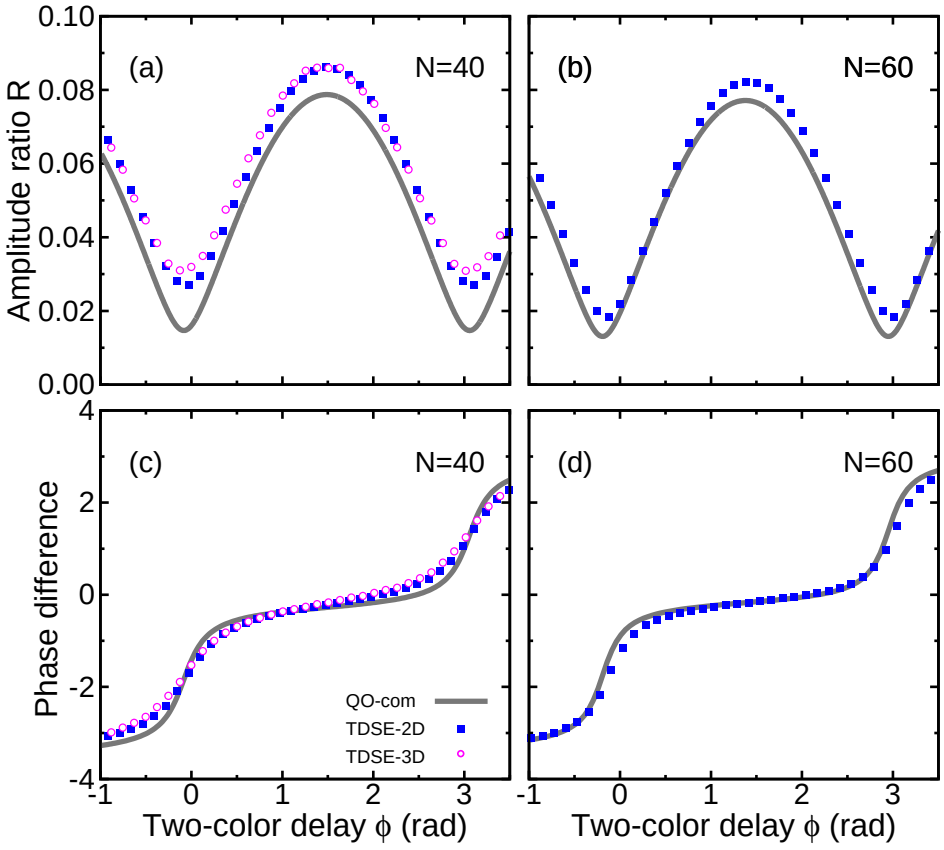

Figure 3.8: (a),(b) Amplitude ratio R as a function of two-color delay; (c),(d) Phase difference between y- and x-component of the harmonics versus two-color delay. Left panels: Laser intensity 4×10^{14} W/cm^2; Right panels: 8×10^{14} W/cm^2. N denotes the harmonic order.

ratio for a given harmonic frequency. From Eq. (3.28), we get the expression for the optimized two-color delay $\phi_a(\Omega)$

$$\phi_a(\Omega) = \arctan\left|\frac{\sin 2\omega t_i - \sin 2\omega t_r + 2\omega(t_r - t_i)\cos 2\omega t_r}{\cos 2\omega t_r - \cos 2\omega t_i + 2\omega(t_r - t_i)\sin 2\omega t_r}\right|. \tag{3.29}$$

By inserting the ionization and return times from the classical three-step model or the quantum-orbit model into Eq. (3.29), one finds $\phi_a(\Omega)$ that maximizes R. Fig. 3.9 shows the results for two different laser intensities. The best agreement with the TDSE results is achieved by using the complex times from the quantum-orbit model. Significant differences between the other two results with real times and the TDSE results are shown, due to the lack of the imaginary parts of the electron velocity.

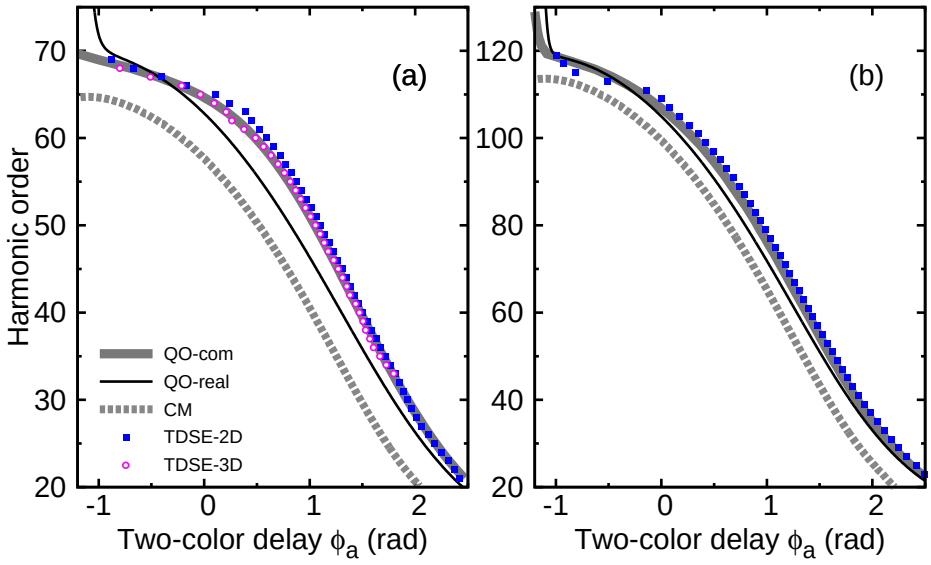

Figure 3.9: Two-color delays $\phi_a(\Omega)$ maximizing the amplitude ratio R. (a) Laser intensity 4×10^{14} W/cm^2; (b) 8×10^{14} W/cm^2.

3.3 Retrieval of ionization and return time from two-color HHG

In [48], the electron exit times are measured from the variations of harmonic intensity and amplitude ratio with two-color delay, based on the classical analysis of the electronic lateral motion after tunneling. However, we have shown that the classical analysis of the dynamics along the y axis may not be sufficient for an accurate retrieval. Both $\phi_h(\Omega)$ and $\phi_a(\Omega)$ are much better reproduced by the quantum-orbit model with complex times. A quantum mechanical version is necessary to retrieve the ionization and return times, based on electron trajectories evolving in complex times. In this section, we present both the classical and quantum mechanical retrieval methods and show the comparison of the retrieved times.

3.3.1 Classical retrieval

To allow a recollision in the classical picture with two-color delay ϕ_h and to maximize the amplitude ratio, two conditions have to be satisfied:

$$v_{y0}(t_i, t_r, \phi_h) = 0, \quad \left.\frac{\partial R(t_i, t_r, \phi)}{\partial \phi}\right|_{\phi_a} = 0. \tag{3.30}$$

Inserting Eqs. (3.16) and (3.28) into Eq. (3.30), one obtains

$$\begin{aligned} 2\omega(t_r - t_i)\sin(2\omega t_i + \phi_h) &= \cos(2\omega t_i + \phi_h) - \cos(2\omega t_r + \phi_h), \\ 2\omega(t_r - t_i)\cos(2\omega t_r + \phi_a) &= \sin(2\omega t_r + \phi_a) - \sin(2\omega t_i + \phi_a). \end{aligned} \tag{3.31}$$

Using the extracted two-color delays $\phi_h(\Omega)$ and $\phi_a(\Omega)$ from TDSE results, we can find the ionization time t_i and return time t_r numerically. The corresponding times are labeled as "TDSE-2D-real" in Fig. 3.10.

3.3.2 Quantum mechanical retrieval

The key point of the quantum mechanical retrieval method is to use the complex times of the quantum-orbit model. The velocity along y is complex and the two equations determining the two-color delays ϕ_h and ϕ_a read

$$\mathrm{Re}\,(v_{y0}(\tau_i, \tau_r, \phi_h)) = 0, \quad \partial R(\tau_i, \tau_r, \phi)/\partial\phi = 0. \tag{3.32}$$

Here the real times t_i and t_r in Eqs. (3.16) and (3.28) are replaced by the complex times τ_i and τ_r from the quantum-orbit model.

A problem arises in the retrieval of both complex times τ_i and τ_r from the measured two-color delays ϕ_h and ϕ_a using Eqs. (3.32): if the times are complex, there are four unknown variables but only two equations. It is a good approximation [94] to neglect the imaginary part of τ_r and to assume that the imaginary part of τ_i equals the instantaneous Keldysh tunneling time,

$$\mathrm{Im}\,\tau_i = \sqrt{2I_p}/|E_x(t_i)|. \tag{3.33}$$

The assumptions have been verified in Fig. 2.8. For each harmonic frequency we use a numerical procedure to find the solution of Eqs. (3.32), i.e. the ionization and return times.

3.3.3 Retrieved ionization and return times

The retrieved ionization and return times are shown in Fig. 3.10 (a). The retrieved real parts of the ionization and return times match very well with the quantum-orbit model. The slight difference in the return times is partially explained by neglecting the imaginary part of the return time in the retrieval. The retrieval based on the classical equations (using real times) yields return times up to more than 50 as too early; the ionization times are too early for the higher harmonics and too late for the low harmonics. Fig. 3.10 (c),(d) show the deviations of the retrieved ionization and return times from the quantum-orbit

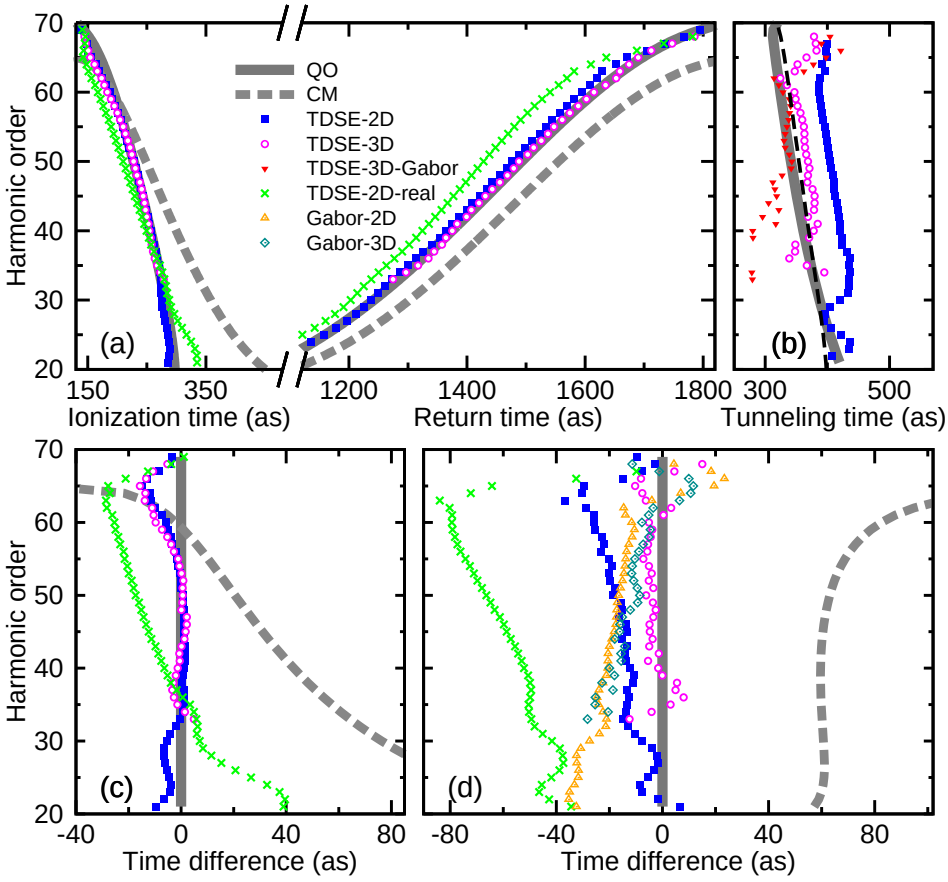

Figure 3.10: (Color online) (a) Reconstructed ionization times and return times. (b) Reconstructed tunneling times. Time zero in (a) is at the maximum of the electric field. Purple circles (TDSE-3D) and blue squares (TDSE-2D) represent the times from the complex-time retrieval. Green crosses represent the times from the classical retrieval with real times (TDSE-2D-real). Thick grey solid lines show the real parts of the quantum-orbit model times (QO); thick grey dashed lines are from the classical model (CM). The thin black dashed line in (b) is the Keldysh time $\sqrt{2I_p}/|E_x(t_i)|$. Red triangles in (b) are the reconstructed tunneling times with the Gabor emission times. Bottom: ionization times (c) and return times (d) relative to the quantum-orbit model. Orange triangles and cyan diamonds in (d) are the Gabor emission times (2D and 3D, respectively). The laser intensity is $4{\times}10^{14}\,\mathrm{W/cm^2}$.

model. From harmonic order 40 to 55, where a clean retrieval is possible since the short-trajectory branch is perfectly isolated from other trajectories, we find remarkably small deviations below 5 as. The error of the classical retrieval of the return time did not become apparent in the experiment [48] because the absolute scale of the two-color delay was fixed by requiring agreement with

the quantum-orbit model. If we applied the same procedure to our TDSE results, the classically retrieved ionization times would also shift to later times along with the return times, resulting in a significant improvement for the high harmonic orders.

In an alternative scheme, we use the same observables to retrieve the real and imaginary part of the ionization time, by making suitable assumptions about the return time. We neglect the imaginary part of the return time, and we take the real part either from the quantum-orbit model or from the Gabor distribution in the TDSE simulation. Note that this approach is very suitable for experiment: for example, the return times could be taken from measurements as in [82]. The retrieved imaginary part is shown in Fig. 3.10(b). Although the retrieval is very sensitive to small errors in the input parameters, we find good agreement with the quantum-orbit model and the Keldysh time. To our knowledge, this is the only reported scheme for determination of the tunneling time.

3.4 Conclusion

We have obtained the ionization and return times in high-order harmonic generation from the numerical solution of the TDSE. We use a retrieval based on complex-time trajectories and we find astonishing agreement with the quantum orbit model. The classical retrieval gives only approximate results as it ignores the change of the lateral position and velocity during tunneling. We have also retrieved the tunneling time by making reasonable assumptions for the return time. This shows the physical relevance of the tunneling time: it affects the lateral dynamics in the two-color field. Such a position-space effect is in contrast to the view that the tunneling time determines merely the ionization rate. A signature may also be expected in the vibrational wave packet in the probing of attosecond dynamics by chirp encoded recollision [113].

Chapter 4

Positioning of bound electron wave packets in molecules

4.1 Introduction

High-harmonic spectroscopy provides a unique insight into the initial shape and location of the hole left by field-induced one-electron ionization [30, 39, 114, 115]. A theoretical study shows that electron-electron correlation effect plays an important role during tunneling ionization [114]. In this work, we investigate the correlated electron dynamics in field-induced ionization from molecules by numerical solution of the TDSE. We take the simplest neutral molecule, i.e. the H_2 molecule as an example. In the case of H_2, two ionization channels contribute to HHG: the intermediate H_2^+ ion is either in the ground or first excited state. The internuclear distance is chosen larger than the equilibrium distance such that the energy gap between the two ionic states is comparable with the laser frequency, giving access to the rearrangements occuring in the ion within less than one optical period of the driving laser pulse. The populations and phases of the two states determine the shape and location of the total bound wave function. By analyzing the two-electron wave function for one-electron ionization, we find that strong-field ionization in combination with electron correlation can prepare localized or delocalized bound electron wave packets, depending on the laser intensity. From the numerical two-electron wave packet, we calculate the ionization phase, i.e. the phase difference between the gerade and ungerade states of H_2^+, for different internuclear distances. We investigate the HHG spectra at various internuclear distances, showing that ionization to the ionic ground state is not sufficient to explain HHG at increased distance. Finally, we propose a simple two-channel recollision model, including both the two-center structural interference and the two-channel dynamical interference effects. Using the recollision model with

the numerical ionization phase, the extrema in the harmonic spectra are well reproduced.

4.2 Strong-field ionization from H_2 molecule

The field-free Hamiltonian of H_2 molecule in the center-of-mass frame can be written as

$$H = \frac{\mathbf{P}_{\mathbf{R}}^2}{2M_\mu} + \sum_{i=1,2} \frac{\mathbf{P}_{\mathbf{r}_i}^2}{2} + V(\mathbf{R}, \mathbf{r_1}, \mathbf{r_2}), \tag{4.1}$$

where M_μ is the reduced mass of the nuclei. $\mathbf{R}$ denotes the internuclear coordinate and $\mathbf{r}_1$, $\mathbf{r}_2$ are the position vectors of the electrons with respect to the center of mass. The Coulomb interactions between all pairs of particles are

$$\begin{aligned} V(\mathbf{R}, \mathbf{r_1}, \mathbf{r_2}) &= -\sum_{i=1,2} \frac{1}{\sqrt{(\mathbf{r}_i + \frac{\mathbf{R}}{2})^2}} - \sum_{i=1,2} \frac{1}{\sqrt{(\mathbf{r}_i - \frac{\mathbf{R}}{2})^2}} \\ &+ \frac{1}{\sqrt{(\mathbf{r}_1 - \mathbf{r}_2)^2}} + \frac{1}{\mathbf{R}}. \end{aligned} \tag{4.2}$$

Due to the high ratio between nuclear and electronic masses, the electron moves much faster than the nucleus that we can consider the nucleus to be static with respect to electron motion.

4.2.1 One-dimensional model

In this work, we consider a one-dimensional (1D) model H_2 molecule with fixed nuclei. Although the 1D model lacks the information about angular dependencies, it is possible to qualitatively reproduce important features of the real molecule, such as the electron-electron correlation effect. The electronic time-independent Schrödinger equation for the 1D model H_2 molecule reads

$$\left[-\frac{\partial_1}{2} - \frac{\partial_2}{2} + V(x_1, x_2) \right] \Psi(x_1, x_2) = E\Psi(x_1, x_2) \tag{4.3}$$

with the soft-core potential

$$\begin{aligned} V(x_1, x_2) &= -\sum_{i=1,2} \frac{1}{\sqrt{(x_i + \frac{R}{2})^2 + \sigma^2}} - \sum_{i=1,2} \frac{1}{\sqrt{(x_i - \frac{R}{2})^2 + \sigma^2}} \\ &+ \frac{1}{\sqrt{(x_1 - x_2)^2 + \sigma^2}}, \end{aligned} \tag{4.4}$$

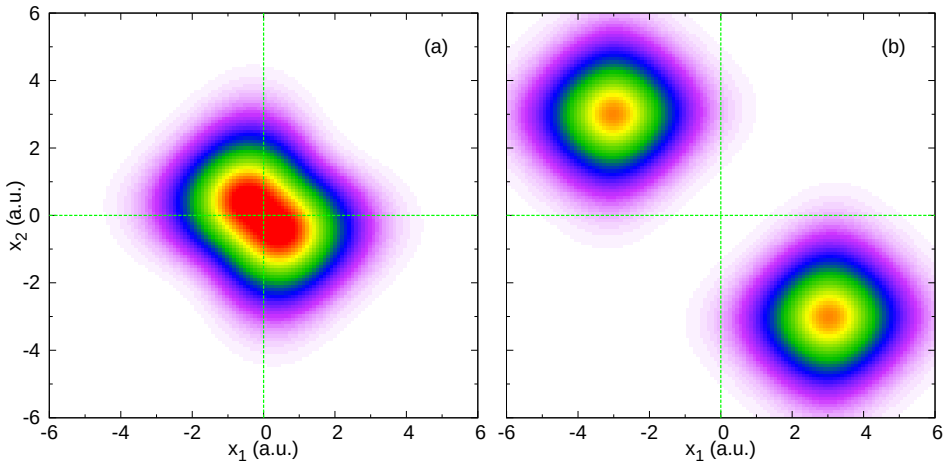

Figure 4.1: (Color online) Electron distribution in the electronic ground state of the 1D hydrogen molecule with fixed internuclear distance (a) $R = 1.4$ a.u. and (b) $R = 6$ a.u. x_1 and x_2 are the coordinates of the two electrons.

where x_1, x_2 and R are the two electron coordinates and nuclear separation. We use the soft-core parameter $\sigma^2 = 1$ to eliminate the singularity at $x_{1,2} = \pm R/2$ and $x_1 = x_2$ in the numerical simulation. The soft-core potential is physically resonable because of the fact that in real H_2 molecule, the two electrons have enough space available to bypass each other and the nucleus.

The Hamiltonian is symmetric under exchange of the spatial coordinates of the two electrons. This property allows for wavefunctions that are either symmetric or antisymmetric with respect to exchange. In this work, we restrict our discussion to the singlet state, i.e. the two electrons have opposite spins, and the wave function is invariant under exchange of the coordinates of the two electrons.

4.2.2 Ionization-induced bound wave packet

First, we investigate the two-electron distribution in the electronic ground state for different nuclear separations. The two-electron singlet ground state can be found through imaginary-time evolution starting from a space-symmetric initial wave function using the field-free Hamiltonian. The results are shown in Fig. 4.1. It can be seen that for H_2 molecule with small nuclear separation ($R = 1.4$ a.u.), two electrons are both localized around the center. In contrast, for the stretched internuclear separation ($R = 6$ a.u.), the two electrons are located on opposite sides of the molecule, which yields two isolated neutral hydrogen atoms in the ground state in the separated-atom limit.

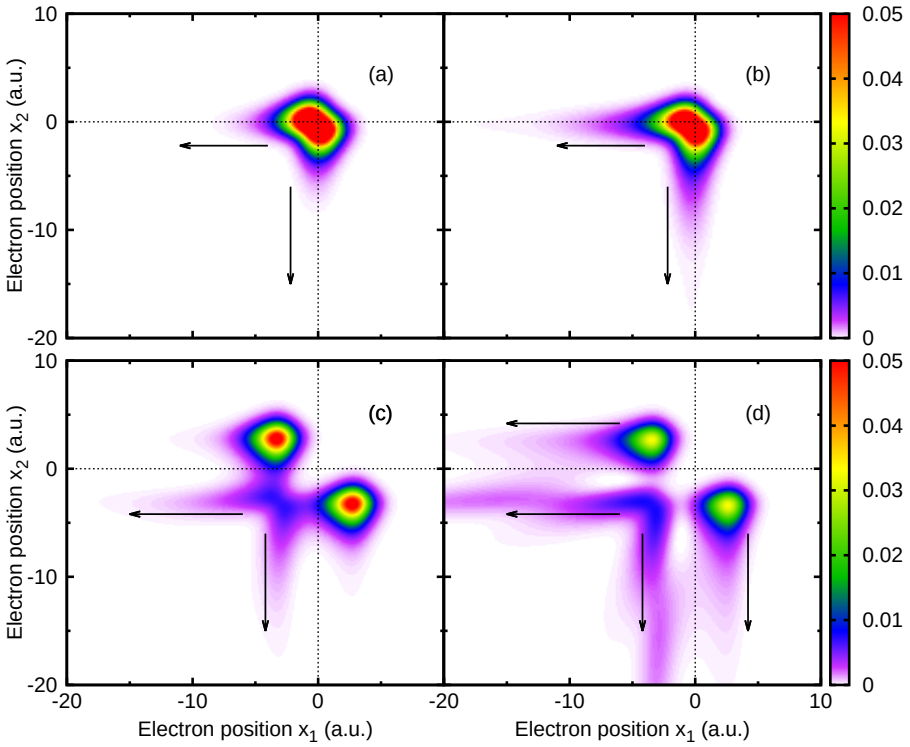

Figure 4.2: (Color online) Two-electron density at the peak of a half-cycle pulse for $R = 1.4$ a.u. (a), (b) and $R = 6$ a.u. (c), (d). Arrows represent the directions of the outgoing electron. (a) (c) Laser intensity $2{\times}10^{14}$ W/cm^2. (b) (d) Laser intensity $4{\times}10^{14}$ W/cm^2.

Next, we investigate the strong-field ionization process through TDSE simulation. The TDSE for the two-electron wave function $\Psi(x_1, x_2, t)$ describing 1D H_2 in a laser field $E(t)$ reads

$$i\,\partial_t\Psi(x_1,x_2,t) = \left[-\frac{\partial_1^2}{2} - \frac{\partial_2^2}{2} + V(x_1,x_2) + (x_1{+}x_2)E(t)\right]\Psi(x_1,x_2,t). \quad (4.5)$$

We use a half-cycle pulse with 1200 nm wavelength. The time evolution starts from the singlet ground state. The split-operator method [102] is applied to solve the TDSE with 2048 time steps per optical cycle, yielding the time-dependent two-electron wave function $\Psi(x_1, x_2, t)$. The two-electron densities $|\Psi(x_1, x_2, t)|^2$ at the peak of the half-cycle pulse (with positive electric field) are shown in Fig. 4.2 for $R = 1.4$ a.u. and $R = 6$ a.u. using two different laser intensities. In both cases, the major part of the density resides in a ground-state-like wave packet as in Fig. 4.1. Additionally, there is density escaping towards negative values of x_1 or x_2, representing single ionization. The behav-

ior of the remaining electron depends on the internuclear distance R. With small $R=1.4$ a.u., the outgoing electron coordinate is negative and the remaining bound electron is localized around zero, resembling the ionic ground state in Fig. 4.3(a). For large $R=6$ a.u. with lower laser intensity, we see that both electron coordinates are negative in the ionizing part, i.e. ionization localizes the remaining bound electron at the site that is on the same side as the outgoing electron. The remaining electron resembles a coherent superposition state of the ionic states. This is consistent with the mechanism of enhanced ionization via the ion-pair state [116–118]. The relevance of the ion-pair state in the H_2 dynamics with moving nuclei has also been demonstrated previously [119]. For the higher intensity, the coordinate of the bound electron can be positive or negative, indicating delocalization of the remaining electron. In short, for the H_2 molecule at small internuclear distance, laser-induced ionization leaves the ion in the ground state, whereas with stretched internuclear distance, the ionization-induced bound electron wave packet is left in a coherent superposition of ionic states with the relative phase depending on the laser intensity. The phase between different ionic states is termed as the ionization phase.

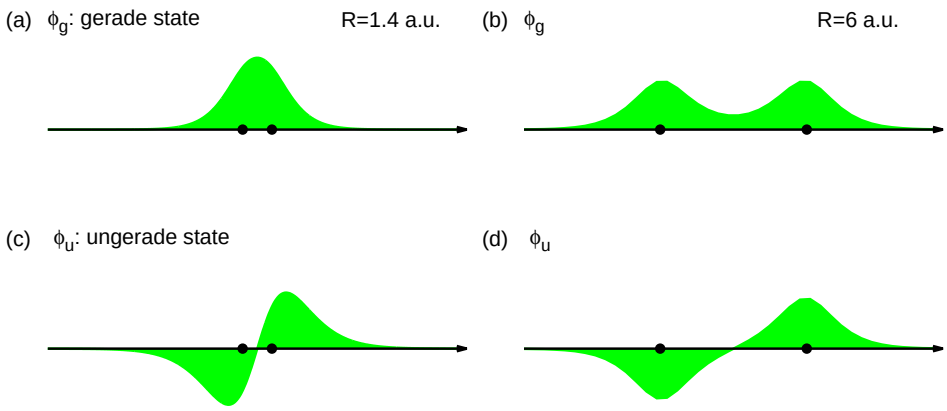

Figure 4.3: Eigen states for H_2^+ molecule with fixed nuclear separation $R = 1.4$ a.u. (left) and $R = 6$ a.u. (right). The top panels represent the wave function of the ground state; the bottom panels show the wave function of the first excited electronic state. The points represent the position of the two protons.

4.2.3 Ionization phase

In order to obtain a more quantitative description of the ionization-induced bound electron wave packet for stretched internuclear distance, we calculate the wave function of the bound electron at the ionization time t_i. First, the bound wave packet $\varphi(x_1, k, t)$ at time t, one optical cycle after the half-cycle pulse, for outgoing electron momentum k is obtained as the overlap between the two-electron wave function and the outgoing electron approximated as a plane wave, i.e.,

$$\varphi(x_1, k, t) = \int e^{-ikx_2}\, w(x_2)\Psi(x_1, x_2, t)\, dx_2. \tag{4.6}$$

We use a window function

$$w(x) = \frac{1}{1 + e^{5(x+10)}} + \frac{1}{1 + e^{5(-x+10)}} \tag{4.7}$$

to eliminate the inner part of the wave function, where the ground state is located. We relate the momentum of the outgoing electron to the ionization time t_i by the classical expression $k = -\int_{t_i}^{t} E(t')dt'$. The bound wave packet is propagated backwards in time using the one-electron TDSE with the same half-cycle pulse as in the two-electron TDSE, yielding the initial bound wave packet $\chi(x_1, t_i)$ at the ionization time t_i. Because the tunnel ionization rate is exponentially sensitive to the ionization energy, we only consider the two most important channels, namely the H_2^+ ion in the gerade ground state φ_g or ungerade first excited state φ_u (Fig. 4.3). For every ionization time, we calculate the populations $|C_{g,u}|^2$ of the two states and their relative phase $\phi = \arg(C_u/C_g)$ from the complex amplitudes $C_{g,u} = \langle\varphi_{g,u}|\chi(t_i)\rangle$. Our convention for the ionization phase ϕ is that $\phi = 0$ refers to the bound electron located opposite to the outgoing electron, as in Fig. 4.4 (b). This is in accordance with the definition in the work by Smirnova and coworkers [30, 39], where the ionization phase refers to the phase difference of the ionizing wings of different Dyson orbitals.

The two states are found to be almost equally populated for the internuclear distances $R = 5.2$ a.u. and $R = 6$ a.u. The existence of a bound superposition state requires non-orthogonality of the continuum wave functions in the two ionization channels [40]. In our case, we use the same momentum k for both channels in Eq. (4.6), so the numerically obtained equal occupation of the gerade and ungerade bound states proves the existence of a bound superposition state. Fig. 4.5 shows that the ionization phase depends on the laser intensity,

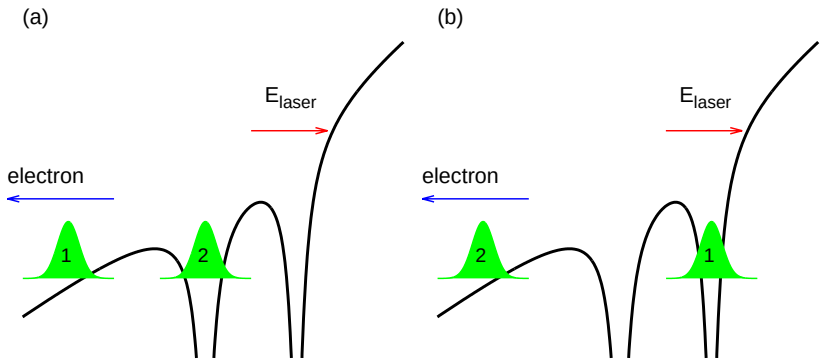

Figure 4.4: Schematic representation of ionization-induced bound electron wave packets. (a) the bound electron is on the same side with the outgoing electron, corresponding to the ionization phase $\phi = \pi$; (b) the bound electron is on the opposite side from the outgoing electron, corresponding to the ionization phase $\phi = 0$;

especially when the internuclear distance is large. This indicates that the location of the ionization-induced hole depends on the laser intensity as well. The ionization phase depends weakly on the ionization time. For the lower intensity 2×10^{14} W/cm^2, the phase stays close to π, i.e. the bound electron starts on the same side as the outgoing electron (Fig. 4.4(a)). For the higher intensity 4×10^{14} W/cm^2 and $R = 6$ a.u., the phase is near $3\pi/2$. Phases far from 0 and π imply a delocalized wave packet in the process of moving from one nucleus to the other. Varying the laser intensity allows us to vary the phase, therefore opening a possibility for controlling the electron localization. As shown in Ref. ([39]), the ionization phase is encoded in the HHG spectrum. In the next section, we will show how the wave-packet creation is revealed by the emission spectrum in high-order harmonic generation, which is sensitive to the ionization and recombination phase difference between different ionization channels.

4.3 HHG from H_2 molecule

As has been investigated in [18, 19], the harmonic spectrum from H_2 molecules exhibits a clear minimum due to destructive two-center interference, known as the structural interference. It depends only on the geometry of the bound state. We have shown in the above section that for H_2 molecule with stretched internuclear separation, laser-induced ionization leaves the bound

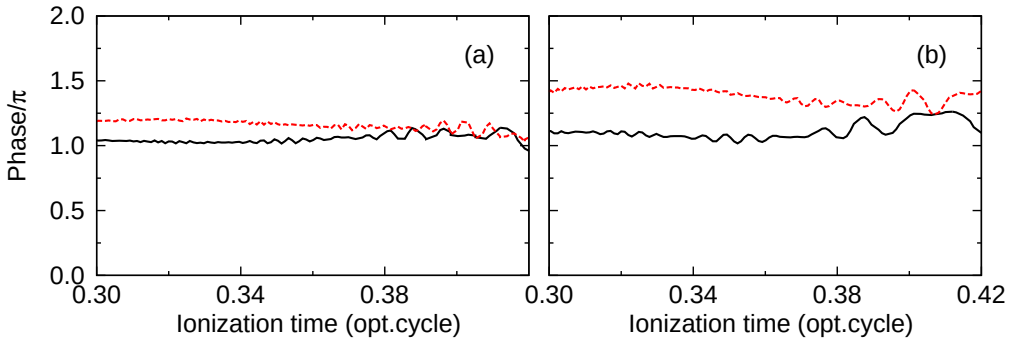

Figure 4.5: (Color online) Relative phase between the ungerade and gerade states versus ionization time. Solid lines: intensity 2×10^{14} W/cm^2. Dashed lines: intensity 4×10^{14} W/cm^2. Left panel: $R = 5.2$ a.u. Right panel: $R = 6$ a.u.

electron in a superposition of the ionic ground state and first excited state, which could affect the harmonic spectrum by the interference between contributions from these two channels as in [30].

4.3.1 Two-center interference in HHG

First, we take the H_2^+ molecule as an example to introduce the structural interference in HHG. The harmonic spectrum from H_2^+ is minimized at some critical angle between the molecular axis and the polarization of the laser pulses, because of the destructive interference when the electron recombines with the two-center ion. Using the linear combination of atomic orbitals (LCAO) and the plane wave approximation, the recombination dipole velocity is described as

$$\begin{aligned} v_d(\mathbf{k}) &= i\int d^3r\, e^{i\mathbf{k}\cdot\mathbf{r}}\,\nabla\varphi_g(\mathbf{r}) \\ &= 2i\cos\left(\frac{\mathbf{k}\cdot\mathbf{R}}{2}\right)\int d^3r\, e^{i\mathbf{k}\cdot\mathbf{r}}\,\nabla\varphi_{at}(\mathbf{r}), \end{aligned} \tag{4.8}$$

where $\varphi_g(\mathbf{r}) = \frac{1}{\sqrt{1+s}}\left[\varphi_{at}(\mathbf{r}+\frac{\mathbf{R}}{2}) + \varphi_{at}(\mathbf{r}-\frac{\mathbf{R}}{2})\right]$, where φ_{at} is the ground state of hydrogen atom and s is the overlap integral between two atomic orbitals. Simple formulae can be derived to predict the two-center interference in HHG. Destructive interference for H_2^+ occurs when

$$\mathbf{k}\cdot\mathbf{R} = (2m+1)\pi, \qquad m = 0, 1, \ldots \tag{4.9}$$

Constructive interference occurs when

$$\mathbf{k} \cdot \mathbf{R} = 2m\pi, \qquad m = 0, 1, \ldots \tag{4.10}$$

Within the plane wave approximation, the influence of the Coulomb binding potential on the returning electron is neglected. It has been shown that with the energy relation $E_k = \Omega$, this simple model gives good predictions for low order harmonics, while the energy relation $E_k = \Omega - I_p$ works much better for high order harmonics [100].

Next, we use a more precise approach to predict the structural interference effect in HHG. We consider a laser-field-free setup, in which harmonics are generated by collision of a Gaussian electron wave packet that is initially prepared heading towards the molecular ion in the ground state. The continuous emission spectrum from the collision shows the effect of molecular structure on HHG in the absence of multichannel effects or distortions due to the laser field. We use the wave-packet collision instead of a heuristic formula [19] in order to include Coulomb effects exactly in the determination of the structural effects. The initial state for this calculation is a superposition of the two-electron ground state $\Psi_0(x_1, x_2)$ and a symmetrized product of the ionic ground state $\varphi_g(x)$ with a Gaussian wave packet $\psi_G(x)$,

$$\Psi(x_1, x_2) = \alpha\, \Psi_0(x_1, x_2) + \beta\, S[\varphi_g(x_1)\, \psi_G(x_2)], \tag{4.11}$$

where S is the symmetrization operator for the two coordinates x_1, x_2. Here we have used that the system is in a singlet state with two opposite electron spins. The Gaussian wave packet

$$\psi_G(x) = \exp(-(x - x_0)^2/(2\sigma^2) + ikx) \tag{4.12}$$

is initially centered at $x_0 = 80\,\text{a.u.}$ with $\sigma = 0.3\,\text{a.u.}$, moving with a central momentum $k = -1.3\,\text{a.u.}$ toward the molecular ion. We set $\alpha/\beta = 10^3$ to mimic an HHG process in a weakly ionized system.

In the simulation of the laser-induced harmonic spectrum, we use trapezoidally shaped 1200 nm laser pulses with a total duration of 4 optical cycles and linear ramps of one optical cycle. The HHG spectrum for a two-electron molecule is obtained as the Fourier transform of the time-dependent dipole acceleration in the length gauge

$$S(\Omega) \sim \left| \int \langle \Psi(t) | (\partial_1 + \partial_2) V + 2E(t) | \Psi(t) \rangle e^{i\Omega t} dt \right|^2 . \tag{4.13}$$

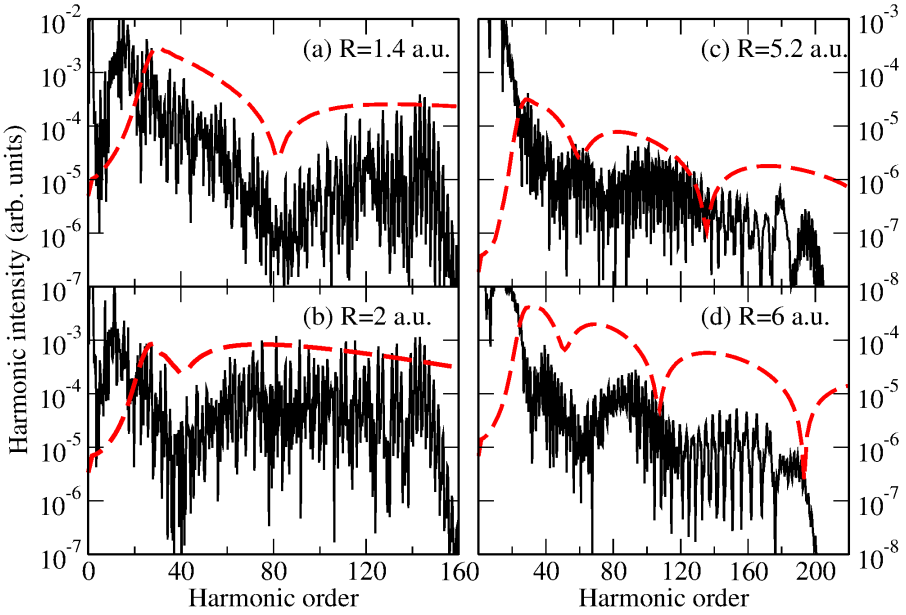

Figure 4.6: (Color online) HHG spectra for 1D H_2 at various internuclear distances. The laser intensity is $3 \times 10^{14}\,\mathrm{W/cm^2}$ in (a),(b) and $4 \times 10^{14}\,\mathrm{W/cm^2}$ in (c),(d). Dashed lines: spectra emitted by collision of a Gaussian wave packet with the molecular ion.

The HHG spectra at various internuclear distances are shown in Fig. 4.6 in comparison with the smooth HHG spectra from the wave-packet collision. At small internuclear distances ($R = 1.4\,\mathrm{a.u.}$ and $R = 2\,\mathrm{a.u.}$), we find that the minimum in the collision spectrum occurs at the same frequency as in laser-induced HHG. This shows that the suppression of the harmonic intensity is a purely structural effect. Indeed it originates from destructive two-center interference [18, 19, 36]. As the internuclear distance is increased, the energy gap ΔE between the ionic ground state and first excited state is reduced ($R = 5.2\,\mathrm{a.u.}$, $\Delta E = 0.0566\,\mathrm{a.u.}$; $R = 6\,\mathrm{a.u.}$, $\Delta E = 0.0302\,\mathrm{a.u.}$). Ionization to the excited ionic state may start to play a role. As can be seen from Figures 4.6(c) and (d), the minima in the collision spectra appear at frequencies different from the laser-induced spectra. This demonstrates that ionization to the ionic ground state is not sufficient to explain HHG at increased distance.

4.3.2 Two-channel HHG

Two channels, i.e. the ionic ground state and first excited state, must be taken into account to understand the HHG spectra. We introduce a recollision model for describing the extrema in the HHG spectrum. The essential ingredients of the model are the ionization phase, the bound-electron

motion, and the recombination phase. We assume that at times t close to recollision, the system is in a superposition of the two-electron ground state $\Psi_0(x_1, x_2, t) = \Psi_0(x_1, x_2)e^{-iE_0 t}$ and a symmetrized product of a bound ionic wave packet ψ^+ with a continuum wave packet $\psi_c(x, t)$,

$$\Psi(x_1, x_2, t) = \alpha\Psi_0(x_1, x_2, t) + \beta S[\psi^+(x_1, t)\psi_c(x_2, t)]. \tag{4.14}$$

If the two ionic states are equally populated and if there is no laser-induced excitation between ionization and recombination, the ionic wave packet is

$$\psi^+(x, t) = \frac{1}{\sqrt{2}}\left(\varphi_g(x) + \varphi_u(x)e^{-i\omega\tau+i\phi}\right)e^{-iE_g\tau} \tag{4.15}$$

where E_g is the H_2^+ ground-state energy and $\omega = \Delta E$ is the energy gap between the ground and first excited state. However, in the presence of the laser field, we deduce from our calculations that the wave packets oscillate approximately with the laser frequency and therefore we set ω equal to the laser frequency. The travel time $\tau = t - t_i$ determines the dynamical phase $\omega\tau$ accumulated after ionization. The molecular ground state at large internuclear separation is well approximated by the Heitler-London-type function

$$\Psi_0(x_1, x_2) = \frac{1}{\sqrt{2}}\left(\varphi_g(x_1)\varphi_g(x_2) - \varphi_u(x_1)\varphi_u(x_2)\right). \tag{4.16}$$

The Dyson orbitals, defined as the overlaps between the neutral ground state and the ionic states, corresponding to the ionic states φ_g and φ_u are then $D_g = \sqrt{2}\langle\varphi_g|\Psi_0\rangle = \varphi_g$ and $D_u = \sqrt{2}\langle\varphi_u|\Psi_0\rangle = -\varphi_u$. The emission spectrum $S(\Omega)$ is proportional to the modulus squared of the Fourier transform of the dipole-velocity expectation value [120]

$$v_d(t) = i\langle\Psi(t)|\partial_1 + \partial_2|\Psi(t)\rangle. \tag{4.17}$$

We set the continuum wave packet to a plane wave $\psi_c(x, t) = e^{ikx-iE_k t}$ with momentum k. Using the following equations

$$\begin{aligned} \langle\,\varphi_g\,|\,\partial_x\,|\,\varphi_g\,\rangle &= 0 \\ \langle\,\varphi_g\,|\,\varphi_u\,\rangle &= 0 \end{aligned} \tag{4.18}$$

and linear combinations of atomic orbitals for the states φ_g and φ_u yields

$$\begin{aligned} \langle\, \psi_c(t) \,|\, \partial_x \,|\, \varphi_g \,\rangle &= 2\cos\left(\frac{kR}{2}\right) v_{at} \\ \langle\, \psi_c(t) \,|\, \partial_x \,|\, \varphi_u \,\rangle &= -2i\sin\left(\frac{kR}{2}\right) v_{at}, \end{aligned} \tag{4.19}$$

where $v_{at} = i\langle \psi_c(t) \,|\, \partial_x \,|\, \varphi_{at} \,\rangle$ is the recombination dipole velocity for the ground state of hydrogen atom. Keeping only continuum-bound transitions, and neglecting exchange contributions [121, 122] leads (within a temporal saddle-point approximation) to the expression of the dipole velocity

$$\begin{aligned} v_d(t) &= i\langle\, \psi_c \,|\partial_x \,|\, \varphi_g \,\rangle \,-\, i\langle\, \psi_c \,|\partial_x \,|\, \varphi_u \,\rangle e^{i\omega\tau - i\phi} \\ &= i\left(2\cos\frac{kR}{2} + 2i\sin\frac{kR}{2} e^{i\omega\tau - i\phi}\right) v_{at}. \end{aligned} \tag{4.20}$$

Then one obtains the final results

$$S(\Omega) \,\sim\, |v_d|^2 \,\sim\, 1 - \sin(|k|R)\,\sin(\omega\tau - \phi), \tag{4.21}$$

which includes both the structural and dynamical interference effects. In this model, we have assumed that the excited-state channel has the same trajectories as the ground state (neglecting the difference in ionization energy) and we have used that the recombination matrix elements for the gerade and ungerade states differ by a phase of $\pi/2$, see Eq. (4.19). The harmonic photon energy Ω is the sum of the kinetic recollision energy and the ionization potential I_p, i.e. $\Omega = E_k + I_p$. The mapping between the photon energy Ω and the travel time τ can be obtained either from the classical three-step model or the quantum-orbit model. In the three-step model, the travel time τ is related to the kinetic energy E_k for the short trjectory as [123]

$$\omega\tau = 0.786[f(E_k/U_p)]^{1.207} + 3.304[f(E_k/U_p)]^{0.492} \tag{4.22}$$

with $f(x) = \arccos(1 - x/1.5866)/\pi$. In the quantum-orbit model, the travel time τ is mapped to the photon energy Ω using Eq. (2.49) and (2.50). In the end, we can evaluate the interference pattern predicted by Eq. (4.21) using the numerically obtained ionization phase ϕ from Fig. 4.5.

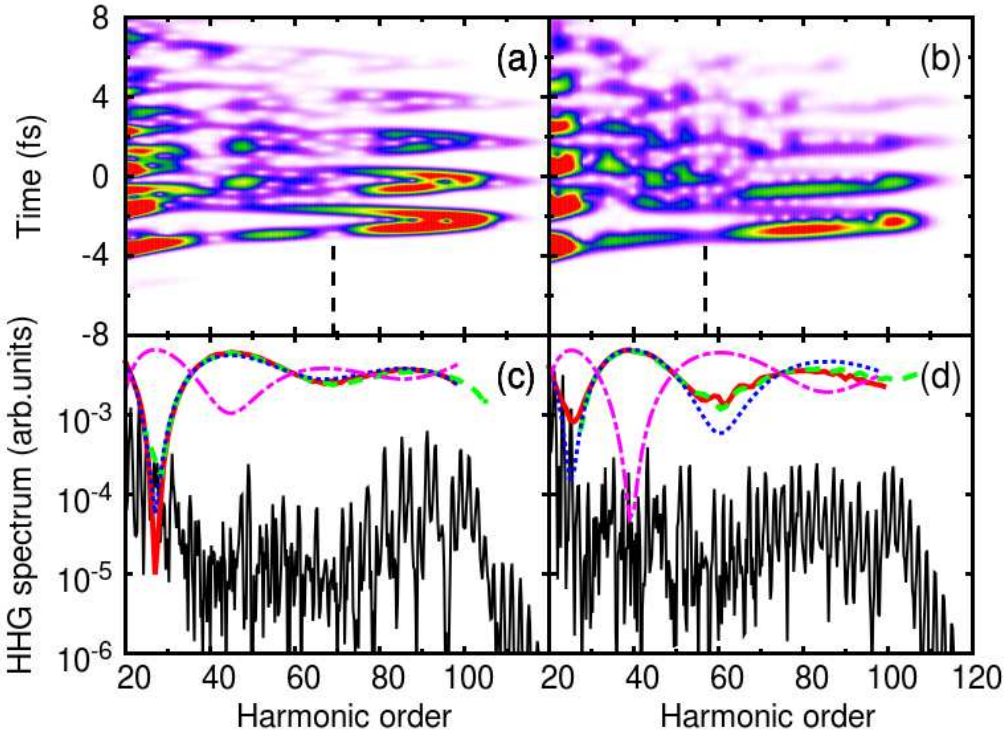

Figure 4.7: (Color online) Time-frequency analysis and HHG spectra of H_2 for the laser intensity $2 \times 10^{14}\,\mathrm{W/cm^2}$. Also shown are the emission spectra obtained using the recollision model, Eq. (4.21). Thick red solid lines represent the results with Eq. (4.22) and the ionization phase from Fig. 4.5; thick green dashed lines represent the results using times from the quantum-orbit model and the ionization phase from Fig. 4.5; thick blue dotted lines represent the results with Eq. (4.22) and $\phi = \pi$; thick magenta dot-dashed lines represent the results with Eq. (4.22) and $\phi = 0$. Left panel: $R = 5.2\,\mathrm{a.u.}$ Right panel: $R = 6\,\mathrm{a.u.}$

4.4 Results and discussion

In addition to the HHG spectra, we calculate the time-frequency distribution using the Gabor transform. The results are shown in Figs. 4.7 and 4.8 for two different laser intensities. Figs. 4.7(a),(b) show clear minima in the short trajectory at intermediate harmonic orders, namely at about harmonic 69 in Fig. 4.7(a) and harmonic 57 in Fig. 4.7(b). In the HHG spectra, these minima are visible, but less pronounced due to the summation over short and long trajectories. Using the recollision model with the ionization phase from Fig. 4.5, these minima are well reproduced. At the same orders, there is no interference minimum in the long trajectory, showing clearly the sensitivity to

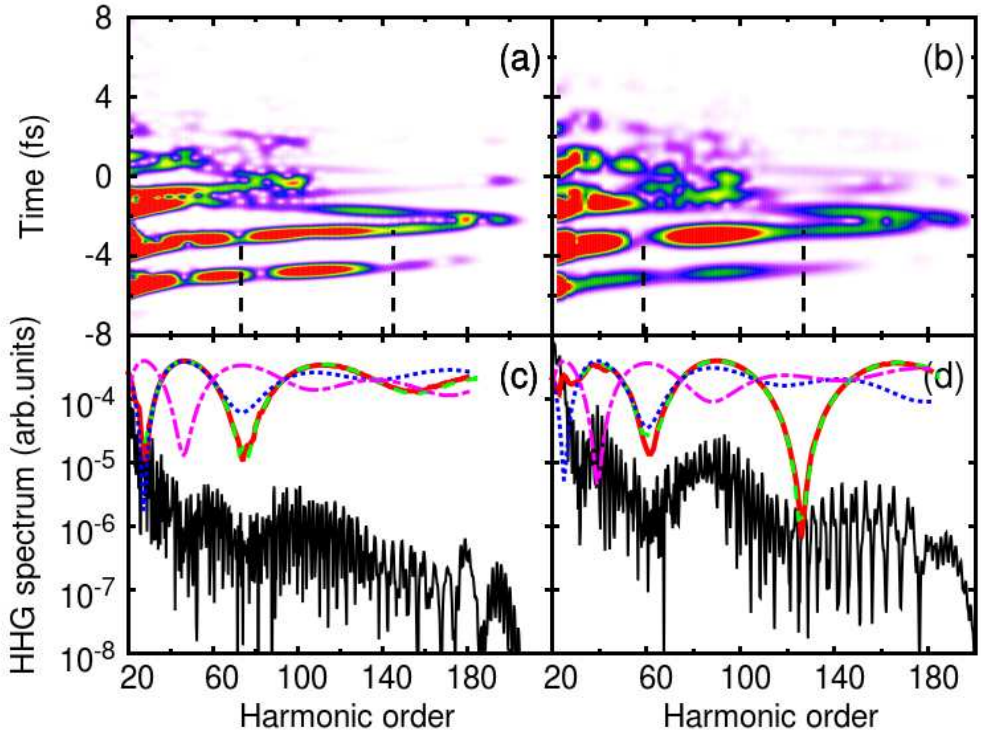

Figure 4.8: Same as 4.7 but for the intensity $4 \times 10^{14}\,\mathrm{W/cm^2}$.

the electron travel time, which is expected in multichannel interference. The model does not reproduce well the minimum at the lower harmonic order 40 in Fig. 4.7(c). This may be due to a low-energy failure of the model, which is based on plane waves and Coulomb-free trajectories. In general, however, the model reproduces the features of the numerical calculations well. This is seen also for the higher laser intensity in Fig. 4.8. The structures in the short trajectory in the range $-4\,\mathrm{fs} < t < -2\,\mathrm{fs}$ in Figs. 4.8(a),(b) are consistent with the model. The signal at earlier times comes from the rising edge of the laser pulse and should not be compared to the model. For $R = 6\,\mathrm{a.u.}$, the model now uses a phase significantly above π, see Fig. 4.5(b). Choosing the phase constant and equal to zero or π does not satisfactorily reproduce the numerical result. This is apparent by inspection of the minimum at harmonic order 125 in Fig. 4.8(d). Only the correct choice of phase in the interference model reproduces the minima. The HHG spectrum thus provides the information on the electron localization. This method of observing the electron dynamics can be adapted to more complex systems once the electronic states and transition matrix elements are known.

4.5 Conclusion

In summary, we have provided numerical evidence for bound wave-packet creation by strong-field ionization of two-electron molecules. The location of the initial wave packet can be controlled by varying the laser intensity. A simple recollision model has been applied to predict how the positions of interference minima in the HHG spectrum depend on the wave packet localization. The model shows good agreement with the numerical TDSE results provided that the correct ionization phase, i.e. the correct initial wave-packet location, is used. Our finding demonstrates the power of high-harmonic spectroscopy for molecular imaging on the subfemtosecond and Ångström scale. It may provide a new possibility for experimental investigation of ionization mechanisms such as the ion-pair-type enhanced ionization of H_2.

Chapter 5

Probing Fano resonances with ultrashort pulses

5.1 Introduction

Recently, the dynamical properties of Fano resonances caused by autoionization of metastable states have been investigated [66, 124–126]. Doubly excited states lying above the one-electron ionization threshold are prime examples of autoionizing states. The doubly excited states can be viewed as discrete states embedded in the continuum. They decay into a free electron and an ion in the ground state, with the kinetic energy of the free electron determined by conservation of energy. This type of decay is a prototype process governed by the electron-electron interaction. One-photon absorption from the ground state into the energy range around a doubly excited state leads to ionization along two possible paths: either direct ionization into the background continuum or indirect ionization via the autoionizing resonance. The interference of the two paths gives rise to an asymmetric absorption line, which is known as the Fano profile [71], as illustrated in Fig. 5.1. The Fano profile is found both in photoelectron spectra and in photoabsorption spectra. In this work, we focus on the photoelectron spectra.

We begin with a detailed introduction to the Fano resonance theory, following exactly the treatment of [71, 125, 127]. We obtain the asymmetric Fano line profile in the energy domain and the decay amplitude of the Fano resonance in the time domain. We calculate the photoelectron spectrum for the 1D helium model atom by numerical solution of the TDSE. We investigate the situation that a quasibound wave packet is formed by irradiation with a spectrally broad XUV pulse that covers several autoionizing states. We calculate the photoelectron spectrum as a function of the time delay between the XUV pulse and the laser pulse. Our results explain well the recent experiments on

time-resolved autoionization dynamics. For the presentation of the results, energies and times are given in units of eV and fs in this chapter.

5.2 Review of the Fano resonance theory

5.2.1 Fano line profile in energy domain

First, we give a brief introduction to the Fano resonance theory [71]. We start with a doubly excited state of helium atom. The zero-order unperturbed Hamiltonian H_0 of helium, neglecting the electron-electron interaction, is

$$H_0 \;=\; -\sum_{i=1,2}\left(\frac{1}{2}\nabla^2_{\mathbf{r}_i} \;+\; \frac{2}{\mathbf{r}_i}\right), \tag{5.1}$$

being the sum of two hydrogenic Hamiltonians. Consider a doubly excited state with energy E_ψ, which lies within the continuous range of values of E. Within the zero-order approximation, the doubly excited state $|\phi_{E_\phi}\rangle$ and the continuum state $|\psi_E\rangle$ are given by $H_0|\phi_{E_\phi}\rangle = E_\phi|\phi_{E_\phi}\rangle$ and $H_0|\psi_E\rangle = E|\psi_E\rangle$. The first step of Fano's treatment is to find the eigenstate $|\Psi_E\rangle$ of the total Hamiltonian $H \;=\; H_0 \;+\; V_{ee}$, with the electron-electron interaction

$$V_{ee} = \frac{1}{\mathbf{r}_{12}}. \tag{5.2}$$

The eigenstate $|\Psi_E\rangle$ of the total Hamiltonian H can be expanded using the doubly excited state $|\phi_{E_\phi}\rangle$ and the continuum states $|\psi_E\rangle$ as bases

$$|\Psi_E\rangle \;=\; a|\phi_{E_\phi}\rangle \;+\; \int dE' b_{E'}|\psi_{E'}\rangle. \tag{5.3}$$

The couplings between these orthogonal states by the total Hamiltonian are given by

$$\begin{aligned}
\langle\phi_{E_\phi}\,|\,H\,|\,\phi_{E_\phi}\rangle &= E_\phi \\
\langle\psi_{E'}\,|\,H\,|\,\psi_E\rangle &= E'\delta(E \;-\; E') \\
\langle\psi_E\,|\,H\,|\,\phi_{E_\phi}\rangle &= \langle\psi_E\,|\,V_{ee}\,|\,\phi_{E_\phi}\rangle \;=\; V_E,
\end{aligned} \tag{5.4}$$

where V_E is the configuration interaction that couples the discrete doubly excited state and the nearby continuum states. Inserting Eq. (5.3) into the eigenvalue equation $H|\Psi_E\rangle \;=\; E|\Psi_E\rangle$, and using the coupling relations Eq. (5.4),

we find the coefficients a and $b_{E'}$ satisfying the equations

$$aE = aE_\phi + \int dE'\, b_{E'} V^*_{E'}, \tag{5.5}$$

$$b_{E'} E = aV_{E'} + b_{E'} E'. \tag{5.6}$$

Following the treatment of [71], the solution of Eqs. (5.5), (5.6) are assumed to take the form

$$b_{E'} = \left[\frac{1}{E - E'} + \frac{E - E_\phi - F(E)}{|V_E|^2} \delta(E - E') \right] V_{E'} a, \tag{5.7}$$

instead of $b_{E'} = \frac{V_{E'} a}{E - E'}$ to avoid the singularity at $E = E'$, with

$$F(E) = \mathcal{P} \int dE' \frac{|V_{E'}|^2}{E - E'}, \tag{5.8}$$

and $\mathcal{P}$ indicates the principle part of the integral. The value of $F(E)$ represents a shift of the resonance energy with respect to E_ϕ due to the configuration interaction V_E.

If the continuum states $|\psi_{E'}\rangle$ are represented by a wavefunction with asymptotic behavior

$$|\psi_{E'}\rangle \propto \sin\left[k(E')r + \delta\right], \tag{5.9}$$

their superposition, i.e. the second term in Eq. (5.3), with the coefficient b'_E in Eq. (5.7) has the simple form

$$\int dE' b_{E'} |\psi_{E'}\rangle \propto \sin\left[k(E)r + \delta + \Delta\right], \tag{5.10}$$

with the phase shift caused by the configuration interaction V_E

$$\Delta = -\arctan\left[\frac{\pi |V_E|^2}{E - E_\phi - F(E)} \right]. \tag{5.11}$$

From Eqs. (5.7) and (5.11), one can obtain the coefficients a and $b_{E'}$

$$a = \frac{\sin\Delta}{\pi V_E}, \tag{5.12}$$

$$b_{E'} = \frac{V_{E'}}{E - E'} a - \delta(E - E') \cos\Delta. \tag{5.13}$$

Inserting the coefficients in Eqs. (5.12) and (5.13) into the eigenstate $|\Psi_E\rangle$

Eq. (5.3), we obtain

$$\begin{aligned} |\Psi_E\rangle &= a|\phi_{E_\phi}\rangle + a\int dE' \frac{V_{E'}}{E-E'}|\psi_{E'}\rangle - |\psi_E\rangle\cos\Delta \\ &= a|\Phi\rangle - |\psi_E\rangle\cos\Delta \\ &= \frac{1}{\pi V_E}|\Phi\rangle\sin\Delta - |\psi_E\rangle\cos\Delta, \end{aligned} \tag{5.14}$$

where

$$|\Phi\rangle = |\phi_{E_\phi}\rangle + \mathcal{P}\int dE' \frac{V_{E'}}{E-E'}|\psi_{E'}\rangle \tag{5.15}$$

is the modified doubly excited state.

The transition probability from an initial state $|\Psi_i\rangle$ to the eigenstate $|\Psi_E\rangle$ is the modulus squared of the transition matrix element

$$\langle\Psi_E|T|\Psi_i\rangle = \frac{1}{\pi V_E^*}\langle\Phi|T|\Psi_i\rangle\sin\Delta - \langle\psi_E|T|\Psi_i\rangle\cos\Delta, \tag{5.16}$$

which consists of two separate parts: one is the transition matrix element from the initial state $|\Psi_i\rangle$ to the modified doubly excited state $|\Phi\rangle$ and the other is the transition to the continuum state $|\psi_E\rangle$. These two matrix elements interfere with opposite phase on the two sides of the resonance. The Fano parameter q is then defined as

$$q = \frac{\langle\Phi|T|\Psi_i\rangle}{\pi V_E^*\langle\psi_E|T|\Psi_i\rangle}, \tag{5.17}$$

which measures the relative strength of the ionization via the doubly excited state compared to direct ionization into the background continuum. A dimensionless reduced energy

$$\varepsilon = \frac{E - E_\phi - F(E)}{\Gamma/2} = -\cot\Delta \tag{5.18}$$

is introduced to measure the energy relative to the resonance position $E_r = E_\phi + F(E)$ in units of $\Gamma/2$, where

$$\Gamma = 2\pi|V_E|^2. \tag{5.19}$$

represents the spectral width of the resonance. Then the transition probability is given in the form of

$$|\langle\Psi_E\,|\,T\,|\,\Psi_i\rangle|^2 = |\langle\psi_E\,|\,T\,|\,\Psi_i\rangle|^2\,\frac{(q+\varepsilon)^2}{1+\varepsilon^2}. \tag{5.20}$$

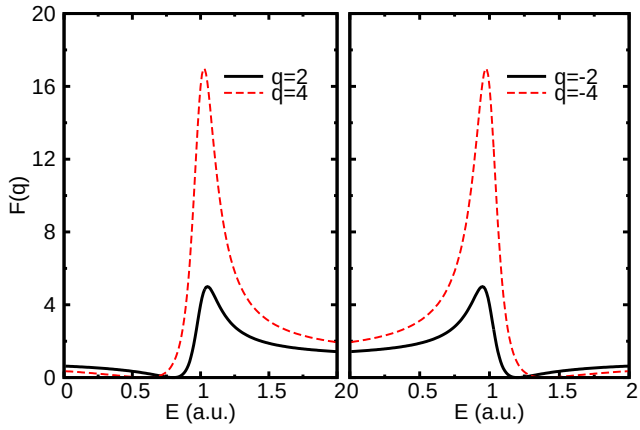

Figure 5.1: The Fano profile for various values of the asymmetry parameter q, with $\Gamma = 0.5$ a.u. and $E_r = 1$ a.u.

The ratio of the transition probability $|\langle \Psi_E \,|\, T \,|\, \Psi_i \rangle|^2$ to $|\langle \psi_E \,|\, T \,|\, \Psi_i \rangle|^2$ is described as the Fano profile:

$$P_{\mathrm{F}}(E) = \frac{(q+\varepsilon)^2}{1+\varepsilon^2}. \tag{5.21}$$

It has an asymmetric line profile with respect to the resonance energy E_r. The Fano parameter q determines the asymmetry of the Fano profile: for nonzero finite q, the line profile is asymmetric; for $|q| \to \infty$, i.e. the interference between discrete and continuum states is neglected, a Lorentzian profile is obtained. The shape of the Fano profile is illustrated in Fig. 5.1 for different values of the parameters.

In the above discussion we chose the stationary wave condition in Eq. (5.9). When incoming wave boundary condition, i.e.,

$$|\psi^-_{E'}\rangle \;\propto\; \exp\left[-i(k(E')r \;+\; \delta)\right] \tag{5.22}$$

is used in the formulation of the eigenstates in Eq. (5.3), namely,

$$|\Psi^-_E\rangle \;\propto\; \exp[-i(k(E)r + \delta + \Delta)], \tag{5.23}$$

and using Eqs. (5.16) and (5.17), the scattering amplitude from an initial state $|\Psi_i\rangle$ to the scattering state $|\Psi^-_E\rangle$ has the form

$$\begin{aligned} \langle \Psi^-_E | T | \Psi_i \rangle &= (q \sin\Delta - \cos\Delta) e^{i\Delta} \langle \psi^-_E | T | \Psi_i \rangle \\ &= -\langle \psi^-_E | T | \Psi_i \rangle \frac{q+\varepsilon}{i+\varepsilon}, \end{aligned} \tag{5.24}$$

with Δ being the eigen-phase shift [127]. The q-dependent factor $f_{\mathrm{F}}(E) = \frac{q+\varepsilon}{1-i\varepsilon}$ presents the amplitude of the Fano profile in the energy domain and can be decomposed into [128]

$$f_{\mathrm{F}}(E) = \frac{q-i}{1-i\varepsilon} + i \equiv (q-i)\frac{\Gamma}{2} f_{\mathrm{L}}(E) + i, \tag{5.25}$$

where $f_{\mathrm{L}}(E)$ is the amplitude of the Lorentz profile in the energy domain

$$f_{\mathrm{L}}(E) \;=\; \frac{1}{\Gamma/2 \;-\; i(E-E_r)}. \tag{5.26}$$

The Fano profile Eq. (5.21) is the modulus squared of the q-dependent factor.

5.2.2 Fano resonance in time domain

In a time-domain picture, the resonance can be considered as a continnous electron emitting process. First we consider a Lorentz resonance. In the time domain, the decay amplitude from a Lorentz resonance is described as

$$f_{\mathrm{L}}(t) = \exp(-iE_r t - \frac{\Gamma}{2}t). \tag{5.27}$$

The energy spectrum is given by the Fourier transform of the exponential decay amplitude from time 0 to infinite

$$\begin{aligned} F_{\mathrm{L}}(E) &= \left| \int_0^\infty dt f_{\mathrm{L}}(t) e^{iEt} \right|^2 \\ &= \frac{1}{(\Gamma/2)^2 + (E-E_r)^2}. \end{aligned} \tag{5.28}$$

The energy spectrum is symmetric with respect to the resonance energy E_r, corresponding to the case of $q \to \infty$ in Eq. (5.21). If the decay process is truncated at time t_d, for example by sudden ionization of the atom due to the presence of the laser field, the exponential decaying amplitude is Fourier transformed to the energy domain using as an upper limit not infinite time but a finite time t_d, yielding the truncated energy spectrum of the Lorentz resonance

$$\begin{aligned} F_{\mathrm{L}}(E, t_d) &= \left| \int_0^{t_d} dt\, f_{\mathrm{L}}(t)\, e^{iEt} \right|^2 \\ &= F_{\mathrm{L}}(E) \left[1 + e^{-\Gamma t_d} - 2e^{-\frac{\Gamma}{2}t_d} \cos\left[(E-E_r)t_d\right] \right], \end{aligned} \tag{5.29}$$

characterized by the oscillating term in Eq. (5.29) depending on the truncated time t_d. Similar to the Lorentz resonance, upon transforming the amplitude of the Fano profile (Eq. (5.25)) to the time domain yields the decay amplitude of a Fano resonance [125]

$$f_{\mathrm{F}}(t) = \frac{\Gamma}{2}(q-i)e^{-iE_r t-\Gamma t/2} + i\delta(t-0). \tag{5.30}$$

The first term describes the decay from the discrete state and the second term describes direct photoionization into the continuum state. The energy spectrum of a Fano resonance truncated at time t_d is given as

$$\begin{aligned} P_{\mathrm{F}}(E,t_d) &= \left| \int_0^{t_d} dt\, f_{\mathrm{F}}(t) e^{iEt} \right|^2 \\ &= \left| \frac{1}{i\varepsilon - 1} \left\{ \exp\left[i((E-E_r)t_d + \eta) - \frac{\Gamma}{2} t_d) \right] - (q+\varepsilon) \right\} \right|^2 \\ &= P_{\mathrm{F}}(E) \left[1 + \frac{1}{(q+\varepsilon)^2} e^{-\Gamma t_d} - \frac{2}{q+\varepsilon} e^{-\frac{\Gamma}{2} t_d} \cos[(E-E_r)t_d + \eta] \right] \end{aligned} \tag{5.31}$$

with $\eta = -\arctan(1/q)$.

5.3 Autoionization dynamics

5.3.1 One-dimensional model

Since the helium atom is the simplest system that exhibits autoionization, the autoionization dynamics from its doubly excited states has been studied exclusively via the XUV-pump-NIR-probe scheme [65, 66, 68, 69, 129]. It has been shown that laser-induced ionization and laser-induced coupling between the doubly excited states 2s2p and $2p^2$ of helium play a crucial role in the autoionization process, leading to modification of the Fano resonance profile. While the previous theoretical studies of time-resolved autoionization are based on the strong-field approximation or on few-level models, in this paper we approach the problem by numerical solution of the TDSE for a 1D helium model atom. The 1D atom exhibits a series of autoionizing states embedded in the single-ionization continuum [130]. The advantage of the 1D model is that the TDSE can be solved practically exactly with full account of the electron-electron interaction and without making assumptions about the dominant physical mechanisms.

The two-electron TDSE for the 1D helium atom in the presence of an

external field $E_{\text{ext}}(t)$ reads

$$i\,\partial_t\Psi(x_1,x_2,t) = \left[-\frac{\partial_1^2}{2} - \frac{\partial_2^2}{2} + V_0(x_1,x_2) + (x_1{+}x_2)E_{\text{ext}}(t)\right]\Psi(x_1,x_2,t) \tag{5.32}$$

with

$$V_0(x_1,x_2) = -\frac{2}{\sqrt{x_1^2+0.5}} - \frac{2}{\sqrt{x_2^2+0.5}} + \frac{1}{\sqrt{(x_1-x_2)^2+0.339}}. \tag{5.33}$$

The soft-core parameters are chosen to reproduce the ground-state energies of 3D helium and the He^+ ion [131]. The wave function $\Psi(x_1,x_2,t)$ is represented on a numerical grid with a spatial step size of 0.5 a.u. Due to the discreteness of our grid, the calculated energy values of the autoionizing states may differ slightly by a few tenths of an eV from the exact values. This has negligible effect on the presented results. The external field is a superposition of an XUV pulse E_{X}(t) and a NIR laser pulse E_{L}(t) linearly polarized in the same direction. We choose the frequencies $\omega_{\text{X}} = 1.84\,\text{a.u.} = 50.0\,\text{eV}$ and $\omega_{\text{L}} = 0.038\,\text{a.u.} = 1.03\,\text{eV}$ unless specified differently. The two pulses have the forms

$$E_{\text{X}}(t) = E_{0\text{X}}\exp\left(-(2\ln 2)\frac{t^2}{\tau_{\text{X}}^2}\right)\cos(\omega_{\text{X}}t) \tag{5.34}$$

and

$$E_{\text{L}}(t) = E_{0\text{L}}\cos^2\left(\frac{\pi(t-t_{\text{d}})}{2.75\tau_{\text{L}}}\right)\cos\Big(\omega_{\text{L}}(t-t_{\text{d}})+\phi\Big),\ |t-t_{\text{d}}| < 1.375\tau_{\text{L}}. \tag{5.35}$$

Here $E_{0\text{X}}$ and $E_{0\text{L}}$ are the electric-field amplitudes; τ_{X} and τ_{L} are the pulse durations defined as the full width at half maximum (FWHM) of the intensity envelope; ϕ is the carrier envelope phase of the laser pulse and t_{d} is the time delay between the centres of the laser pulse and the XUV pulse. The sign of the delay is chosen such that for positive delays, the XUV pulse acts before the laser pulse.

First, we calculate the energy levels of the unperturbed 1D helium model using the autocorrelation function method (section 2.4.3). Propagating from an arbitrary initial state yields the energies of the eigenstates contained in the initial state. Singlet states can be obtained from an initial state with space-symmetry, which remains unchanged upon exchanging the coordinates of the two electrons, i.e. $\Psi(x_1,x_2) = \Psi(x_2,x_1)$. Triplet states satisfy $\Psi(x_1,x_2) = -\Psi(x_2,x_1)$. Since the Hamiltonian is invariant under the parity operation ($x_1{\to}{-}x_1$, $x_2{\to}{-}x_2$), the nondegenerate eigenfunctions must satisfy the condi-

tion $\Psi(x_1, x_2) = \pm\Psi(-x_1, -x_2)$, namely they have well-defined parity. In this work, we focus on the singlet states of helium atom. To distinguish the parity of the states, we choose two different initial states. One is a Gaussian wave packet

$$\Psi_G(x_1, x_2) = \exp\left[-(x_1+4)^2/10 - (x_2+2)^2/10\right], \tag{5.36}$$

and the other is an even-parity wave packet

$$\Psi_s(x_1, x_2) = \sin(x_1)\sin(x_2)\exp\left(-x_1^2/10 - x_2^2/10\right), \tag{5.37}$$

comprising only eigenfunctions satisfying $\Psi(x_1, x_2) = \Psi(-x_1, -x_2)$. Moreover, we can get the triplet eigenstates of the 1D helium using the initial wave packet

$$\Psi_T(x_1, x_2) = \frac{1}{\sqrt{2}}\left[\Psi_G(x_1, x_2) - \Psi_G(x_2, x_1)\right]. \tag{5.38}$$

The corresponding results are shown in Fig. 5.2. Here we set the energy scale such that the ground-state energy equals 0. According to the parity property of the eigenstates, some relevant levels are labeled in Fig. 5.2. The notation $|n_1, n_2\rangle$ indicates that, in the limit of noninteracting electrons, one of the electrons is in the state $|n_1\rangle$ of He^+ and the other is in the state $|n_2\rangle$. Here, $n=1$ refers to the ground state, $n=2$ to the first excited state and so on.

For the simulation describing the interaction with the field, the TDSE is solved by means of the split-operator technique [102] with 64 time steps per XUV cycle. The time evolution starts from the singlet ground state, which is obtained by imaginary-time propagation. Therefore the system is in a singlet state at all times, i.e. the wave function $\Psi(x_1, x_2, t)$ must be symmetric with respect to exchange of the electron position coordinates x_1 and x_2. Absorbing boundaries are employed but the grid is chosen large enough (at least 2000 a.u. in each coordinate) to ensure that electrons will not reach the boundaries before the end of the pulses. We isolate the non-ground-state part $\bar{\Psi}(x_1, x_2, t_0)$ of the wave function at time t_0 after the pulses by projecting out the ground state. To obtain the photoelectron spectrum, the wave function is then propagated further in time without external field until a final time t_f. From the time-dependent wave function, we obtain the photoelectron spectrum via the autocorrelation function as in section 2.4.3. We use a long time interval $t_\mathrm{f} - t_0 = 3420$ a.u. for all calculations to guarantee sufficient energy resolution. Since autoionization of doubly excited states leaves the ion in the ground state, the kinetic energy E_f of the outgoing electron is determined by energy conservation, $E = E_\mathrm{f} + E_\mathrm{g}^+$, with E_g^+ being the ground-state energy of

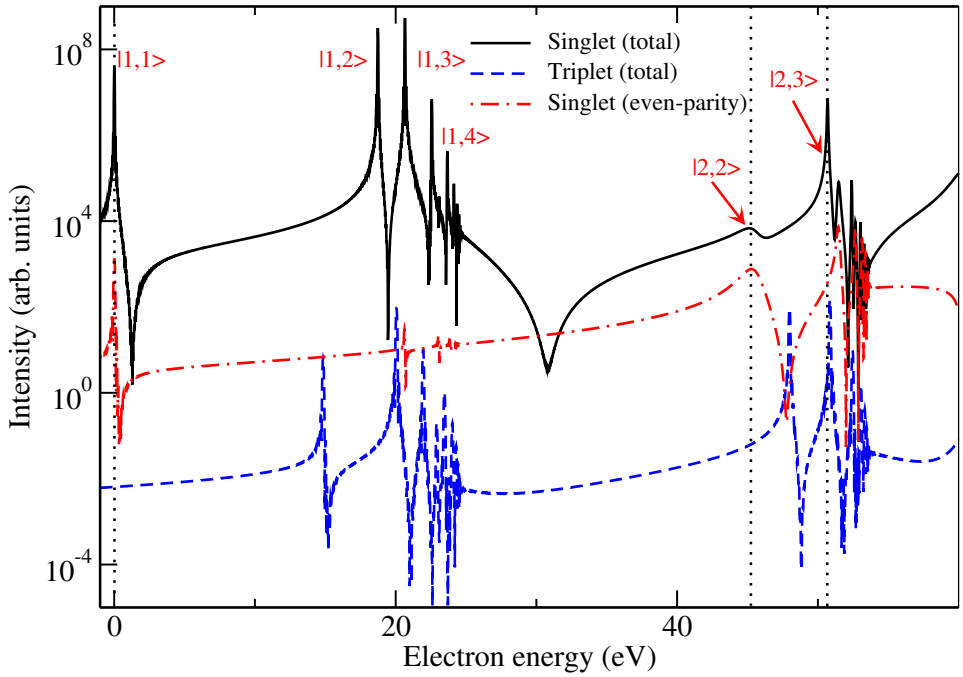

Figure 5.2: Energy levels of the 1D helium model atom. The solid curve predicts energy levels of singlet states with both odd- and even-parity; the dot-dashed curve predicts the energy levels of singlet states with even-parity; the dashed curve predicts energy levels of triplet states with both odd- and even-parity.

the singly-charged ion.

5.3.2 Wave-packet dynamics after XUV excitation

It is instructive to first present the relevant energy level diagram of the 1D helium atom and the photoelectron spectrum after an attosecond XUV excitation. The state $|2,3\rangle$ at $E = 50.69$ eV is the lowest doubly excited state reachable by one-photon absorption from the ground state. The even-parity state $|2,4\rangle$ is 0.75 eV above the state $|2,3\rangle$ and the state $|2,5\rangle$ is at $E = 52.41$ eV. The energy spectrum after irradiation with an attosecond XUV pulse with FWHM $\tau_X = 171$ attoseconds is shown in the right part of Fig. 5.3(a). The broad spectral distribution reflects the bandwidth of the XUV pump pulse. Due to the selection rules for electric dipole transitions, only the odd-parity states are populated by the attosecond XUV pulse. Therefore the doubly excited states $|2,3\rangle$ and $|2,5\rangle$ can be reached with one XUV photon, but not the states $|2,2\rangle$ and $|2,4\rangle$. Note that the simultaneous XUV-induced population of different autoionizing states has been addressed only rarely in the literature [60, 125, 132]. The electron energy spectrum near a doubly excited

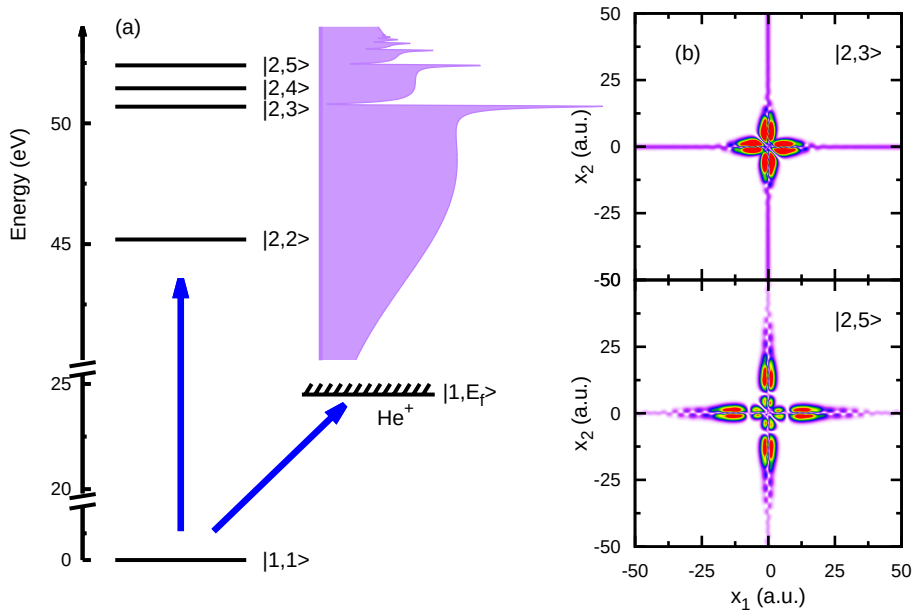

Figure 5.3: (a) Energy level diagram of the $|2, n\rangle$ autoionizing states in the 1D helium model and the energy spectrum after action of a short XUV pulse. (b) Wave packets generated by excitation with long XUV pulses resonant with the states $|2, 3\rangle$ and $|2, 5\rangle$, respectively.

state is given by the Beutler-Fano function Eq. (5.21). The XUV-induced spectrum in Fig. 5.3(a) beautifully exhibits the typical asymmetric absorption lines. The largest weights are found for the states $|2, 3\rangle$ and $|2, 5\rangle$. By fitting the spectrum to Beutler-Fano functions, the parameters of the resonance state $|2, 3\rangle$ are $E_\mathrm{r} = 50.69$ eV, $\Gamma = 0.086$ eV and $q = -1.21$; the parameters for the state $|2, 5\rangle$ are $E_\mathrm{r} = 52.41$ eV, $\Gamma = 0.054$ eV and $q = -1.17$. In comparison, the numbers for the well known 2s2p resonance in the real helium atom are $E_\mathrm{r} = 60.15$ eV, $\Gamma = 0.037$ eV and $q = -2.75$ [133].

To obtain pictures of the doubly excited states, we excite the atom with longer XUV pulses such that only one of the states is covered by the bandwidth of the pulse. To select the $|2, 3\rangle$ or $|2, 5\rangle$ state, the XUV frequency is centred at 50.7 eV or 52.4 eV, respectively. The XUV pulse length (FWHM) is about 6.9 fs. By projecting out the two-electron ground state from the wave function after XUV irradiation, the two-electron wave packet containing the autoionizing state can be isolated. The modulus squared of the resulting wave functions is plotted in Fig. 5.3(b). The nodal structure is consistent with the single-particle excitations indicated by the quantum numbers. The wave function at large $|x_1|$ or large $|x_2|$ shows the transition of the quasi-bound state into an

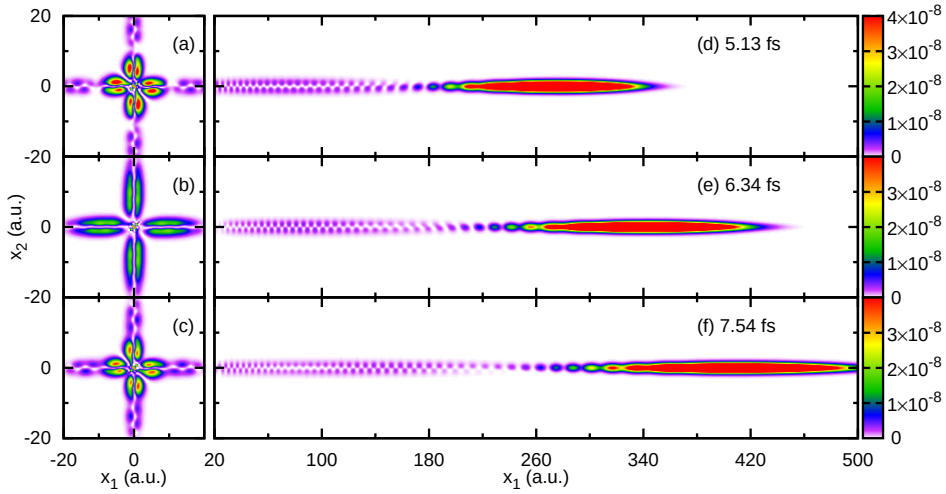

Figure 5.4: Left: Modulus squared of the inner part of the two-electron wave packet after the XUV pulse, taken at different times. Right: Modulus squared of the outer part of the wave function. The times in (a),(b),(c) are the same as in (d),(e),(f).

outgoing electron with the other electron bound in the nodeless single-electron ground state.

Returning to the case of attosecond XUV excitation, we show in Fig. 5.4 the modulus squared of the two-electron wave packet (where the ground state has been projected out) at different times after the XUV pulse. The XUV parameters for these and the following simulations are: pulse length 171 attoseconds, central photon energy 50 eV and peak intensity 10^{12} W/cm^2. At 5.13 fs after the XUV pulse, the inner-part wave packet resembles to some extent the autoionizing state $|2,3\rangle$ in Fig. 5.3. However, the coherent superposition of autoionizing states expresses itself in an oscillation of the quasi-bound wave packet in time. The period of this oscillation is expected to be $T = 2\pi/(E_{|2,5\rangle} - E_{|2,3\rangle}) = 2.41$ fs. The time evolution displayed from Fig. 5.4(a) to Fig. 5.4(c) clearly confirms the oscillation of the wave packet within the expected period. At the same time, comparison of Fig. 5.4(a) and 5.4(c) shows the decrease of the overall population of the doubly excited states due to the decay.

The right panels of Fig. 5.4 show the wave function in the outer region. Obviously, the outgoing wave function consists of two parts. One is the broad continuous wave packet, plotted in red colour, representing direct ionization to the continuum. It escapes the core region immediately after excitation. The other part, lagging behind, represents an electron emerging by decay of

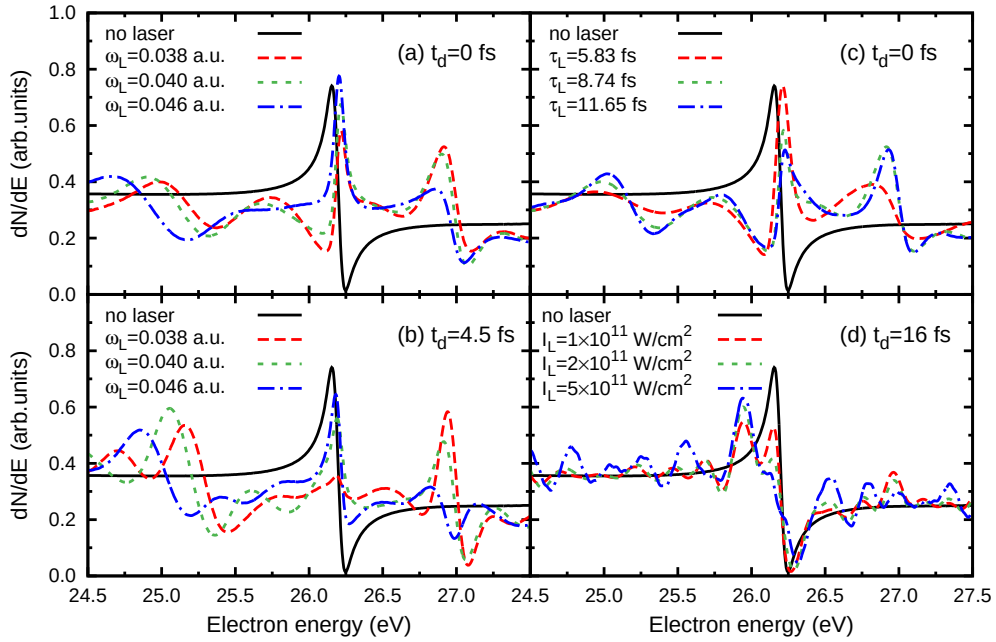

Figure 5.5: (a) Photoelectron spectra for different laser frequencies ω_L at time delay zero. (b) Same as (a) for the time delay 4.5 fs. (c) Photoelectron spectra with different laser pulse lengths. The frequency is ω_L =0.038 a.u. (d) Photoelectron spectra for various laser intensities at time delay 16 fs (no overlap between XUV and laser pulses). The laser pulse lengths in (a), (b) and (d) are τ_L =8.74 fs for ω_L = 0.038 a.u., τ_L =8.30 fs for ω_L = 0.040 a.u. and τ_L =7.22 fs for ω_L = 0.046 a.u.

autoionizing states. The coherent superposition of autoionizing states leads to interference in the outgoing waves. This interference is responsible for the slow oscillation along the x_1 axis. The spatial period of about 140 a.u. matches the momentum difference between electrons from the states $|2,3\rangle$ and $|2,5\rangle$. The momenta of electrons from these two states are 1.389 a.u. and 1.434 a.u. The interference of these outgoing waves with quasi-bound Rydberg states (which can be thought of as extended momentum-zero states) leads to the fast oscillation with a spatial period of about 4.5 a.u.

5.3.3 Laser-induced autoionization

In the XUV-pump-NIR-probe method, a single attosecond XUV pulse with broad bandwidth creates a wave packet consisting of several doubly excited states. A time-delayed NIR laser pulse probes the autoionization dynamics. In the following, we investigate in detail the probing of the autoioniz-

ing wave-packet dynamics by a NIR laser pulse. The laser peak intensity in these simulations is $2\times10^{11}\,\mathrm{W/cm^2}$ except for Fig. 5.5(d) where also the intensities $1\times10^{11}\,\mathrm{W/cm^2}$ and $5\times10^{11}\,\mathrm{W/cm^2}$ are used as indicated. We inspect the photoelectron spectrum around the $|2,3\rangle$ absorption line for a variety of laser parameters. The energy axis in these plots gives the kinetic energy E_f of the outgoing electron. First, we compare different laser wavelengths for zero time delay between the XUV and NIR pulses, see Fig. 5.5(a). The frequencies 0.038, 0.040, 0.046 a.u. correspond to the wavelengths 1.20, 1.14, 0.99 μm. It is apparent that the Fano profile at 26.26 eV is strongly modified by the laser field. Additionally, electrons with energies around 27 eV appear in the presence of the laser pulse. The position of this peak is found to be independent of the laser wavelength and it coincides with the $|2,4\rangle$ doubly excited state. The explanation is that the NIR laser field couples states of opposite parity. In a quasistatic picture, the instantaneous laser field dresses the states and XUV absorption to the dressed states need not respect the laser-free selection rules. When the laser field ends, population remains in the $|2,4\rangle$ state and it decays by autoionization. This process is found to become less efficient with increasing laser frequency. The line shape is obviously asymmetric. This shows that the autoionization of the $|2,4\rangle$ state interferes with the direct ionization path. Similar effects take place for the delay $t_\mathrm{d} = 4.5\,\mathrm{fs}$ as shown in Fig. 5.5(b). At this delay, we observe another characteristic feature of the XUV-pump-NIR-probe scheme, namely the appearance of a sideband: the peaks around 25 eV in Fig. 5.5(b) are one laser photon below the $|2,3\rangle$ resonance. For $t_\mathrm{d} = 0$ (Fig. 5.5(a)), the sideband is present as well, but it is less clear. A sideband could in principle exist also on the high-energy side of the resonance; it seems to be suppressed by the presence of the state $|2,4\rangle$ in the same energy region. Sidebands have been seen clearly in the XUV-pump-NIR-probe photoelectron spectra from helium [66]. Sideband intensities have been exploited to deduce the Auger lifetime of a Kr inner-shell excitation in [62], since the sideband can be created only during the lifetime of the populated metastable state. As discussed in [125], also the lifetime of a Fano resonance can be read from the decay of the sideband for non-overlapping XUV and laser pulses.

The photoelectron spectra for different laser pulse lengths are shown in Fig. 5.5(c). With increasing pulse length, there is more time available to form the sideband. At the same time, the central Fano profile is depleted. The population of the $|2,4\rangle$ state around 27 eV, however, is hardly increased by increasing the pulse length above 8.74 fs. This is in accordance with the physical interpretation that the population transfer to the $|2,4\rangle$ state is mainly

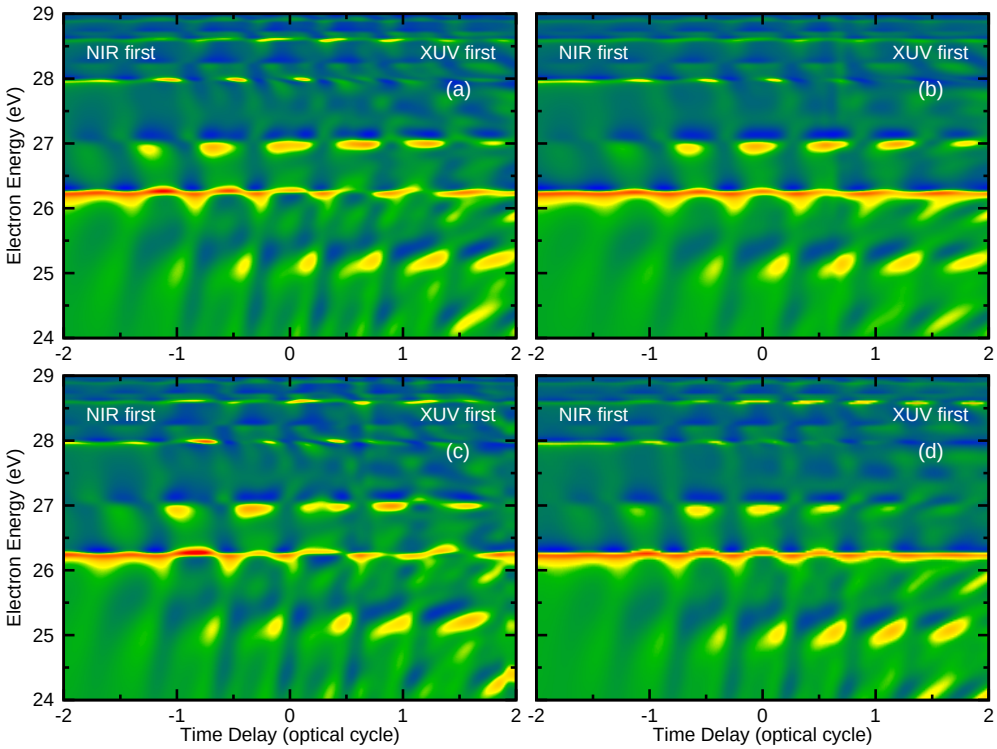

Figure 5.6: Photoelectron spectra as a function of time delay between the NIR and XUV pulses. (a),(d) Laser intensity 2×10^{11} W/cm^2, CEP ϕ =0. (b) Laser intensity 1×10^{11} W/cm^2, CEP ϕ =0. (c) Laser intensity 2×10^{11} W/cm^2, CEP $\phi = \pi/2$. The laser pulse length is τ_L =8.74 fs for ω_L =0.038 a.u. in (a), (b) and (c), and is τ_L =7.91 fs for ω_L =0.042 a.u. in (d).

achieved during the XUV pulse. Fig. 5.5(c) shows the modification of the Fano line shape at 26.26 eV very clearly. We find an inverse Fano line, which has been discussed before in [68].

At a larger time delay of 16 fs, the XUV and NIR pulses do not overlap in time any more. At this delay, the autoionizing states have substantially decayed so that the laser-assisted transfer of electrons to the sideband or to the $|2,4\rangle$ state is weak. The Fano profile, on the other hand, is strongly changed as compared to the laser-free profile. The spectrum is dominated by a side peak at 25.9 eV. Since the position of this peak is insensitive to the laser intensity (see figure), we do not interpret it in terms of Autler-Townes splitting [67, 134, 135]. Similar structures have been seen in the calculations of [68, 69] where they were explained as a superposition of the regular and an inverse Fano profile. We give a different interpretation later (Fig. 5.8).

The photoelectron spectra as a function of time delay, when the XUV and NIR overlap, are shown in Fig. 5.6. In the region of large negative delays,

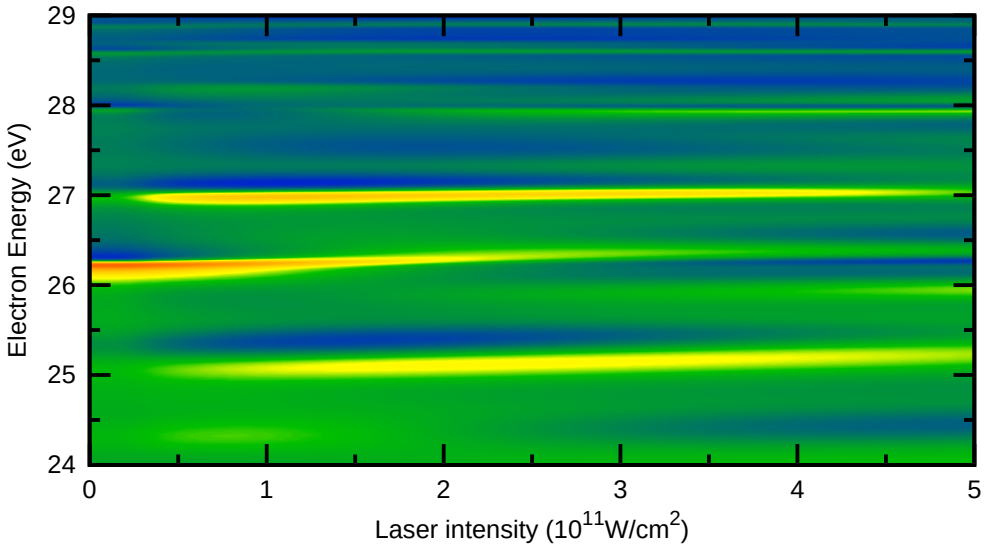

Figure 5.7: Photoelectron spectra for different laser intensities at a fixed time delay of 4 fs. The laser pulse length is τ_{L} =5.83 fs and the laser frequency is $\omega_{\mathrm{L}} = 0.038$ a.u.

the laser pulse arrives before the XUV pulse and only the tail of the laser pulse is involved in the dynamics. Therefore, the spectrum is similar to the XUV-only case. For overlapping XUV and laser pulses, complex behaviour of the spectrum is found. The efficiency of populating the $|2,4\rangle$ state at 27 eV oscillates as a function of delay with about half the period of the NIR field. In this case, the population in $|2,4\rangle$ is large when the XUV pulse arrives at a time of maximum of the laser field close to the centre of the laser pulse. This shows that the population is sensitive to the instantaneous electric field. In the simulation for a CEP of $\pi/2$ shown in Fig. 5.6(c), the oscillation in the $|2,4\rangle$ peak is accordingly phase-shifted with respect to the case of zero CEP in Fig. 5.6(a). We attribute the deviations from an exact half-cycle modulation to the rapidly varying envelope of the few-cycle laser pulses. It is interesting to note that the main Fano profile at the $|2,3\rangle$ state tends to be inverted at times of maximum population in $|2,4\rangle$. The sideband around 25 eV oscillates as a function of the time delay as well. Its maxima appear at the same times as the maxima of the $|2,4\rangle$ state. Simulations with the laser intensity 1×10^{11} W/cm^2 (Fig. 5.6(b)) and the laser frequency ω_{L} =0.042 a.u. (Fig. 5.6(d)) demonstrate that the oscillation period of the population in the $|2,4\rangle$ state and the sideband does not depend on the laser intensity and is indeed determined by the laser frequency.

Next, we investigate the photoelectron spectra versus the laser intensity at a

fixed time delay of 4 fs, shown in Fig. 5.7. We observe clearly an inversion of the Fano profile at the $|2,3\rangle$ state at laser intensities larger than $2\times10^{11}\,\mathrm{W/cm^2}$, which has been observed recently in the experiment [129], where the Fano-line-shape inversion is present in the state $|sp_{2,n+}\rangle$ with $n > 4$. Since the sign of asymmetry depends on the relative phase between the background continuum and the electron from the autoionizing states, the Fano-line-shape inversion can be explained by the additional dynamical phase of doubly excited states accumulated under the external laser field. The experiment also reveals clear Autler-Townes splitting of the $2s2p$ autoionizing state, as shown in Fig.4 in [129], while we do not observe it in our simulation. As for the $|2,4\rangle$ state and the sideband around 25 eV, their populations are almost stable within the range of $1.5 \sim 3.5\ \times10^{11}\,\mathrm{W/cm^2}$.

In the following we discuss the region where the laser pulse arrives after the XUV pulse without overlap. This is the case for time delays longer than 8 fs in Fig. 5.8. Apparently, the main Fano line at the $|2,3\rangle$ state is strongly depleted. We see a characteristic curved fringe pattern on the low-energy side and to a lesser extent on the high-energy side. Similar patterns have been found already in the previous theoretical studies in [69], but they have not been explained. The delay-dependent fringes due to the interference between electrons tunneled from bound excited states and direct ionization by XUV absorption have also been observed experimentally in [136]. It is one of these fringes that gives rise to the side peak at 25.9 eV in Fig. 5.5(d). Its position is independent of the laser intensity. Our results indicate that the overall pattern is not very sensitive to the laser pulse parameters. Instead, the fringes follow curves where the product $|E-E_\mathrm{r}|t_\mathrm{d}$ is constant with E_r being one of the resonance energies. For large delays, these fringes converge to the resonance energy. For example, the line between 27.5 and 27.8 eV at times $t_\mathrm{d} > 16$ fs approaches the $|2,5\rangle$ resonance at 28 eV from below. We can understand the appearance of these fringes as a consequence of a truncated decay of a metastable state, as we discussed in section 5.2.2. Hence, we expect that the condition for obtaining maximum or minimum signal follows curves satisfying $(E-E_r)t_\mathrm{d} + \eta = n\pi$ with integer n. This is confirmed by the photoelectron spectra in Fig. 5.8(a) and (b), corresponding to the attosecond pulses with pulse duration of $\tau_\mathrm{X} = 171$ as and $\tau_\mathrm{X} = 885$ as. They exhbit the same fringe pattern. For comparison, we show the prediction of our truncated autoionization model (Eq. 5.31) for the $|2,3\rangle$ state in Fig. 5.8(c), which agrees well with the photoelectron spectra from the TDSE simulations. It is natural to assume that the action of the time-delayed laser pulse can truncate the exponential decay, for example by sudden ioniza-

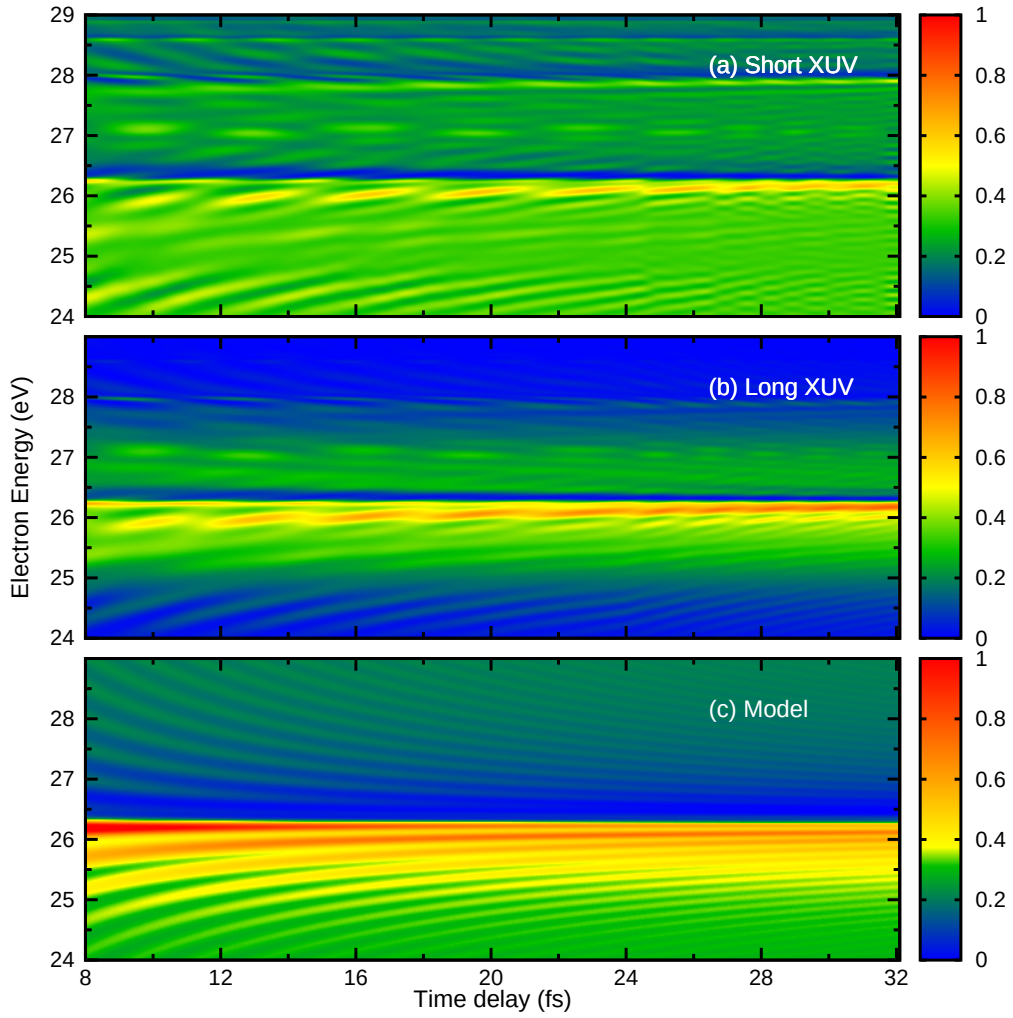

Figure 5.8: Photoelectron spectra as a function of time delay between the NIR and XUV pulses. (a) Short XUV pulse, $\tau_X = 171\,\text{as}$. (b) Long XUV pulse, $\tau_X = 855\,\text{as}$. (c) Truncated photoelectron spetrum of a single Fano resonance, Eq. (5.31). Laser pulse length in (a),(b) is $\tau_L = 5.83\,\text{fs}$ and laser frequency is ω_L =0.038 a.u.

tion of the atom. We may even speculate that the laser-induced line shifts of the autoionizing argon states measured in the experiment [67] are not due to an Autler-Townes-type splitting, but that they obey a fringe pattern law as described above. When the fringes are superimposed with the regular Fano profile (due to autoionizing decay after the NIR pulse in case that the doubly excited state has not been entirely emptied), a hybrid structure is formed as in Fig. 5.5(d) for the lowest laser intensity. Although our interpretation agrees with [68] to the extent that the overall spectrum is formed by overlaying the contributions from before and after the laser pulse, our understanding of the

pre-laser-pulse contribution is a different one. Another interesting feature in Fig. 5.8(a) is the modulation of the peak near 26 eV, just below the $|2,3\rangle$ resonance at 26.26 eV. It can be easily verified that the oscillation as a function of delay has a period of about 2.4 fs, in agreement with the energy gap between the states $|2,3\rangle$ and $|2,5\rangle$. This type of oscillation for coherent excitation of two resonances has been already pointed out in [125] and measured experimentally [126]. It corresponds to the quasi-periodic motion apparent in the coordinate-space plots in Fig. 5.4(a)-(c). The same oscillation period is found in the population of the $|2,4\rangle$ state at 27 eV in the photoelectron spectrum in Fig. 5.8(a). Closer inspection of these structures reveals that they exhibit also a slight modulation to higher and lower energies as the delay is varied. The period is given by the energy gap between the states $|2,3\rangle$ and $|2,4\rangle$. If we interpret the small energy shifts as the signature of an asymmetric line shape, it is easily understood that the sign of asymmetry depends on the relative phase between the background continuum and the electrons from the autoionizing $|2,4\rangle$ state. This relative phase must include the phase that the electrons have acquired in the $|2,3\rangle$ state before being transferred by the laser field to the $|2,4\rangle$ state. Thus, the sign of the Fano profile can simply be controlled by applying the laser pulse at a certain time delay.

5.4 Conclusion

Autoionization dynamics of 1D helium has been investigated by numerical solution of the time-dependent two-electron Schrödinger equation. An autoionizing wave packet is excited by an attosecond XUV pulse and probed by a time-delayed NIR laser pulse. Besides confirming previously known effects such as sideband formation and laser-induced coupling between autoionizing states, we have gained new insight into the laser-induced line shifts. The truncation of the autoionizing decay by the NIR field forms a universal fringe pattern in the photoelectron spectra. The peaks arising from the laser-induced coupling between states are modulated with time delay. This means that control of Fano line shapes is possible by suitable timing of an NIR pulse.

Chapter 6

Summary

With the rapid evolution in attosecond science, investigations on the ultrafast electronic dynamics in atoms and small molecules have attracted a lot of attention. Ongoing efforts have been undertaken to monitor and manipulate electron dynamics on the attosecond time scale. High-harmonic spectroscopy is a powerful tool to probe electronic dynamics in atoms and molecules. It relies on measuring the spectrum of coherent raidation, i.e. the high-harmonic generation spectrum, emitted by atoms and molecules interacting with an intense laser field. The observation and control of attosecond electronic dynamics can also be performed using the XUV-pump-NIR-probe scheme, with the XUV pulses available from high-harmonic generation, by analyzing directly the particles from laser-irradiated systems. The subject of this work is the theoretical investigation of several types of electronic dynamics in atoms and molecules. We approach these problems by numerical solution of the time-dependent Schrödinger equation for model atoms and molecules.

The first part of this work is to investigate the electron dynamics in laser-induced tunneling in atoms. According to the recollision model of harmonic generation, the ionization time, i.e. the time when an electron exits the tunneling barrier, is mapped to the harmonic frequency. In a recent experiment, the ionization time of the electron was determined using two-color high-harmonic spectroscopy, where an orthogonally polarized second-harmonic field was applied to manipulate the electron trajectory in two dimensions. The ionization and return times in high-order harmonic generation are retrieved by measuring the intensity for both even and odd harmonics as a function of the two-color delay, with a classical description of lateral electron motion. The retrieved times agree well with the quantum-orbit model, while quite different from the classical three-step model. In this work, following exactly the experimental procedure, we calculate the harmonic spectrum from numerical solution of both 2D and 3D TDSE. We find that the optimized two-color delays that

maximize the harmonic intensity and the amplitude ratio of even and odd harmonics deviate significantly from the results of the quantum-orbit model when the lateral electron motion is treated classicaly. We introduce an improved quantum mechanical retrieval method based on electron trajectories evolving in complex time. The model shows excellent agreement with our TDSE simulations. Complex treatment of the lateral motion has not been considered before. It has two substantial effects: it indicates that tunnel ionization induces electron displacement in the lateral direction, and also it explains the elliptically polarized bursts found in our TDSE results. Furthermore, we use this two-color scheme to retrieve the tunneling time, i.e. the imaginary part of the complex ionization time.

The second part of this work is motivated by a series of investigations on multichannel molecular high-order harmonic generation. These studies show that high-harmonic spectroscopy provides a unique insight into the initial shape and location of the hole left by field-induced one-electron ionization. It has been shown that the electron correlation effect plays an important role during tunneling ionization. In this work, we focus on the investigation of the correlated electron dynamics in field-induced ionization of the two-electron H_2 molecule at stretched internuclear separation. The energy gap between the ground and first excited states of the ion is comparable with the laser frequency, such that the ultrafast dynamics of the molecular ion takes place on a timescale comparable to the laser cycle and influences the harmonic spectrum. By analyzing the wavepacket motion after one-electron ionization, we find that strong-field ionization in combination with electron correlation can localize bound electron wave packets in molecules. The ionization phase difference between the gerade and ungerade channels depends on the internuclear distance and the laser intensity. With the parameters in our simulation, the ionization phase varies from π and 1.5π, implying that the bound wave packet is initially either on the same side as the outgoing electron or delocalized. We present a simple two-channel recollision model, including both the structural and dynamical interference effects. The model reproduces well the positions of the extrema in the harmonic spectra. We demonstrate that the location of the hole left by tunnel ionization can be manipulated by varying the laser intensity.

In the last part, we study the autoionization dynamics of Fano resonances. The natural approach to this task is to populate the metastable states with excitation by attosecond pulses, which are formed by high-order harmonic generation in laser-irradiated systems. We apply time-delayed near-infrared

laser pulses to probe the autoionization dynamics. Previous theoretical studies of time-resolved autoionization are based on the strong-field approximation or on few-level models. In this work, we consider the photoelectron spectrum of a 1D helium atom obtained by exact numerical solution of the TDSE. We find that the Fano line profile is strongly modified by the presence of the laser field. Laser-induced coupling between different doubly excited states populates autoionizing states that cannot be reached by absorbing a single XUV photon from the ground state. The resulting additional peaks in the photoelectron spectrum are modulated as a function of time delay. We observe clearly a fringe pattern in the photoelectron spectrum, which is understood as a consequence of the autoionizing decay being truncated by the laser field. The side peak of the Fano resonance observed in experiments is one of the these fringes.

The physcis of laser-matter interaction is very rich and complex. Visualizing and controlling bound electron dynamics in strong laser fields is one of the most active areas in strong field physics. So far the experimental and theoretical investigations are focused on simple atoms and molecules. Future work in this field will extend the scope of these methods to more complex systems.

Acknowledgements

I would like to express my special appreciation and thanks to my advisor Prof. Dr. Manfred Lein for his guidance, support and constant encouragement during my doctoral studies. I thank him for patiently answering all my questions and concerns on the projects. His serious attitude towards work had a great influence on my study. The joy and enthusiasm he has for scientific research was motivational and contagious for me, even during tough times in the PhD pursuit.

I would also like to thank my colleagues in our group, Jost Henkel, Ingo Dreißigacker, Maria Tudorovskaya, Elmar van der Zwan, Chirag Jhala and Lars Frahm for their help and fruitful discussions. I have really enjoyed being a member of this friendly and stimulating research group. I want to thank all respective people for proofreading my thesis and German corrections. In particular, I thank Jost Henkel for teaching me German. He helped me a lot during the past three years. Special thanks to our secretary Catharina Burmeister for her kindness and efficient assistance whenever I needed. I want to express my gratitude to Prof. Dr. Jianmin Yuan and Prof. Dr. Zengxiu Zhao for introducing the interesting research field to me and providing me the opportunity to study in Germany.

I want to thank Prof. Dr. Dieter Bauer for refereeing my thesis, and Prof. Dr. Uwe Morgner, Prof. Dr. Holger Frahm for taking time to serve on my dissertation committee.

I wish to thank all my friends from the university for the great time we had in Germany.

Finally, I would like to thank my family for their love and constant support.

Curriculum Vitae

Jing Zhao

- Date of Birth: Jul. 05, 1985
- Place of Birth: Hebei, China
- Nationality: Chinese
- Address: Institut für Theoretische Physik,
  Leibniz Universität Hannover
  Appelstr 2, 30167 Hannover, Deutschland
- Phone: +49 (0) 511 762 3368
- E-Mail: jing.zhao@itp.uni-hannover.de

Education

- **Feb. 2010 -**, Ph.D, Institute of Theoretical Physics, Leibniz University Hannover, Hannover, Germany,
  Thesis: *High-harmonic spectroscopy of atoms and molecules*
  Advisor: Prof. Dr. Manfred Lein

- **Sep. 2006 - Dec. 2008**, M.Sc, Atomic and Molecular Physics, Institute of Physics, National University of Defense Technology, Changsha, P. R. China,
  M.Sc thesis: *High-order harmonic generation from* H_2^+
  Advisor: Prof. Dr. Zengxiu Zhao

- **Sep. 2002 - Jun. 2006**, B.Sc, Institute of Physics, National University of Defense Technology, Changsha, P. R. China,

Publications

1. J. Zhao and M. Lein *Determination of ionization and tunneling times in high-order harmonic generation*, submitted.
2. J. Zhao and M. Lein, *Probing Fano resonances with ultrashort pulses*, New J. Phys. **14**, 065003 (2012).
3. J. Zhao and M. Lein, *Positioning of bound electron wave packets in molecules revealed by high-harmonic spectroscopy*, J. Phys. Chem. A **116**, 2723 (2012).
4. J. Zhao and Z. X. Zhao, *Effects of Bounding Potential on High-Order Harmonic Generation with Hydrogen Molecular Ion*, Chin. Phys. Lett. **27**, 063301 (2010).
5. J. Zhao and Z. X. Zhao, *Probing* H_2^+ *vibrational motions with high-order harmonic generation*, Phys. Rev. A **78**, 053414 (2008).

Bibliography

[1] T. Brabec and F. Krausz, Rev. Mod. Phys. **72**, 545 (2000).

[2] M. Protopapas, C. H. Keitel, and P. L. Knight, Rep. Prog. Phys. **60**, 389 (1997).

[3] P. B. Corkum, Phys. Rev. Lett. **71**, 1994 (1993).

[4] H. Niikura, F. Legare, R. Hasbani, A. D. Bandrauk, M. Y. Ivanov, D. M. Villeneuve, and P. B. Corkum, Nature **417**, 917 (2002), ISSN 0028-0836.

[5] D. Akoury, K. Kreidi, T. Jahnke, T. Weber, A. Staudte, M. Schöffler, N. Neumann, J. Titze, L. P. H. Schmidt, A. Czasch, et al., Science **318**, 949 (2007).

[6] M. Meckel, D. Comtois, D. Zeidler, A. Staudte, H. C. Bandulet, J. C. Kieffer, D. M. Villeneuve, and P. B. Corkum, Science **320**, 1478 (2008).

[7] M. Lein, J. P. Marangos, and P. L. Knight, Phys. Rev. A **66**, 051404 (2002).

[8] S. N. Yurchenko, S. Patchkovskii, I. V. Litvinyuk, P. B. Corkum, and G. L. Yudin, Phys. Rev. Lett. **93**, 223003 (2004).

[9] D. N. Fittinghoff, P. R. Bolton, B. Chang, and K. C. Kulander, Phys. Rev. Lett. **69**, 2642 (1992).

[10] B. Walker, B. Sheehy, L. F. DiMauro, P. Agostini, K. J. Schafer, and K. C. Kulander, Phys. Rev. Lett. **73**, 1227 (1994).

[11] A. Becker and F. H. M. Faisal, Phys. Rev. Lett. **84**, 3546 (2000).

[12] M. Lein, E. K. U. Gross, and V. Engel, Phys. Rev. Lett. **85**, 4707 (2000).

[13] H. Sakai, J. J. Larsen, I. Wendt-Larsen, J. Olesen, P. B. Corkum, and H. Stapelfeldt, Phys. Rev. A **67**, 063404 (2003).

[14] S. Baier, C. Ruiz, L. Plaja, and A. Becker, Phys. Rev. A **74**, 033405 (2006).

[15] M. Ferray, A. L'Huillier, X. F. Li, L. A. Lompre, G. Mainfray, and C. Manus, J. Phys. B **21**, L31 (1988).

[16] A. McPherson, G. Gibson, H. Jara, U. Johann, T. S. Luk, I. A. McIntyre, K. Boyer, and C. K. Rhodes, J. Opt. Soc. Am. B **4**, 595 (1987).

[17] J. L. Krause, K. J. Schafer, and K. C. Kulander, Phys. Rev. Lett. **68**, 3535 (1992).

[18] M. Lein, N. Hay, R. Velotta, J. P. Marangos, and P. L. Knight, Phys. Rev. Lett. **88**, 183903 (2002).

[19] M. Lein, N. Hay, R. Velotta, J. P. Marangos, and P. L. Knight, Phys. Rev. A **66**, 023805 (2002).

[20] M. Lein, P. P. Corso, J. P. Marangos, and P. L. Knight, Phys. Rev. A **67**, 023819 (2003).

[21] J. Itatani, J. Levesque, D. Zeidler, H. Niikura, H. Pepin, J. C. Kieffer, P. B. Corkum, and D. M. Villeneuve, Nature **432**, 867 (2004).

[22] T. Kanai, S. Minemoto, and H. Sakai, Nature **435**, 470 (2005).

[23] C. Vozzi, F. Calegari, E. Benedetti, J.-P. Caumes, G. Sansone, S. Stagira, M. Nisoli, R. Torres, E. Heesel, N. Kajumba, et al., Phys. Rev. Lett. **95**, 153902 (2005).

[24] W. Boutu, S. Haessler, H. Merdji, P. Breger, G. Waters, M. Stankiewicz, L. J. Frasinski, R. Taïeb, J. Caillat, A. Maquet, et al., Nat. Phys. **4**, 545 (2008).

[25] J. Zhao and Z. Zhao, Phys. Rev. A **78**, 053414 (2008).

[26] B. K. McFarland, J. P. Farrell, P. H. Bucksbaum, and M. Gühr, Science **322**, 1232 (2008).

[27] S. Haessler, J. Caillat, W. Boutu, C. Giovanetti-Teixeira, T. Ruchon, T. Auguste, Z. Diveki, P. Breger, A. Maquet, B. Carre, et al., Nat. Phys. **6**, 200 (2010).

[28] S. Baker, J. S. Robinson, C. A. Haworth, H. Teng, R. A. Smith, C. C. Chirilă, M. Lein, J. W. G. Tisch, and J. P. Marangos, Science **312**, 424 (2006).

[29] S. Baker, J. S. Robinson, M. Lein, C. C. Chirilă, R. Torres, H. C. Bandulet, D. Comtois, J. C. Kieffer, D. M. Villeneuve, J. W. G. Tisch, et al., Phys. Rev. Lett. **101**, 053901 (2008).

[30] O. Smirnova, Y. Mairesse, S. Patchkovskii, N. Dudovich, D. Villeneuve, P. Corkum, and M. Y. Ivanov, Nature **460**, 972 (2009).

[31] T. Bredtmann, S. Chelkowski, and A. D. Bandrauk, Phys. Rev. A **84**, 021401 (2011).

[32] Y. Liang, S. Augst, S. L. Chin, Y. Beaudoin, and M. Chaker, J. Phys. B **27**, 5119 (1994).

[33] C. Lyngå, A. L'Huillier, and C.-G. Wahlström, J. Phys. B **29**, 3293 (1996).

[34] R. Velotta, N. Hay, M. B. Mason, M. Castillejo, and J. P. Marangos, Phys. Rev. Lett. **87**, 183901 (2001).

[35] G. L. Kamta and A. D. Bandrauk, Phys. Rev. A **70**, 011404 (2004).

[36] G. L. Kamta and A. D. Bandrauk, Phys. Rev. A **71**, 053407 (2005).

[37] C. Jin, A.-T. Le, and C. D. Lin, Phys. Rev. A **83**, 053409 (2011).

[38] C. Jin, J. B. Bertrand, R. R. Lucchese, H. J. Wörner, P. B. Corkum, D. M. Villeneuve, A.-T. Le, and C. D. Lin, Phys. Rev. A **85**, 013405 (2012).

[39] Y. Mairesse, J. Higuet, N. Dudovich, D. Shafir, B. Fabre, E. Mével, E. Constant, S. Patchkovskii, Z. Walters, M. Y. Ivanov, et al., Phys. Rev. Lett. **104**, 213601 (2010).

[40] O. Smirnova, S. Patchkovskii, Y. Mairesse, N. Dudovich, and M. Y. Ivanov, Proc. Natl. Acad. Sci. **106**, 16556 (2009).

[41] O. Smirnova and M. Ivanov, Nat. Phys. **6**, 159 (2010).

[42] H. J. Wörner, J. B. Bertrand, P. Hockett, P. B. Corkum, and D. M. Villeneuve, Phys. Rev. Lett. **104**, 233904 (2010).

[43] R. Torres, T. Siegel, L. Brugnera, I. Procino, J. G. Underwood, C. Altucci, R. Velotta, E. Springate, C. Froud, I. C. E. Turcu, et al., Phys. Rev. A **81**, 051802 (2010).

[44] J. Zhao and M. Lein, J. Phys. Chem. A **116**, 2723 (2012).

[45] Y. Mairesse, A. de Bohan, L. J. Frasinski, H. Merdji, L. C. Dinu, P. Monchicourt, P. Breger, M. Kovačev, R. Taïeb, B. Carré, et al., Science **302**, 1540 (2003).

[46] P. Salières, A. Maquet, S. Haessler, J. Caillat, and R. Taïeb, Rep. Prog. Phys. **75**, 062401 (2012).

[47] D. Shafir, Y. Mairesse, D. M. Villeneuve, P. B. Corkum, and N. Dudovich, Nat. Phys. **5**, 412 (2009).

[48] D. Shafir, H. Soifer, B. D. Bruner, M. Dagan, Y. Mairesse, S. Patchkovskii, M. Y. Ivanov, O. Smirnova, and N. Dudovich, Nature **485**, 343 (2012).

[49] P. M. Paul, E. S. Toma, P. Breger, G. Mullot, F. Augé, P. Balcou, H. G. Muller, and P. Agostini, Science **292**, 1689 (2001).

[50] M. Hentschel, R. Kienberger, C. Spielmann, G. A. Reider, N. Milosevic, T. Brabec, P. Corkum, U. Heinzmann, M. Drescher, and F. Krausz, Nature **414**, 509 (2001).

[51] M. Ivanov, P. B. Corkum, T. Zuo, and A. Bandrauk, Phys. Rev. Lett. **74**, 2933 (1995).

[52] B. Shan, S. Ghimire, and Z. Chang, J. Mod. Opt. **52**, 277 (2005).

[53] G. Sansone, E. Benedetti, F. Calegari, C. Vozzi, L. Avaldi, R. Flammini, L. Poletto, P. Villoresi, C. Altucci, R. Velotta, et al., Science **314**, 443 (2006).

[54] I. J. Sola, E. Mevel, L. Elouga, E. Constant, V. Strelkov, L. Poletto, P. Villoresi, E. Benedetti, J.-P. Caumes, S. Stagira, et al., Nat. Phys. **2**, 319 (2006).

[55] H. Mashiko, S. Gilbertson, C. Li, S. D. Khan, M. M. Shakya, E. Moon, and Z. Chang, Phys. Rev. Lett. **100**, 103906 (2008).

[56] X. Feng, S. Gilbertson, H. Mashiko, H. Wang, S. D. Khan, M. Chini, Y. Wu, K. Zhao, and Z. Chang, Phys. Rev. Lett. **103**, 183901 (2009).

[57] K. Zhao, Q. Zhang, M. Chini, Y. Wu, X. Wang, and Z. Chang, Opt. Lett. **37**, 3891 (2012).

[58] M. Kitzler, N. Milosevic, A. Scrinzi, F. Krausz, and T. Brabec, Phys. Rev. Lett. **88**, 173904 (2002).

[59] J. Itatani, F. Quéré, G. L. Yudin, M. Y. Ivanov, F. Krausz, and P. B. Corkum, Phys. Rev. Lett. **88**, 173903 (2002).

[60] E. Skantzakis, P. Tzallas, J. E. Kruse, C. Kalpouzos, O. Faucher, G. D. Tsakiris, and D. Charalambidis, Phys. Rev. Lett. **105**, 043902 (2010).

[61] P. Tzallas, E. Skantzakis, L. A. A. Nikolopoulos, G. D. Tsakiris, and D. Charalambidis, Nat. Phys. **7**, 781 (2011).

[62] M. Drescher, M. Hentschel, R. Kienberger, M. Uiberacker, V. Yakovlev, A. Scrinzi, T. Westerwalbesloh, U. Kleineberg, U. Heinzmann, and F. Krausz, Nature **419**, 803 (2002).

[63] M. Schultze, M. Fiess, N. Karpowicz, J. Gagnon, M. Korbman, M. Hofstetter, S. Neppl, A. L. Cavalieri, Y. Komninos, T. Mercouris, et al., Science **328**, 1658 (2010).

[64] K. Klünder, J. M. Dahlström, M. Gisselbrecht, T. Fordell, M. Swoboda, D. Guénot, P. Johnsson, J. Caillat, J. Mauritsson, A. Maquet, et al., Phys. Rev. Lett. **106**, 143002 (2011).

[65] Z.-H. Loh, C. H. Greene, and S. R. Leone, Chem. Phys **350**, 7 (2008).

[66] S. Gilbertson, M. Chini, X. M. Feng, S. Khan, Y. Wu, and Z. Chang, Phys. Rev. Lett. **105**, 263003 (2010).

[67] H. Wang, M. Chini, S. Chen, C.-H. Zhang, F. He, Y. Cheng, Y. Wu, U. Thumm, and Z. Chang, Phys. Rev. Lett. **105**, 143002 (2010).

[68] W.-C. Chu, S.-F. Zhao, and C. D. Lin, Phys. Rev. A **84**, 033426 (2011).

[69] W.-C. Chu and C. D. Lin, Phys. Rev. A **85**, 013409 (2012).

[70] J. Zhao and M. Lein, New J. Phys. **14**, 065003 (2012).

[71] U. Fano, Phys. Rev. **124**, 1866 (1961).

[72] E. Goulielmakis, Z. Loh, A. Wirth, R. Santra, N. Rohringer, V. S. Yakovlev, S. Zherebtsov, T. Pfeifer, A. M. Azzeer, M. F. Kling, et al., Nature **466**, 739 (2010).

[73] M. Holler, F. Schapper, L. Gallmann, and U. Keller, Phys. Rev. Lett. **106**, 123601 (2011).

[74] M. B. Gaarde, C. Buth, J. L. Tate, and K. J. Schafer, Phys. Rev. A **83**, 013419 (2011).

[75] P. Eckle, M. Smolarski, P. Schlup, J. Biegert, A. Staudte, M. Schöffler, H. G. Muller, R. Dorner, and U. Keller, Nat. Phys. **4**, 565 (2008).

[76] P. Eckle, A. N. Pfeiffer, C. Cirelli, A. Staudte, R. Dörner, H. G. Muller, M. Büttiker, and U. Keller, Science **322**, 1525 (2008).

[77] J. Zhao and M. Lein, submitted (2013).

[78] A. J. DeMaria, D. A. Stetser, and H. Heynau, Appl. Phys. Lett. **8**, 174 (1966).

[79] D. E. Spence, P. N. Kean, and W. Sibbett, Opt. Lett. **16**, 42 (1991).

[80] U. Keller, Nature **424**, 831 (2003).

[81] T. Brabec, ed., *Strong Field Laser Physics* (Springer, 2008).

[82] P. Salières, B. Carré, L. Le Déroff, F. Grasbon, G. G. Paulus, H. Walther, R. Kopold, W. Becker, D. B. Milošević, A. Sanpera, et al., Science **292**, 902 (2001).

[83] J. D. Jackson, *Classical Electrodynamics* (Wiley, 1999).

[84] S. Patchkovskii, Z. Zhao, T. Brabec, and D. M. Villeneuve, Phys. Rev. Lett. **97**, 123003 (2006).

[85] Z. Zhao, J. Yuan, and T. Brabec, Phys. Rev. A **76**, 031404 (2007).

[86] S. Sukiasyan, C. McDonald, C. Destefani, M. Y. Ivanov, and T. Brabec, Phys. Rev. Lett. **102**, 223002 (2009).

[87] D. N. Fittinghoff, P. R. Bolton, B. Chang, and K. C. Kulander, Phys. Rev. Lett. **69**, 2642 (1992).

[88] B. Walker, B. Sheehy, L. F. DiMauro, P. Agostini, K. J. Schafer, and K. C. Kulander, Phys. Rev. Lett. **73**, 1227 (1994).

[89] K. Kondo, A. Sagisaka, T. Tamida, Y. Nabekawa, and S. Watanabe, Phys. Rev. A **48**, R2531 (1993).

[90] B. Bransden and C. Joachain, *Physics of Atoms and Molecules* (Prentice-Hall, 2003).

[91] L. Landau and E. Lifshitz, *Quantum Mechanics* (Pergamon, New York, 1965).

[92] L. V. Keldysh, Sov. Phys. JETP **20**, 1307 (1965).

[93] M. Y. Ivanov, M. Spanner, and O. Smirnova, J. Mod. Opt. **52**, 165 (2005).

[94] E. V. van der Zwan and M. Lein, Phys. Rev. Lett. **108**, 043004 (2012).

[95] M. Lewenstein, P. Balcou, M. Y. Ivanov, A. L'Huillier, and P. B. Corkum, Phys. Rev. A **49**, 2117 (1994).

[96] D. B. Milošević and W. Becker, Phys. Rev. A **66**, 063417 (2002).

[97] C. Figueira de Morisson Faria, H. Schomerus, and W. Becker, Phys. Rev. A **66**, 043413 (2002).

[98] G. F. Gribakin and M. Y. Kuchiev, Phys. Rev. A **55**, 3760 (1997).

[99] M. Y. Ivanov, T. Brabec, and N. Burnett, Phys. Rev. A **54**, 742 (1996).

[100] E. V. van der Zwan, *Molecular Imaging using Strong-Field Processes* (Doctoral thesis, 2011).

[101] I. Dreissigacker and M. Lein, Chem. Phys. **414**, 69 (2013).

[102] M. Feit, J. Fleck, Jr, and A. Steiger, J. Comp. Phys. **47**, 412 (1982).

[103] W.-C. Liu, J. H. Eberly, S. L. Haan, and R. Grobe, Phys. Rev. Lett. **83**, 520 (1999).

[104] M. Lein, E. K. U. Gross, and V. Engel, Phys. Rev. Lett. **85**, 4707 (2000).

[105] R. Kosloff and H. Tal-Ezer, Chem. Phys. Lett. **127**, 223 (1986), ISSN 0009-2614.

[106] A. Zaïr, M. Holler, A. Guandalini, F. Schapper, J. Biegert, L. Gallmann, U. Keller, A. S. Wyatt, A. Monmayrant, I. A. Walmsley, et al., Phys. Rev. Lett. **100**, 143902 (2008).

[107] C. C. Chirilă, I. Dreissigacker, E. V. van der Zwan, and M. Lein, Phys. Rev. A **81**, 033412 (2010).

[108] M. Y. Ivanov, M. Spanner, and O. Smirnova, J. Mod. Opt. **52**, 165 (2005).

[109] N. B. Delone and V. P. Krainov, J. Opt. Soc. Am. B **8**, 1207 (1991).

[110] N. Dudovich, J. Levesque, O. Smirnova, D. Zeidler, D. Comtois, M. Y. Ivanov, D. M. Villeneuve, and P. B. Corkum, Phys. Rev. Lett. **97**, 253903 (2006).

[111] S. D. Khan, Y. Cheng, M. Möller, K. Zhao, B. Zhao, M. Chini, G. G. Paulus, and Z. Chang, Appl. Phys. Lett. **99**, 161106 (2011).

[112] D. Shafir, B. Fabre, J. Higuet, H. Soifer, M. Dagan, D. Descamps, E. Mével, S. Petit, H. J. Wörner, B. Pons, et al., Phys. Rev. Lett. **108**, 203001 (2012).

[113] S. Baker, J. S. Robinson, C. A. Haworth, H. Teng, R. A. Smith, C. C. Chirilă, M. Lein, J. W. G. Tisch, and J. P. Marangos, Science **312**, 424 (2006).

[114] Z. B. Walters and O. Smirnova, J. Phys. B **43**, 161002 (2010).

[115] A.-T. Le, R. R. Lucchese, S. Tonzani, T. Morishita, and C. D. Lin, Phys. Rev. A **80**, 013401 (2009).

[116] H. Yu, T. Zuo, and A. D. Bandrauk, Phys. Rev. A **54**, 3290 (1996).

[117] A. Saenz, Phys. Rev. A **61**, 051402 (2000).

[118] I. Kawata, H. Kono, Y. Fujimura, and A. D. Bandrauk, Phys. Rev. A **62**, 031401 (2000).

[119] S. Saugout, C. Cornaggia, A. Suzor-Weiner, and E. Charron, Phys. Rev. Lett. **98**, 253003 (2007).

[120] C. C. Chirilă and M. Lein, J. Mod. Opt. **54**, 1039 (2007).

[121] R. Santra and A. Gordon, Phys. Rev. Lett. **96**, 073906 (2006).

[122] S. Patchkovskii, Z. Zhao, T. Brabec, and D. M. Villeneuve, Phys. Rev. Lett. **97**, 123003 (2006).

[123] M. Lein, Phys. Rev. Lett. **94**, 053004 (2005).

[124] M. Wickenhauser, J. Burgdörfer, F. Krausz, and M. Drescher, Phys. Rev. Lett. **94**, 023002 (2005).

[125] Z. X. Zhao and C. D. Lin, Phys. Rev. A **71**, 060702 (2005).

[126] H. Geiseler, H. Rottke, N. Zhavoronkov, and W. Sandner, Phys. Rev. Lett. **108**, 123601 (2012).

[127] A. F. Starace, Phys. Rev. A **16**, 231 (1977).

[128] Z. Zhao, *Atomic and Molecular Dynamics in Ultrashort Intense Laser Fields* (Doctoral thesis, 2005).

[129] C. Ott, A. Kaldun, P. Raith, K. Meyer, M. Laux, Y. Zhang, S. Hagstotz, T. Ding, R. Heck, and T. Pfeifer, arXiv **1205**, 0519 (2012).

[130] S. L. Haan, R. Grobe, and J. H. Eberly, Phys. Rev. A **50**, 378 (1994).

[131] P.-C. Li, X.-X. Zhou, G.-L. Wang, and Z.-X. Zhao, Phys. Rev. A **80**, 053825 (2009).

[132] M. Wickenhauser, J. Burgdörfer, F. Krausz, and M. Drescher, J. Mod. Opt. **53**, 247 (2006).

[133] M. Domke, K. Schulz, G. Remmers, G. Kaindl, and D. Wintgen, Phys. Rev. A **53**, 1424 (1996).

[134] S. H. Autler and C. H. Townes, Phys. Rev. **100**, 703 (1955).

[135] P. Lambropoulos and P. Zoller, Phys. Rev. A **24**, 379 (1981).

[136] J. Mauritsson, T. Remetter, M. Swoboda, K. Klünder, A. L'Huillier, K. J. Schafer, O. Ghafur, F. Kelkensberg, W. Siu, P. Johnsson, et al., Phys. Rev. Lett. **105**, 053001 (2010).